BROAD-BAND AND HIGH-ISOLATION PERFORMANCE OF A LUMPED-ELEMENT CIRCULATOR: THEORY AND EXPERIMENT

A Dissertation

Presented in Partial Fulfillment of the Requirements for the

Degree of Doctor of Philosophy

with a

Major in Electrical Engineering

in the

College of Graduate Studies

University of Idaho

by

Hang Dong

March 2014

Major Professor: Jeffrey L. Young, Ph.D.

AUTHORIZATION TO SUBMIT DISSERTATION

This dissertation of Hang Dong, submitted for the degree of Doctor of Philosophy with a major in Electrical Engineering and titled "BROAD-BAND AND HIGH-ISOLATION PERFORMANCE OF A LUMPED-ELEMENT CIRCULATOR: THEORY AND EXPERIMENT," has been reviewed in final form. Permission, as indicated by the signatures and dates given below, is now granted to submit final copies to the College of Graduate Studies for approval.

Major Professor ______________________________ Date__________
Jeffrey L. Young

Committee
Members ______________________________ Date__________
David H. Atkinson

______________________________ Date__________
Dean Edwards

______________________________ Date__________
Dennis Sullivan

Department
Administrator ______________________________ Date__________
Fred Barlow III

Discipline's
College Dean ______________________________ Date__________
Larry Stauffer

Final Approval and Acceptance by the College of Graduate Studies

______________________________ Date__________
Jie Chen

ABSTRACT

Research on a wide-bandwidth, high-isolation, lumped-element, crossover ferrite circulator is presented. The presented research spans the entire range of activities including theory, simulation, fabrication, measurement and assessment of the device. The research is validated by experimental data that shows unprecedented bandwidths on the order of 130% and deep isolations on the order of 30 dB. To accomplish the stated research objectives, the research is subdivided into three key parts.

In the first part, a procedure based on an ideal analytical model of a lumped-element, crossover circulator for maximizing its operating bandwidth is presented. The procedure considers the circulator as a network and employs the circulation impedance—the load impedance associated with perfect circulation—as a metric to optimize the bandwidth. Using this optimization procedure, a maximum bandwidth of 194% is obtained for an ideal circulator operating above ferromagnetic resonance (FMR). When the same procedure is applied using a simulation model for the 225-400 MHz frequency range, we achieve 125% bandwidth. This result is verified by the measurement of a fabricated device, which reveals a bandwidth of 129%.

The second part presents a novel, spiral trace topology for a lumped-element, ferrite circulator. By employing this new topology, along with various optimization methods, a circulator with high isolation and wide bandwidth is achieved for UHF applications. Based on simulation data, an isolation of 30 dB or more is possible over the 250–350 MHz frequency range. When the new trace topology is applied to a fabricated device, we obtain a UHF circulator with isolation response exceeding 30 dB, but over a shifted and wider frequency range of 260 to 390 MHz.

In the third part, a numerical method used for calculating the demagnetization factor of a non-ellipsoid ferrite body is presented. The method divides the ferrite body into small elements and considers each of them as a small, uniformly saturated ferrite volume. Then from their vector potentials, the method calculates the demagnetizing field excited by every element and superimposes them to find the total demagnetization factor at a specified observation point. By utilizing this method, we found the demagnetization factors for several non-ellipsoid ferrite bodies, including an irregular shaped ferrite slab and a non-z-directed biased ferrite disk.

ACKNOWLEDGEMENTS

First, I would like to sincerely thank my major professor Dr. Jeffrey L. Young for his continuous support and guidance throughout my graduate study. He was always there to listen and to give insightful advice. His knowledge and rigorous attitude of scholarship made my Ph.D. study a rewarding experience.

I would also like to thank Mr. Jake Smith and Mr. Brandon Aldecoa from the VHF/UHF circulator team. Their help has been the key to the success of the project. Also I would like to thank my committee members for their mentorship over the past few years.

Last, but not least, my gratitude goes to my wife Nan Yang, who always understands me, and my parents for their unconditionally support and encouragement.

This work was supported by the Office of Naval Research under grant number N00014-08-1-0286.

TABLE OF CONTENTS

LIST OF FIGURES

CHAPTER 1

INTRODUCTION

The ferrite circulator is a three-port, passive microwave network. It is one of the most important components of a mono-static radar system. In a mono-static radar system, both the transmitter and the receiver are connected to a single antenna through the circulator to perform simultaneous transmit and receive. By making use of the non-reciprocal properties of the ferrite material, the circulator provides a simple yet efficient way to re-direct the signal flow and de-couple the electromagnetic wave between the transmitter and the receiver. A depiction of a mono-static radar system is drawn in Figure 1.1. As seen in this figure, signal flow from the transmitter is directed to the antenna for radiation, with the receiver remaining isolated. Meanwhile, the signal received by the antenna will be directed to the receiver without affecting the transmitter.

Because the antenna operates in different frequency ranges, several types of ferrite circulators have been developed, such as the lumped-element, crossover circulators for the low frequency range, the microstrip junction circulators for the X-band range and waveguide junction circulators for the K-band range and higher [1].

1.1 Motivation of Research

The 225-400MHz communication band is the most important frequency band for military applications. The United States Navy is interested in developing a single antenna communication system that covers this range. As an important component of the system, a circulator operating in the UHF frequency range with wide bandwidth and high isolation needs to be designed. In the VHF-UHF frequency band, lumped-element, crossover ferrite circulators have superior performance once compared to other types of circulators. This dissertation reports on the study of the maximum bandwidth and high isolation performance of a lumped-element circulator. The dissertation will first derive the frequency-independent bandwidth limit for a lumped-element ferrite circulator. It will then focus on designing a circulator device for UHF band applications. The last part of dissertation will cover research work on a numerical method to calculate the demagnetization field in

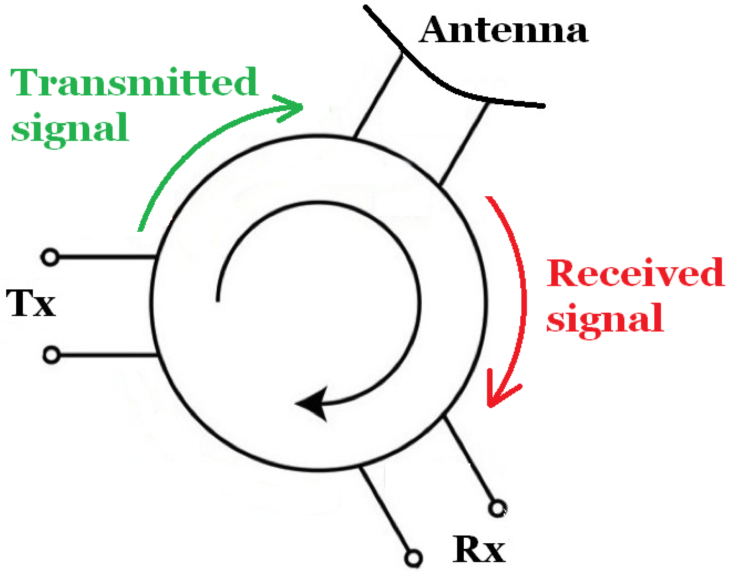

Figure 1.1: A communication system with a circulator.

a ferrite disk. Quantifying this field is critical to the design of circulators.

1.2 Background

Research on lumped-element, crossover circulators for RF communication applications commenced in the early 1960's with the work of Konishi [2], who articulated the theory of operation for the UHF and VHF bands. In recent years a resurgence of activity in crossover circulator research has occurred due to advances in mobile communication devices.

Among the circulator's many important properties, large bandwidth is one of the most important. This leads us to the question of how much bandwidth a crossover circulator can achieve. Miura *et al.* [3] provided one answer using an eigenvalue analysis and reported a 9.8% bandwidth (820-900 MHz) for miniature circulators. Schloemann [4] provided a different perspective on bandwidth by relating bandwidth performance to the geometrical design of the ferrite crossover network. Using a quality factor analysis, he showed that bandwidths on the order of one or two octaves are possible, but no simulation or experimental results supported this claim. A casual review of circulators currently on the market indicates that the current state-of-the-art is close to 100% bandwidth for operating frequencies near 400 MHz.

A typical lumped-element, ferrite circulator device is composed of two parts: the ferrite crossover network and the tuning/matching elements. To improve the device's performance, considerable effort has been expended on the design and optimization of both parts. Konishi [5][6] focused attention on different designs of the center conductor trace of the crossover network. He compared the bandwidth performance of different center trace topologies and developed a model to describe the imperfect coupling between the traces. Takeda *et al.* [7] discussed the influence of the angle between the three traces on the isolation performance of a 800 MHz band circulator. Their work indicated that the angle between the three conductor traces is not a key parameter for circulator performance. Instead of focusing on the crossover network, Anderson [8] put effort on using the external resonant tuning elements to widen the bandwidth of the device and obtained good results in the microwave frequency bands.

The demagnetization factor is a concept that relates the external biasing field to the internal field of the ferrite. In non-ellipsoid ferrite bodies, the demagnetization factor is both anisotropic and inhomogeneous. As a result of this fact, a non-uniform internal field exists within the ferrite material. Since the internal field controls the properties of the ferrite, knowing the demagnetizing factor is necessary to characterize the properties of the ferrite. The search for more accurate and efficient methods to calculate the demagnetization field inside a non-ellipsoid ferrite sample has been the focus of much research. Joseph and Schlomann [9][10][11] set the foundation for analytical methods used for the demagnetization factor calculation. By using a series expansion, they derived the expression of the demagnetization factor in the z-direction inside a rectangular slab and circular cylinders ferrite bodies within a perpendicularly saturated ferrite. Based on that, Kraus [12] developed the field expressions by including non-z-directional components in order to calculate the demagnetization factor of a cylindrical body with a biasing field of arbitrary directions. Calculating the demagnetizing field by numerical methods has also been investigated widely. Kobayashi *et al.* [13] analyzed the demagnetization factors of a cylinder by its surface magnetic charge density, which is a function of position and the relative permeability of the ferrite material. Huang and Pardavi-Horvath [14] developed a numerical method that subdivides the sample using rectangular elements and then found the demagnetizing factor between each pair of elements based on their magnetic scalar potentials.

1.3 Outline of Dissertation

In Chapter 2 we determine the upper bound on bandwidth performance of a circulator based upon theoretical considerations and optimization methodologies. Particularly, using the concept of the circulation impedance, which refers to the impedance load that results in perfect isolation, in conjunction with an ideal electromagnetic field model, we find that a 194% maximum bandwidth is theoretically possible. This result is independent of the choice of center frequency for above-FMR (ferromagnetic resonance) operation. Using more precise models as obtained from simulation and typical values for the magnetic saturation, we show that bandwidths on the order of 130% are realistic. This latter result is also confirmed by experimentation.

In Chapter 3 we discuss a novel center trace topology for the crossover network. The topology results in a deep isolation, broad-band performance for circulators operating in the UHF band. We discuss the design and optimization procedure for this new topology. Also, the simulated and measured performance of a circulator device utilizing this topology are presented.

Chapter 4 introduces the de-embedding technique that is used to remove the influence of the connectors from the measurement results of a circulator. With the connectors mounted on the ports of a circulator, the frequency response measured by a network analyser is the combination of both the circulator device and the connectors. The technique described in Chapter 4 de-embeds the influence of the connector and helps us to characterize the performance of the circulator itself.

In Chapter 5 we present a newly developed method for calculating the demagnetization factor of a non-ellipsoidal ferrite. The method divides a ferrite sample into elements and calculates the demagnetizing factor at an observation point from the superposition of the demagnetizing field of all elements. After introducing the calculation procedure, the result from this new method is validated against analytical solutions by using ferrite cylinders with different radius-to-height ratios. Finally, demagnetization factor computations for several ferrite bodies are presented to illustrate the application of the method.

CHAPTER 2

MAXIMUM BANDWIDTH PERFORMANCE OF AN IDEAL LUMPED-ELEMENT CIRCULATOR

2.1 Introduction

In this chapter our discussion focuses on the method used to determine the upper bandwidth limit of a lumped-element ferrite circulator. We start with the basic concept of the ferrite material and the ideal microwave network model of a circulator. We introduce the bandwidth optimization process and show how the notion of the circulation impedance can be used to estimate device bandwidth. Finally, simulation data and measurement data are provided to support the claims made herein.

2.2 Theoretical Analysis

2.2.1 Key Metrics of a Ferrite Circulator

Three power-related metrics are used to describe the performance of a circulator: isolation I, return loss RL and insertion loss IL. They are defined by power flows between the three ports of the circulator, as shown in Figure 2.1. The isolation indicates how much transmit power is coupled to the receiver. The return loss is the amount of power reflected by the circulator back to the transmitter. It quantifies the impedance mismatch between the circulator and the signal source. The insertion loss quantifies the power loss through the circulator. Ideally, both the return loss and isolation are to be maximized while minimizing the insertion loss.

If we assume a transmitter, receiver and antenna are connected to ports 1, 2 and 3 of a circulator, respectively, then the I, RL and IL can be expressed by the circulator's S-parameters as

$$\begin{aligned} RL &= -20\log_{10}|S_{11}| \\ I &= -20\log_{10}|S_{21}| \\ IL &= -20\log_{10}|S_{31}|. \end{aligned} \tag{2.2.1}$$

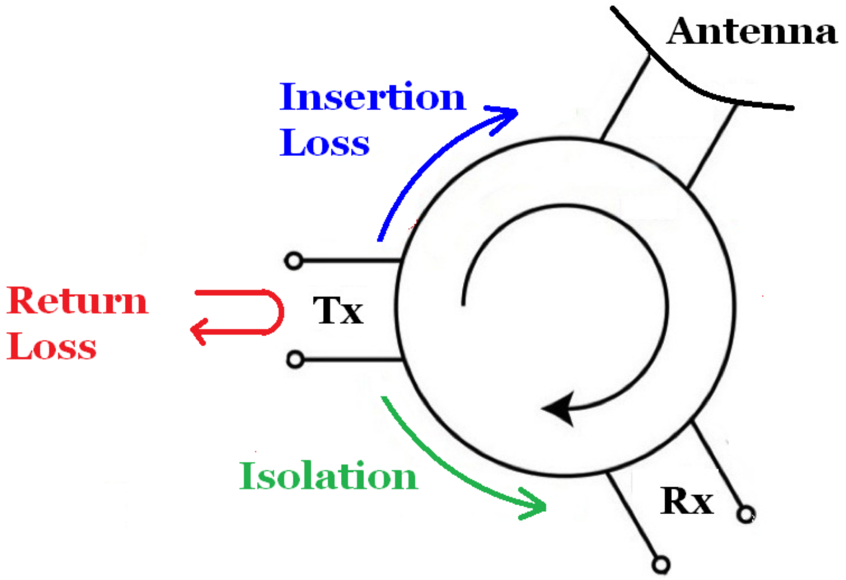

Figure 2.1: A depiction of power flow to define the performance metrics of a circulator.

Another metric associated with the performance of a circulator is the operating bandwidth. The bandwidth is defined as a frequency band f_a to f_b in which the isolation and return loss of a circulator are less than a specified value and the insertion loss reaches a pre-set value. In this work, we will consider return loss and isolation values on the order of 15 dB and an insertion loss value on the order of 0.5 dB. The following percent bandwidth definition is used:

$$\%\ BW \equiv \frac{f_b - f_a}{f_a} \times 100\%. \tag{2.2.2}$$

Such a definition allows us to say that one octave or 100% corresponds to the same bandwidth.

2.2.2 Ideal Model of a Lumped-Element Circulator

To ascertain the bandwidth, return loss, insertion loss and isolation characteristics of a circulator, we consider first an ideal network model [15]. The derivation process is based on the simplified model of a ferrite material as first developed by Polder [16]. He assumed the ferrite is of infinite extension (i.e., no boundary) with a uniform internal field $\mathbf{H}_0$ to place the ferrite into saturation. Polder showed when the external biasing field is in

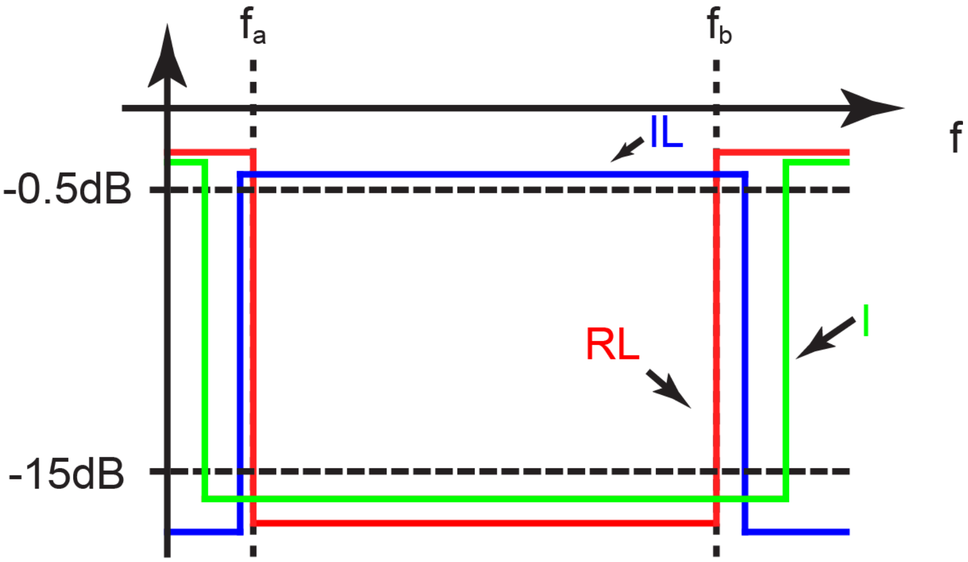

Figure 2.2: An example depicting the bandwidth definition of a circulator.

z-direction, the following RF relationship is satisfied between the internal magnetic flux density $\mathbf{B}$ and magnetic field strength $\mathbf{H}$:

$$\mathbf{B} = \mu_o (\mathbf{H} + \mathbf{M}) = \mu_o ([1] + [\chi]) \mathbf{H} \tag{2.2.3}$$

in which $\mathbf{M}$ is magnetization of the ferrite material. Here $[\chi]$ in the above equation is the susceptibility tensor given by

$$[\chi] = \begin{bmatrix} \chi_{xx} & \chi_{xy} & 0 \\ \chi_{yx} & \chi_{yy} & 0 \\ 0 & 0 & 0 \end{bmatrix}, \tag{2.2.4}$$

where the elements are

$$\begin{aligned} \chi_{xx} = \chi_{yy} &= \frac{\omega_o \omega_m}{\omega_o^2 - \omega^2}, \\ \chi_{xy} = -\chi_{yx} &= \frac{j\omega\omega_m}{\omega_o^2 - \omega^2}. \end{aligned} \tag{2.2.5}$$

For a RF field, $\mathbf{B} = [\mu] \cdot \mathbf{H}$, where $[\mu]$ is the RF permeability tensor. From Eqn. (2.2.3), we write

$$[\mu] = \mu_o \begin{bmatrix} \mu & -j\kappa & 0 \\ j\kappa & \mu & 0 \\ 0 & 0 & 1 \end{bmatrix}. \tag{2.2.6}$$

This is called the Polder tensor and its elements μ and κ are defined as

$$\mu = 1 + \frac{\omega_0 \omega_m}{\omega_0^2 - \omega^2} \tag{2.2.7}$$

and

$$\kappa = \frac{\omega_m \omega}{\omega_0^2 - \omega^2}. \tag{2.2.8}$$

The angular frequencies ω_0 and ω_m in Eqns. (2.2.5), (2.2.7) and (2.2.8) are associated with the ferrite material properties. The angular frequency ω_m depends on the magnetic saturation of the ferrite such that $\omega_m = 2\pi f_m$, where $f_m = (2.8 \times 10^6)(4\pi M_s)(\mathrm{Hz/G})$. Also, ω_0 is the Larmor angular frequency, which is a function of the internal field H_0 of the ferrite such that $\omega_0 = 2\pi f_0$, where $f_0 = (2.8 \times 10^6)(H_0)(\mathrm{Hz/Oe})$.

Hence, from Eqn. (2.2.6) we have the following relationship between **B** and **H** in the ferrite:

$$\begin{bmatrix} B_x \\ B_y \\ B_z \end{bmatrix} = \mu_o \begin{bmatrix} \mu & -j\kappa & 0 \\ j\kappa & \mu & 0 \\ 0 & 0 & 1 \end{bmatrix} \begin{bmatrix} H_x \\ H_y \\ H_z \end{bmatrix}. \tag{2.2.9}$$

This equation reveals two basic properties of the ferrite material. First, the ferrite is anisotropic. This can be seen from the fact that the x-component of **B** depends on both the x and y components of the **H** field; likewise B_y is determined from both H_x and H_y. The second property is non-reciprocity, because $[\mu]$ is a non-symmetric tensor. This means the field components excited by a RF signal travelling in one direction may not be the same as the same signal travelling in the reverse direction. It is these two properties that form the fundamentals of how a ferrite material can be used as the core of a circulator.

The basic configuration of a crossover circulator, which is shown in Figure 2.3, consists of two ferrite pucks with three interwoven conductor traces between them. The ferrite pucks are assumed to be fully saturated by an applied external biasing field H_a whose direction is perpendicular to the trace plane. The traces are placed at 120° intervals to form a crossover topology. All three traces are assumed to be electrically isolated from each other using air as an insulator. One end of any trace is used as the port of the circulator while the other end is connected to the ground plane that forms the housing of the structure (not shown for clarity). This circulator forms a three-port network.

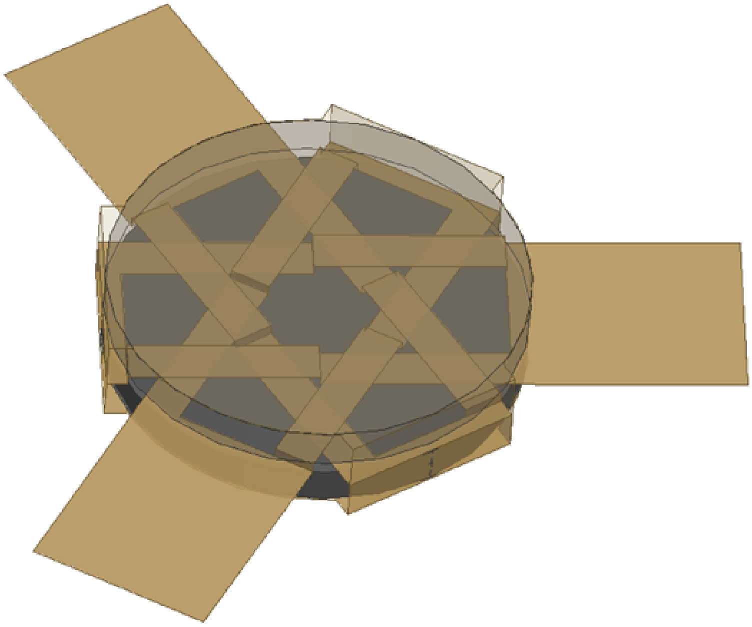

Figure 2.3: A typical lumped-element, crossover ferrite circulator.

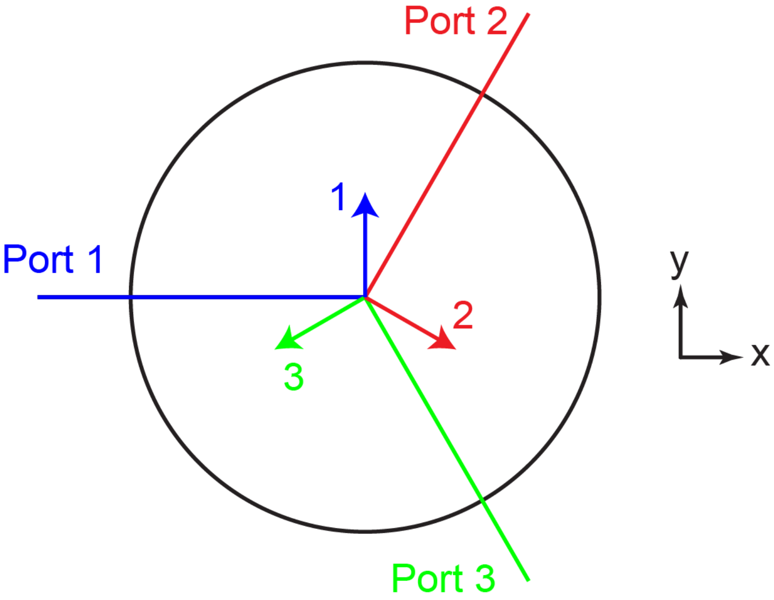

Figure 2.4: Components of the new, non-orthogonal coordinate system.

By assuming the internal RF field is uniform in the ferrite disks, we can decompose the components of **B** and **H** using a non-orthogonal coordinate system, as shown in Figure 2.4. The directional components of the new coordinate system are perpendicular to their corresponding port; therefore, they are 120° apart but not orthogonal to each other. Thus for the **H** field, its components H_x and H_y in the new coordinate system are given by

$$H_x = H_2 \cos 30^\circ - H_3 \cos 30^\circ = \frac{\sqrt{3}H_2}{2} - \frac{\sqrt{3}H_3}{2} \tag{2.2.10}$$

$$H_y = H_1 - H_2 \sin 30^\circ - H_3 \sin 30^\circ = H_1 - \frac{H_2}{2} - \frac{H_3}{2}. \tag{2.2.11}$$

From Figure 2.4 we see that B_1, which is created by the RF signal on port 1, is equal to B_y. Then from Eqn. (2.2.9), we have

$$B_1 = B_y = j\mu_o \kappa H_x + \mu_o \mu H_y. \tag{2.2.12}$$

By inserting Eqn. (2.2.10) and (2.2.11) into the equation above, we can write B_1 as

$$B_1 = \mu_o \left[\mu H_1 - (1/2)(\mu - j\sqrt{3}\kappa)H_2 - (1/2)(\mu + j\sqrt{3}\kappa)H_3 \right]. \tag{2.2.13}$$

Applying similar manipulation to B_2 and B_3, we obtain

$$B_2 = \mu_o \left[-(1/2)(\mu + j\sqrt{3}\kappa)H_1 + \mu H_2 - (1/2)(\mu - j\sqrt{3}\kappa)H_3 \right] \tag{2.2.14}$$

and

$$B_3 = \mu_o \left[-(1/2)(\mu - j\sqrt{3}\kappa)H_1 + -(1/2)(\mu + j\sqrt{3}\kappa)H_2 + \mu H_3 \right]. \tag{2.2.15}$$

Eqns. (2.2.13), (2.2.14) and (2.2.15) form a matrix equation that relates **B** to **H** at each port. This relationship is

$$\begin{bmatrix} B_1 \\ B_2 \\ B_3 \end{bmatrix} = \mu_o [\mu_c] \begin{bmatrix} H_1 \\ H_2 \\ H_3 \end{bmatrix}. \tag{2.2.16}$$

Here

$$[\mu_c] = \begin{bmatrix} \mu_{11} & \mu_{31} & \mu_{21} \\ \mu_{21} & \mu_{11} & \mu_{31} \\ \mu_{31} & \mu_{21} & \mu_{11} \end{bmatrix} \tag{2.2.17}$$

with

$$\begin{aligned} \mu_{11} =& \mu \\ \mu_{21} =& -(\mu + j\sqrt{3}\kappa)/2 \\ \mu_{31} =& -(\mu - j\sqrt{3}\kappa)/2. \end{aligned} \tag{2.2.18}$$

The voltage and current at each port can be computed from the electromagnetic field via Faraday's law and Ampere's law. From Faraday's law, the voltage at port i created by $\mathbf{B}$ at the same port is

$$V_i = j\omega A_e B_i, \tag{2.2.19}$$

where A_e is an effective area parameter related to the trace area and the height of the ferrite disks. From the Ampere's law, the current flowing into port i is related to the magnetic intensity H_i via equation

$$I_i = l_e H_i. \tag{2.2.20}$$

Here l_e is the effective length parameter, which is a function of the trace width as well as the height of the ferrite.

When Eqns. (2.2.19) and (2.2.20) are inserted into (2.2.16), we obtain a matrix equation for the voltage and current at each port of the circulator, which is

$$\begin{bmatrix} V_1 \\ V_2 \\ V_3 \end{bmatrix} = j\omega L_0 [\mu_c] \begin{bmatrix} I_1 \\ I_2 \\ I_3 \end{bmatrix}. \tag{2.2.21}$$

Here L_0 is an effective inductance for each port and is defined by

$$L_0 = \frac{\mu_o A_e}{l_e}. \tag{2.2.22}$$

Again A_e and l_e are effective area and length parameters, and their precise values are not immediately known. However, since A_e and l_e are only dependant on the physical dimensions of the ferrite pucks and traces, it follows that L_0 is a function of the geometrical layout of the device.

From the definition of impedance matrix for a 3-port microwave network, we can write

$$\begin{bmatrix} V_1 \\ V_2 \\ V_3 \end{bmatrix} = [\mathbf{Z}] \begin{bmatrix} I_1 \\ I_2 \\ I_3 \end{bmatrix}. \tag{2.2.23}$$

When this equation is compared to Eqn. (2.2.21), we obtain

$$\mathbf{Z} = j\omega L_0[\mu_c], \tag{2.2.24}$$

which gives the expression of the impedance matrix for a idealized ferrite circulator.

The elements of $\mathbf{Z}$, i.e., the Z-parameters of the ideal device, can be expressed as

$$\begin{aligned} Z_{11} = Z_{22} = Z_{33} &= j\omega L_0 \mu \\ Z_{12} = Z_{23} = Z_{31} &= -j\omega L_0(\mu - j\sqrt{3}\kappa)/2 \\ Z_{13} = Z_{21} = Z_{32} &= -j\omega L_0(\mu + j\sqrt{3}\kappa)/2. \end{aligned} \tag{2.2.25}$$

By inserting Eqns. (2.2.7) and (2.2.8) into (2.2.25), we obtain the following impedance parameters:

$$\begin{aligned} Z_{11} =& j\omega L_0 \left(1 + \frac{\omega_0 \omega_m}{\omega_0^2 - \omega^2}\right) \\ Z_{21} =& -\frac{Z_{11}}{2} + \frac{\sqrt{3}}{2}\left(\frac{\omega^2 \omega_m L_0}{\omega_0^2 - \omega^2}\right) \\ Z_{31} =& -\frac{Z_{11}}{2} - \frac{\sqrt{3}}{2}\left(\frac{\omega^2 \omega_m L_0}{\omega_0^2 - \omega^2}\right). \end{aligned} \tag{2.2.26}$$

These equations can be rewritten as

$$\begin{aligned} Z_{11} &= jX \\ Z_{21} &= -j\frac{1}{2}X + R \\ Z_{31} &= -j\frac{1}{2}X - R \end{aligned} \tag{2.2.27}$$

with

$$R = \frac{\sqrt{3}\omega L_0}{2}\left(\frac{\omega\omega_m}{\omega_0^2 - \omega^2}\right) \tag{2.2.28}$$

and

$$X = \omega L_0\left(1 + \frac{\omega_0\omega_m}{\omega_0^2 - \omega^2}\right). \tag{2.2.29}$$

These latter forms for Z_{ij} will simplify the ensuing mathematical manipulations.

There are two things worth discussing in light of the previous mathematical treatment. First, the internal field H_0 is a function of both the external biasing field H_a and the demagnetization field. For non-ellipsoidal shapes (i.e., disks), the demagnetization field is computed from a tensor demagnetization factor. For purposes of the study, we make the usual assumption that the demagnetization tensor is well approximated by a scalar such that

$$H_0 \approx H_a - 4\pi M_s N_z, \tag{2.2.30}$$

where N_z is the demagnetization scalar in the z-direction. Although N_z is technically a function of position, as discussed extensively in Chapter 5, we treat it as a constant in the context of the ideal model. The pros and cons of this assumption have also been discussed in [9][17][18]. For thin disks, $N_z \approx 1$ [19]. For above-FMR operation ω_0 defines the upper frequency limit of the operating range. When ω nearly equals $\omega_\circ$ the losses in the ferrite are excessive and the fields tend to be evanescent.

The second thing is the Polder terms μ and κ defined in Eqns. (2.2.7) and (2.2.8) are written for lossless ferrites. When ferrite loss is considered, we replace ω_0 with $\omega_0 + j\alpha\omega$, where α is a phenomenological loss coefficient calculated from the linewidth of the ferrite material. For actual ferrites operating in above-FMR mode, linewidths as small as 10 Oe are available, resulting in values of α less than 10^{-3}. It is therefore reasonable to assume no loss in our initial theoretical analysis of an ideal circulator. Moreover, since loss tends to increase bandwidth, we choose to set $\alpha = 0$ in order to create a least upper bandwidth bound.

2.2.3 Circulation Impedance and Bandwidth Estimation

The circulation impedance Z_c of a three-port network is defined as the load that results in perfect isolation [20]. This same load will also result in perfect return loss and insertion loss when the network is lossless. The combined result is called perfect circulation. According to [20], when port one is chosen as the input and port three is isolated, the load impedance at port two must be of the form

$$Z_c = \frac{Z_{32}Z_{21}}{Z_{31}} - Z_{22}. \tag{2.2.31}$$

For the three-port symmetrical crossover network whose Z-parameters are given by Eqns. (2.2.27), (2.2.28) and (2.2.29), this load impedance is also used for the other two ports. In terms of R and X, we replace the previous equation with

$$Z_c = \frac{Z_{21}^2}{Z_{31}} - Z_{11} = \left(R - j\frac{1}{2}X\right)\left(\frac{3X^2 - 4R^2}{X^2 + 4R^2}\right). \tag{2.2.32}$$

Typically, perfect circulation is achievable at a few discrete frequencies and partially achieved over a range of frequencies, say from f_a to f_b. The bandwidth BW is defined using specified values of isolation I, return loss RL, and insertion loss IL over the range f_a to f_b. For purposes herein we arbitrarily regard 15 dB of isolation and return loss along with 0.5 dB of insertion loss as acceptable when discussing bandwidth.

A typical plot of Z_c normalized by $\omega_0 L_0$ is shown in Figure 2.5. To realize Z_c, a lossless matching network needs to be placed between the crossover device and the load resistor R_L to transform R_L into Z_c. How well such a matching network can accomplish this task dictates the operating bandwidth. It is obvious from Figure 2.5 that if perfect circulation performance is desired in the range $0 < f < f_0$, a load with negative reactance is needed. To realize this negative reactance of Z_c it behooves us to use a shunt capacitor C_0 across each port. Also, it is well known that a capacitor C_g placed between the common wire of the ports and the ground of the circulator can widen the operating bandwidth [21][22].

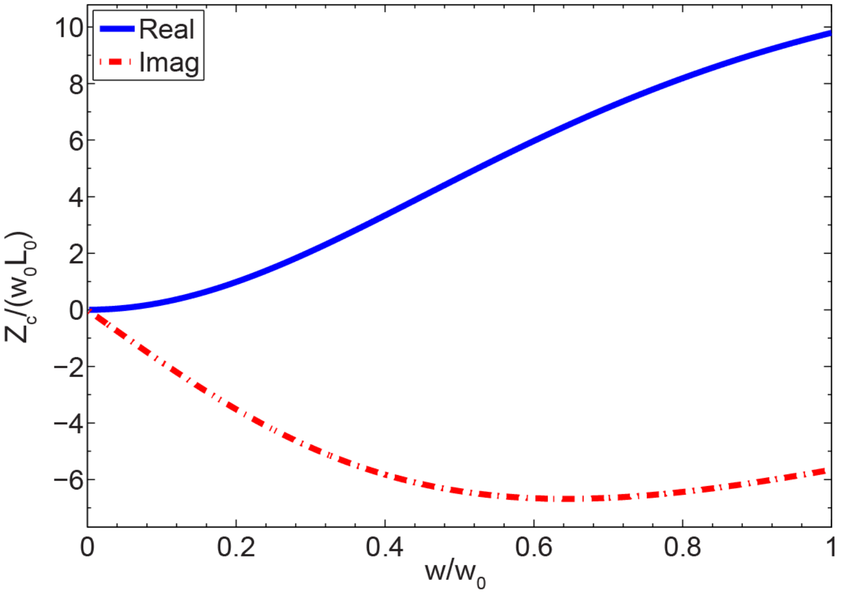

Figure 2.5: Typical Z_c data of an ideal circulator; here $\omega_m/\omega_0 = 4$.

According to Knerr, tuning components connected to the ports can only affect two of the three eigenvalues of the three-port network while C_g can influence the third eigenvalue. Hence, this eigenvalue analysis appeals to the optimal topology of the tuning network, as shown in Figure 2.6. The role of L_1 and C_1 will be discussed in an ensuing paragraph.

The precise effect of C_0 and C_g can be understood through the following analysis. We start with the normalization of the impedance matrix $\mathbf{Z}$ of the ideal crossover network:

$$\mathbf{N} \equiv \frac{\mathbf{Z}}{\omega_0 L_0} = \begin{bmatrix} N_{11} & N_{31} & N_{21} \\ N_{21} & N_{22} & N_{31} \\ N_{31} & N_{21} & N_{33} \end{bmatrix} \tag{2.2.33}$$

where

$$N_{11} = \frac{Z_{11}}{\omega_0 L_0} = j\bar{X}, \tag{2.2.34}$$

$$N_{21} = \frac{Z_{21}}{\omega_0 L_0} = -j\frac{1}{2}\bar{X} + \bar{R}, \tag{2.2.35}$$

and

$$N_{31} = \frac{Z_{31}}{\omega_0 L_0} = -j\frac{1}{2}\bar{X} - \bar{R}, \tag{2.2.36}$$

in which case

$$\bar{R} \equiv \frac{R}{\omega_0 L_0} = \frac{\sqrt{3}}{2}\left[\frac{(\omega/\omega_0)^2(\omega_m/\omega_0)}{1-(\omega/\omega_0)^2}\right] \tag{2.2.37}$$

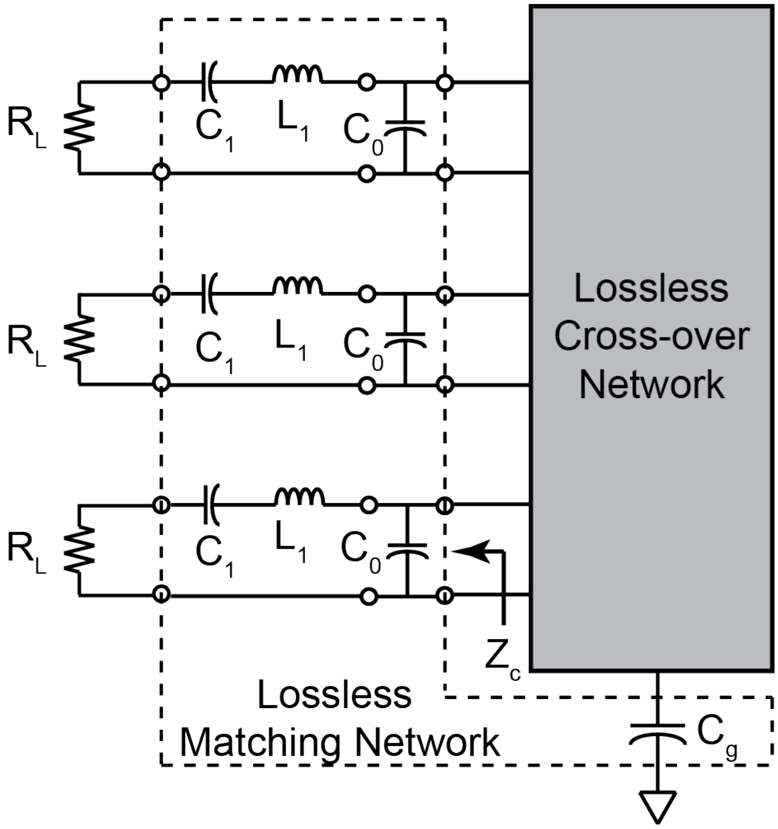

Figure 2.6: Matching network realization of Z_c.

and

$$\bar{X} \equiv \frac{X}{\omega_0 L_0} = \frac{\omega}{\omega_0}\left(1 + \frac{\omega_m/\omega_0}{1-(\omega/\omega_0)^2}\right). \tag{2.2.38}$$

By placing C_0 across each port, the crossover network is transformed into a new network whose Z-parameter matrix is $\mathbf{Z}'$; the relationship between $\mathbf{Z}$ and $\mathbf{Z}'$ is

$$\begin{aligned}\mathbf{Z}' =& \left[\mathbf{U} + j\omega C_0 \mathbf{Z}\right]^{-1} \mathbf{Z} \\ =& \omega_0 L_0 \left[\mathbf{U} + j\omega C_0 \omega_0 L_0 \mathbf{N}\right]^{-1} \mathbf{N}.\end{aligned} \tag{2.2.39}$$

Here, $\mathbf{U}$ is the identity matrix. If we define

$$\omega_r \equiv \frac{1}{\sqrt{L_0 C_0}} \tag{2.2.40}$$

as the resonant frequency related to C_0 and L_0, then through various manipulations, $\mathbf{Z}'$ can be equally written as

$$\mathbf{Z}' = \omega_0 L_0 \left[\mathbf{U} + j\frac{(\omega/\omega_0)}{(\omega_r/\omega_0)^2}\mathbf{N}\right]^{-1} \mathbf{N}. \tag{2.2.41}$$

Applying similar normalizations as in Eqn. (2.2.33) to $\mathbf{Z}'$, we obtain

$$\mathbf{N}' \equiv \frac{\mathbf{Z}'}{\omega_0 L_0} = \left[\mathbf{U} + j\frac{(\omega/\omega_0)}{(\omega_r/\omega_0)^2}\mathbf{N}\right]^{-1} \mathbf{N}. \tag{2.2.42}$$

When C_g is connected to the network, the Z-parameters are transformed from $\mathbf{Z}'$ into $\mathbf{Z}''$ such that

$$\begin{aligned}\mathbf{Z}'' =& \mathbf{Z}' + \frac{1}{j\omega C_g}\mathbf{E} \\ =& \omega_0 L_0 \left(\mathbf{N}' + \frac{1}{j\omega_0 \omega L_0 C_g}\mathbf{E}\right)\end{aligned} \tag{2.2.43}$$

where

$$\mathbf{E} = \begin{bmatrix} 1 & 1 & 1 \\ 1 & 1 & 1 \\ 1 & 1 & 1 \end{bmatrix}. \tag{2.2.44}$$

If we define ω_g as the grounding resonant frequency associated with C_g and L_0 by

$$\omega_g \equiv \frac{1}{\sqrt{L_0 C_g}}, \tag{2.2.45}$$

then $\mathbf{Z}''$ becomes

$$\mathbf{Z}'' = \omega_0 L_0 \left(\mathbf{N}' - \frac{j(\omega_g/\omega_0)^2}{(\omega/\omega_0)}\mathbf{E}\right). \tag{2.2.46}$$

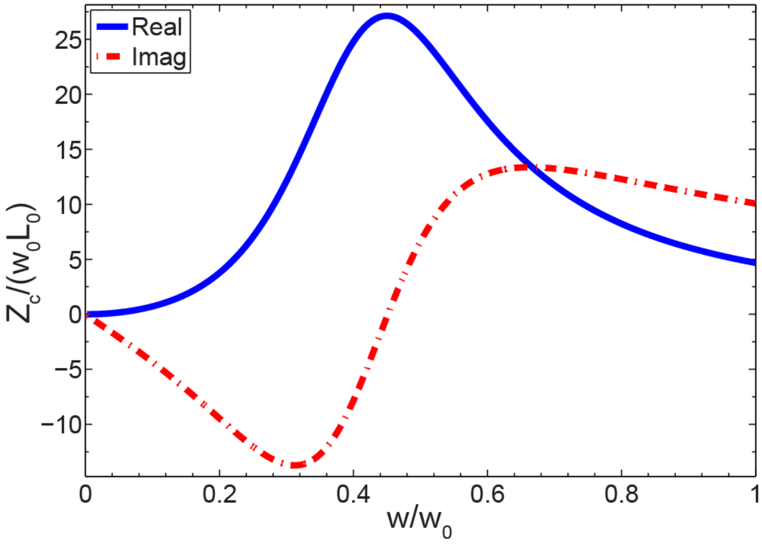

Figure 2.7: A typical plot of Z_c with C_0 and C_g tuning.

Again, it is desirable to normalize $\mathbf{Z}''$ and write

$$\mathbf{M} \equiv \frac{\mathbf{Z}''}{\omega_0 L_0} = \left(\mathbf{N}' - \frac{j(\omega_g/\omega_0)^2}{(\omega/\omega_0)}\mathbf{E}\right). \tag{2.2.47}$$

By definition $\mathbf{M}$ is the normalized Z-parameter matrix of the crossover network together with C_0 and C_g tuning. Although C_0 and C_g are part of the matching network, we refer to them as "tuning elements" since their function is to shift the center frequency to the desired frequency band. The normalized circulation impedance Z_{cm} for this transformed network, per Eqn. (2.2.31), is therefore

$$\frac{Z_{cm}}{\omega_0 L_0} = \frac{M_{21}^2}{M_{31}} - M_{11}. \tag{2.2.48}$$

From Eqns. (2.2.33), (2.2.42) and (2.2.47), we see that $\mathbf{M}$ depends on four frequency ratios:

$$\frac{\omega}{\omega_0}, \ \frac{\omega_m}{\omega_0}, \ \frac{\omega_r}{\omega_0}, \ \text{and} \ \frac{\omega_g}{\omega_0}.$$

Moreover, since $Z_{cm}/(\omega_0 L_0)$ is a function of the matrix elements of $\mathbf{M}$, it is only controlled by these four ratios. For a given set of parameters $Z_{cm}/(\omega_0 L_0)$ can be calculated and the operating bandwidth for the corresponding device can be estimated.

Consider a typical plot of $Z_{cm}/(\omega_0 L_0)$, as shown in Figure 2.7. After including the tuning elements C_0 and C_g, our goal is to find a matching network that can transform the resistive load R_L into Z_{cm}. This can be accomplished using a series LC circuit, which is shown in Figure 2.8.

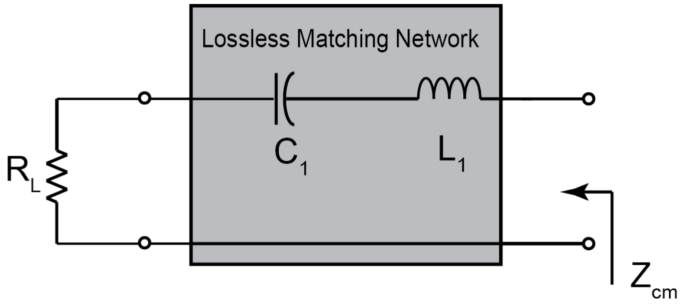

Figure 2.8: The matching network topology for a post-tuned crossover network.

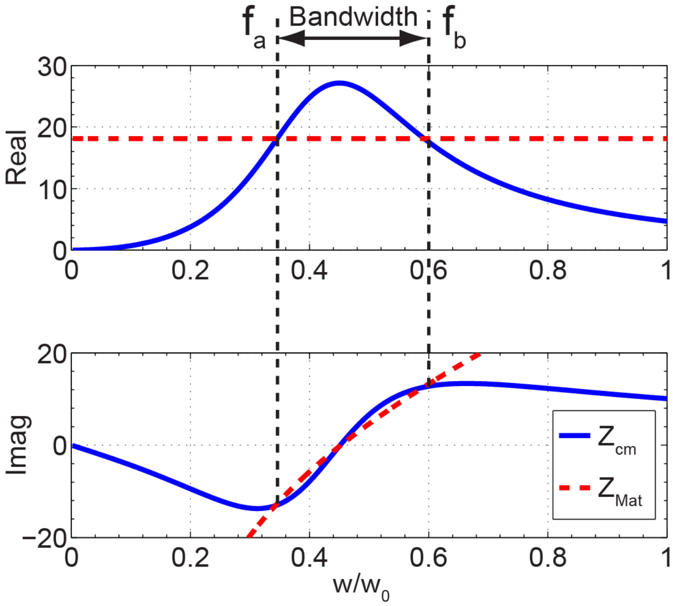

Figure 2.9: Comparison of Z_{cm} and the impedance of a series RLC circuit.

The impedance Z_{Mat} of this series LC circuit and resistive load, which is given by

$$Z_{Mat} = R_L + j(\omega L_1 - \frac{1}{\omega C_1}), \tag{2.2.49}$$

shows good agreement with Z_{cm} in the frequency range f_a to f_b (see Figure 2.9). The imaginary part of Z_{Mat} matches the circulation reactance X_{cm} (i.e., the imaginary part of Z_{cm}) very well while the real part of Z_{Mat}, which is just the load R_L, matches the circulation resistance R_{cm} (i.e., the real part of Z_{cm}). From the definition of circulation impedance it is clear that near-perfect circulation is achieved in the range f_a to f_b by having this matching network connected between the crossover network and R_L on each port, even though R_{cm} is not perfectly matched with R_L. The mismatch between R_L and R_{cm} determines the value of isolation since the match between X_{Mat} and X_{cm} is nearly perfect. For example, 14 dB of isolation suggests that R_L should be set to around 2/3 of the peak value of R_{cm}.

Since we have circulation over the range f_a to f_b, the frequencies f_a and f_b are the estimated bounds for the band of operation. These frequencies are the zero slope points of X_{cm}. However, if the maximum of X_{cm} occurs outside of the range $[0, f_0]$, we set $f_b = f_0$ to avoid operating near resonance. As an example, consider Figure 2.9 in which $\omega_a/\omega_0 = 0.312$ and $\omega_b/\omega_0 = 0.664$; for this case $BW = 112\%$.

2.2.4 Bandwidth Optimization

The preceding analysis reveals how the normalized circulation impedance $Z_{cm}/(\omega_0 L_0)$ of the network is a function of the four frequency ratios ω/ω_0, ω_m/ω_0, ω_r/ω_0 and ω_g/ω_0. And since bandwidth is estimated from the circulation impedance, it is therefore determined by these four ratios. This suggests that optimal values for these ratios exist that maximize bandwidth over the range $0 < \omega/\omega_0 < 1$. To determine these optimal ratios, an optimization procedure was developed. It fixes the ratio ω_m/ω_0 and then sweeps the ratios ω_r/ω_0 and ω_g/ω_0 over pre-set ranges. For each set of ω_r/ω_0 and ω_g/ω_0, the procedure calculates the bandwidth over $0 < \omega/\omega_0 < 1$. A mark for this bandwidth is placed on the z-axis of a 3-D plot with the corresponding values of ω_r/ω_0 and ω_g/ω_0 marked on the x and y axis of the same plot. Figure 2.10 shows the resulting plot of this optimization procedure when $\omega_m/\omega_0 = 14$. When the bandwidth for all sets is calculated, the optimal set of ω_r/ω_0 and ω_g/ω_0 is chosen from the point that is the maximum. For example, the optimal values for $\omega_m/\omega_0 = 14$ in Figure 2.10 are $\omega_r/\omega_0 = 3.2$ and $\omega_g/\omega_0 = 0.75$, which results in a bandwidth of 181%.

By repeating the same optimization procedure for different ω_m/ω_0 ratios, we found

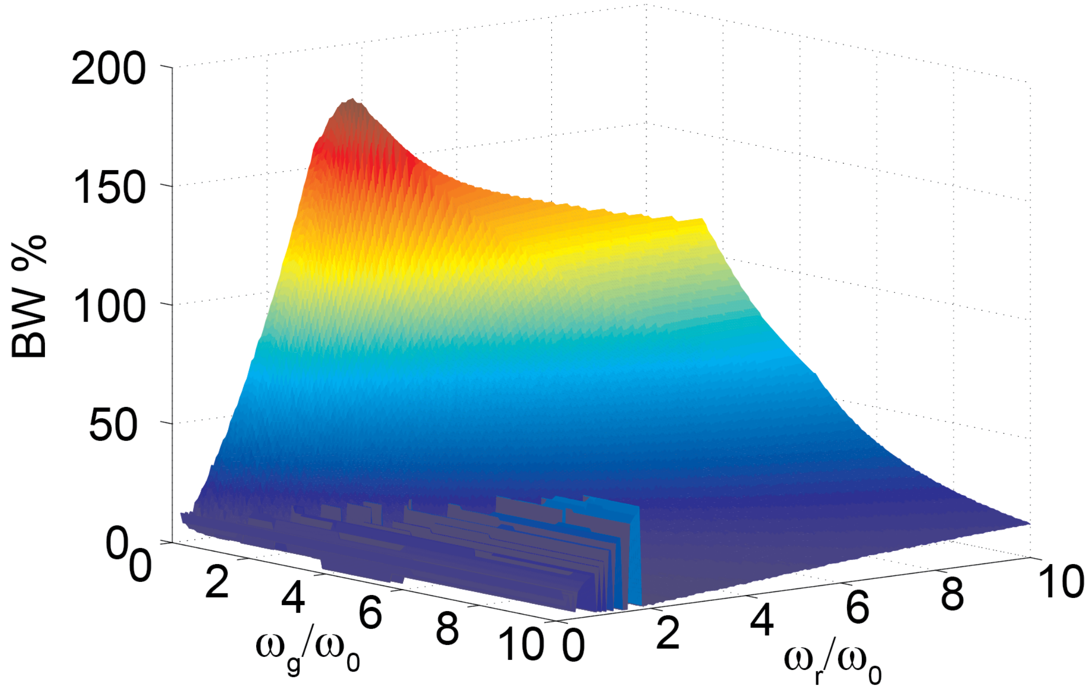

Figure 2.10: An optimization result when $\omega_m/\omega_0 = 14$.

the following design results in the widest bandwidth:

$$\begin{aligned}\omega_m/\omega_0 &= 118\\ \omega_r/\omega_0 &= 8.7\\ \omega_g/\omega_0 &= 2\\ f_a/f_0 &= 0.34\\ f_b/f_0 &= 1.00\\ BW &= 193.8\%. \end{aligned} \tag{2.2.50}$$

Therefore, based on the ideal model, bandwidths near 200% are technically achievable. Whether an actual circulator can achieve such high bandwidth values is the subject of the ensuing discussion. In fact, we believe that the optimal value of ω_m/ω_0 approaches infinity, albeit very slowly, in the search algorithm with almost no change in the bandwidth result.

By using the normalized Z-parameters of the crossover network in Eqns. (2.2.33), (2.2.42) and (2.2.47), we can choose any frequency band of interest. For our research we are interested in the frequency range 225-400 MHz and set $\omega_0 = 800\pi$ r/s along with

$L_0 = 1$ nH. From the ratios of Eqn. (2.2.50), we find that

$$\begin{aligned} 4\pi M_s &= 16,857 \text{ G} \\ C_0 &= 2.1 \text{ pF} \\ C_g &= 39.6 \text{ pF} \\ f_a &= 136 \text{ MHz} \\ f_b &= 400 \text{ MHz} \\ BW &= 193.8\%. \end{aligned} \tag{2.2.51}$$

Figure 2.11 shows a plot of $Z_{cm}/(\omega_0 L_0)$ for this design. If we constrain $4\pi M_s$ to a realizable value for practical applications (e.g., $4\pi M_s = 2,000$ G), a 180% maximum bandwidth is still achieved for the design frequency range. The results for this case are

$$\begin{aligned} 4\pi M_s &= 2,000 \text{ G} \\ C_0 &= 16 \text{ pF} \\ C_g &= 323 \text{ pF} \\ f_a &= 143 \text{ MHz} \\ f_b &= 400 \text{ MHz} \\ BW &= 180\%. \end{aligned} \tag{2.2.52}$$

With the optimal crossover network so determined, the last step is to calculate the value of the matching components C_1 and L_1. The reactance created by the components C_1 and L_1 approximate the circulation reactance X_{cm} through resonance. They can be estimated by recognizing that the slope of X_{Mat} through resonance is $2L_1$; from this value and the resonant frequency, C_1 can be estimated. That is,

$$L_1 \approx \frac{1}{2} \frac{X_{cm\_b} - X_{cm\_a}}{2\pi(f_b - f_a)} \tag{2.2.53}$$

and

$$C_1 = \frac{1}{(2\pi f_r)^2 L_1}, \tag{2.2.54}$$

where X_{cm_a} and X_{cm_b} are values of the circulation reactance at frequencies f_a and f_b, respectively, and f_r is the frequency at which X_{cm} crosses zero. Also, as mentioned before,

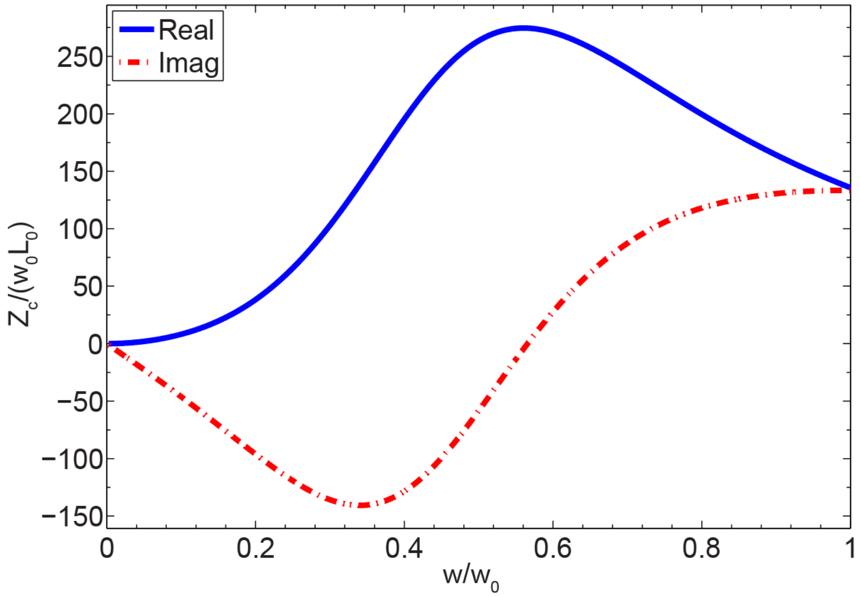

Figure 2.11: A plot of $Z_{cm}/(\omega_0 L_0)$ verses frequency for the widest bandwidth performance design.

the load R_L is estimated to be 2/3 of the peak value of R_{cm} for a 14 dB isolation and return loss. These estimations for L_1, C_1 and R_L are excellent seed values when searching for the optimal values. An optimization algorithm is invoked that uses this set of seed values and employs the Pareto Front population analysis [23] to find the optimal set. The optimization method is based on the following steps: a) Search for values of every component of the matching network; b) calculate minimum isolation and minimum return loss of the circulator over the frequency range f_a to f_b for every solution and plot these isolations and return losses on a Pareto population chart; c) choose a design point from the chart that meets the specified requirements.

By applying this algorithm to the 400 MHz crossover network associated with Eqn. (2.2.51), we obtain the Pareto population chart shown in Figure 2.12. The optimal matching network associated with this chart is chosen and the corresponding component values are

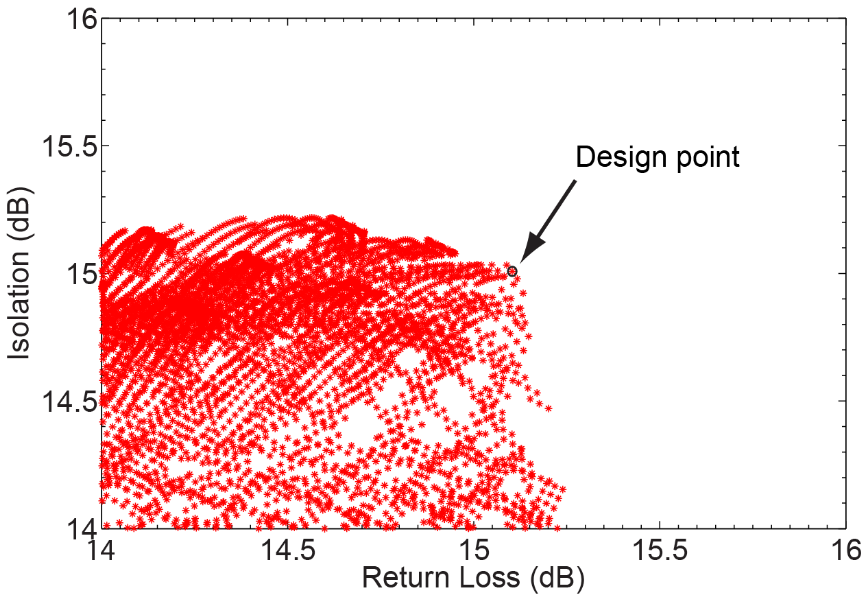

Figure 2.12: A Pareto population chart showing all possible matching network solutions.

$$
\begin{aligned}
C_0 &= 2.13 \text{ pF} \\
C_g &= 40.2 \text{ pF} \\
C_1 &= 5.98 \text{ pF} \\
L_1 &= 82.9 \text{ nH} \\
R_L &= 189.3\ \Omega. \qquad (2.2.55)
\end{aligned}
$$

The corresponding frequency response of this circulator device is shown in Figure 2.13. A performance with 15 dB isolation, 15.1 dB return loss and 0.3 dB insertion loss is obtained over the frequency band 136 MHz to 400 MHz, which is consistent with the 194% bandwidth predicted by Eqn. (2.2.51).

2.3 Actual Circulator Device Optimization

The previous section provides the necessary insight on wide-band operation of a ferrite circulator using an ideal model. For actual circulator hardware the model fails, but the bandwidth optimizing procedure (i.e., using the circulation impedance as a metric to determine bandwidth) is still applicable. For actual hardware, a better model, and

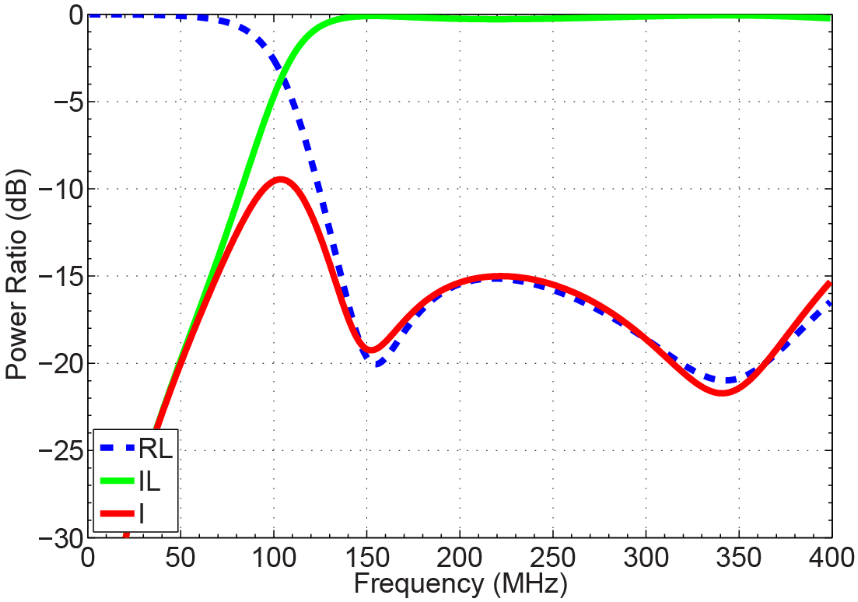

Figure 2.13: Frequency response of an ideal circulator optimized for widest bandwidth when $f_b = 400$ MHz.

hence a better estimate of the Z-parameters, can be obtained from numerical simulation, say using the popular electromagnetic solver HFSS [28]. Following the same procedure developed for the ideal model, we discovered through simulation that a bandwidth of 125% (i.e., 178-400 MHz) is indeed possible when $4\pi M_s = 3275$G. When fabricated and tested, we measured a 129% bandwidth (175-400 MHz). Figure 2.14 shows a picture of the fabricated circulator (the ferrite disks are from Trans-Tech, part No. TTVG-1850) and the HFSS simulation model. The frequency response comparison between data obtained from measurement and simulation is shown in Figure 2.15. Although both simulation and experimental data failed to achieve the ideal value of 194%, this is to be expected due to the many deficiencies associated with the ideal model. More importantly, the optimizing method proved to be a success by achieving unprecedented bandwidth performance.

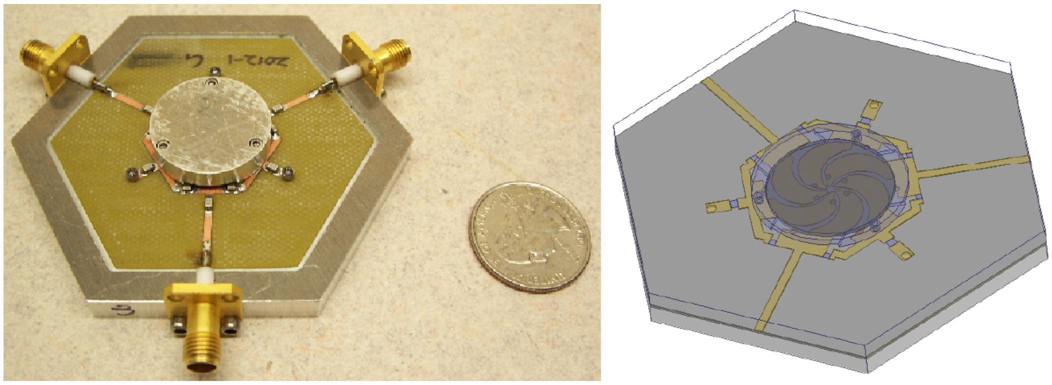

Figure 2.14: The fabricated circulator device and the HFSS model.

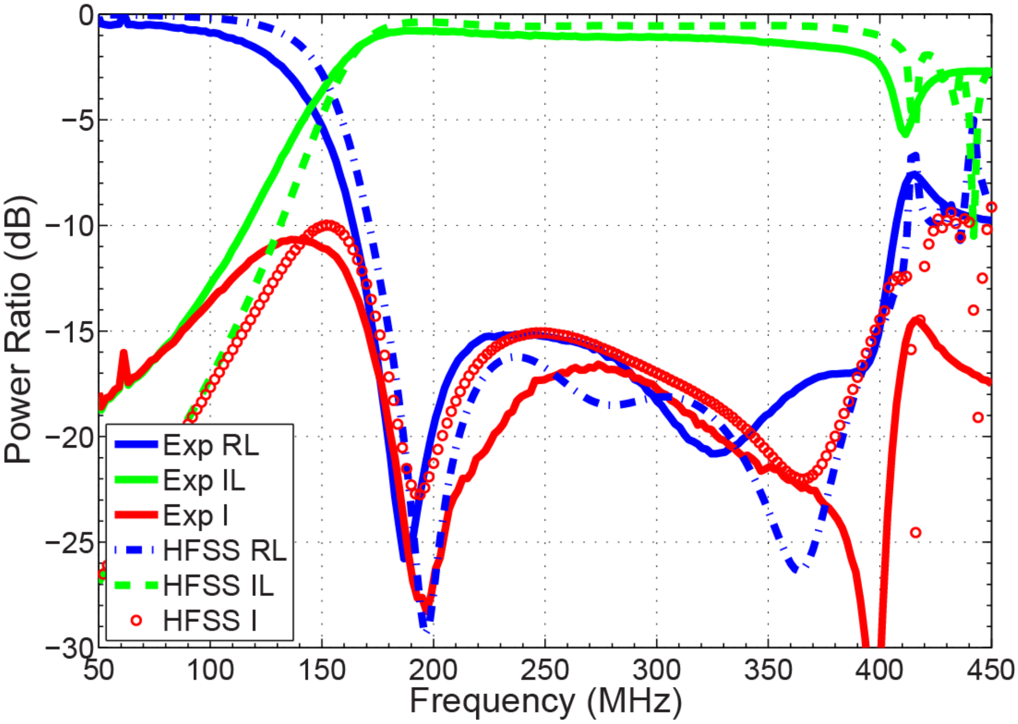

Figure 2.15: Frequency response comparison between data obtained from experiment (Exp) and from simulation (HFSS) when $f_b = 400$ MHz.

CHAPTER 3

A NOVEL CENTER TRACE TOPOLOGY FOR BROAD-BAND AND HIGH-ISOLATION PERFORMANCE

3.1 Introduction

In the previous chapter, our focus was on the maximum bandwidth of a idealized lumped-element ferrite circulator. In this chapter, we propose a new spiral center conductor topology for the lumped-element, crossover circulator and discuss the improvement on the performance of the circulator brought about by this new topology. We use both simulation and laboratory-measurement data to verify this performance enhancement.

3.2 Spiral Trace Geometry Optimization

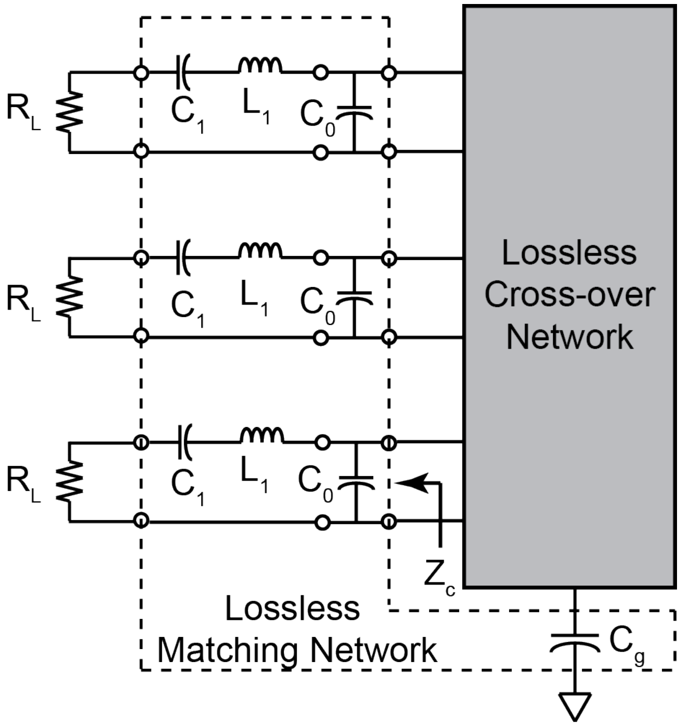

Figure 3.1: Three parts of a typical circulator.

Recall what was covered in the previous chapter. The structure of a typical circulator consists of three parts, as depicted in Figure 3.1: a) the crossover network, which is constructed by two fully saturated ferrite disks and three electrically isolated traces

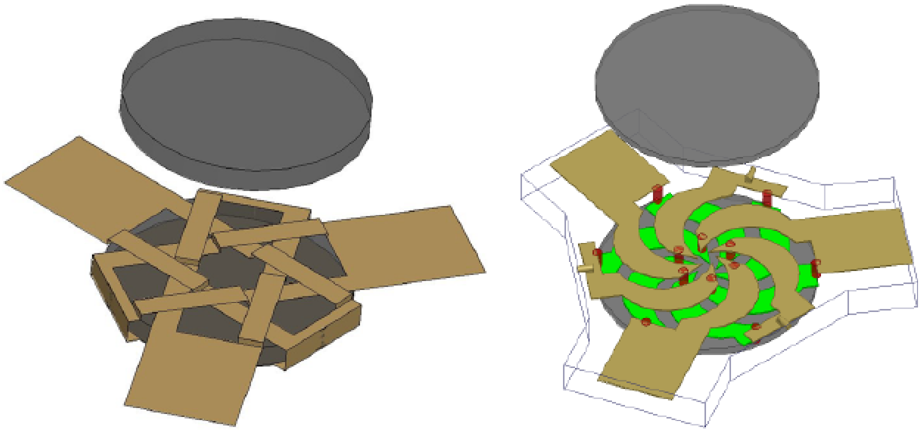

Figure 3.2: Comparison of Konishi crossover trace (left) and novel spiral trace (right) topologies.

between them; b) the tuning elements C_0 and C_g, which set the center frequency of the device and impact device bandwidth; c) the matching network components C_1 and L_1, which establish an impedance match with the load R_L. Among these parts, the ferrite crossover network is the key assembly responsible for non-reciprocal signal behavior; it controls the bandwidth and isolation properties of the circulator, which are the two key metrics associated with circulator design.

The trace topology widely used in circulator devices was first devised by Konishi [2] and depicted in Figure 3.2 (left). The approaches to the design, optimization and fabrication of a wideband, lumped-element circulator with this standard crossover geometry have been discussed by Mr. Brandon Aldecoa and Mr. Jacob Smith for UHF and VHF band applications [24][25]. In this section we introduce a novel spiral trace geometry for the circulator device operating in UHF frequency range. We seek to optimize the spiral topology of Figure 3.2 (right) to obtain deep isolation while keeping the bandwidth relatively wide.

Similar to what we did with the ideal circulator model, the optimization of the new trace topology is accomplished using the notion of circulation impedance Z_c, which is defined as the load impedance that results in perfect circulation for a lossless, non-reciprocal, three-port network. Rewriting Eqn. (3.2.1), we have,

$$Z_c = R_c + jX_c = \frac{Z_{21}^2}{Z_{31}} - Z_{11}. \tag{3.2.1}$$

The capacitances of C_g and C_0 in Figure 3.1 adjust the operating frequency band of the crossover network by turning Z_c into a post-tuned impedance Z_{cm}. Then C_1, L_1 and R_L are adjusted to approximate this Z_{cm} over a band of frequencies, say from f_a to f_b. How well this is accomplished determines the actual values of insertion loss, return loss and isolation of the device. The bandwidth of the circulator device is predicted from Z_{cm} by selecting the frequency points of its imaginary part where the slope changes direction. Since for the spiral trace topology we seek to achieve return loss and isolation values in excess of 30 dB over the operating band, we re-define the bandwidth prediction from Z_{cm} by adding the following two restrictions:

1. The bandwidth should be within the frequency band limited by the two zero-slope points of the X_{cm} curve.
2. For the real part of Z_{cm}, the slope (say k_a) of the line connecting the lower limit and the center point of bandwidth should be approximately equal to the slope (assumed as k_b) of the line between the upper limit and center point, and both of them should have a small angel with the frequency axis. See Figure 3.3.

The first restriction is to ensure that the matching network (C_1 and L_1) response coincides with X_{cm} in the band $f_a < f < f_b$, and the second restriction is necessary for the resistive load R_L to approximate the real part of Z_{cm} perfectly in the same range. When these two conditions are satisfied for the cross-over network, an isolation and return loss greater than 30 dB can be achieved in the operating bandwidth.

The understanding of the new bandwidth definition is aided by Figure 3.3. In this figure, BW_{spi} is the estimated bandwidth in which a 30 dB return loss and isolation is possible for the spiral trace topology and k_a, k_b are the slopes from second restriction. These slopes describe the flatness of R_c in the operating band.

3.2.1 Geometry Optimization

For this new trace topology configuration, the traces on top (indicated by brown) and the traces on bottom (indicated by green) are crossing over at the center using short bond wires (indicated by red) that reduce mutual capacitance. The spiral traces tend to cover the entire surface area of the ferrite disks to enhance RF field coupling to the ferrite material and to maximize mutual inductive coupling between the traces.

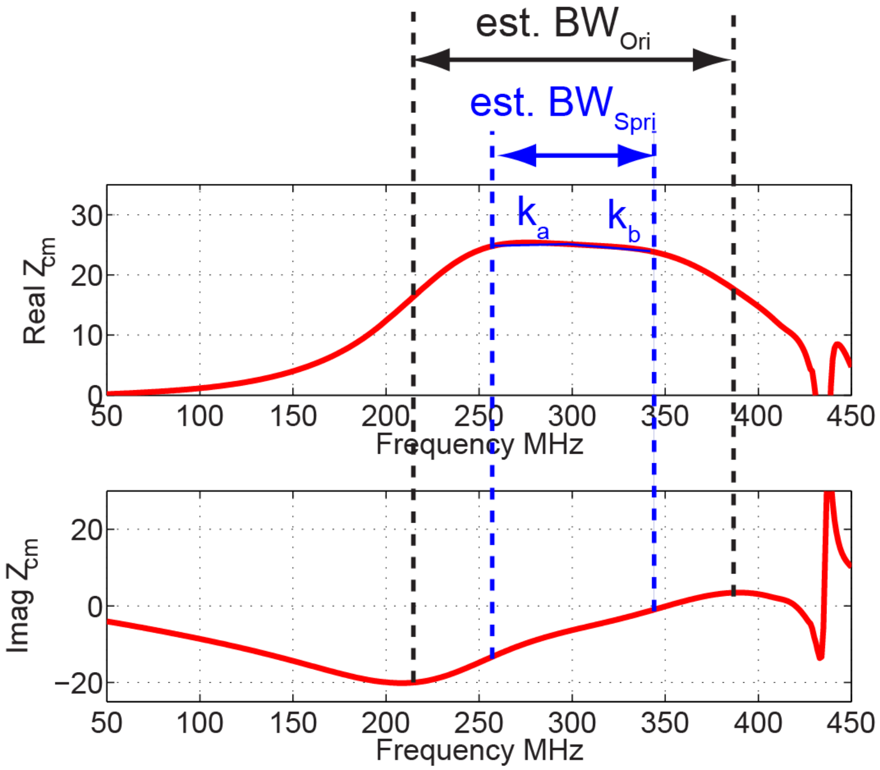

Figure 3.3: The estimated bandwidth of spiral trace topology for 30 dB isolation.

As shown in Figure 3.4, there are six geometrical parameters that define the spiral layout (only one trace is shown for clarity):

$$
\begin{aligned}
X_1 &: \text{ Ferrite disk height}\\
X_2 &: \text{ Ferrite disk radius}\\
X_3 &: \text{ PCB thickness}\\
X_4 &: \text{ Width of the spiral}\\
X_5 &: \text{ Trace width}\\
X_6 &: \text{ Trace length.}
\end{aligned}
\tag{3.2.2}
$$

Furthermore, two additional parameters define the properties of the ferrite, namely, the internal field H_o and the magnetic saturation $4\pi M_s$. These eight parameters form the optimization search space.

The optimization procedure searches through this space and attempts to find the parameter combination that gives maximum bandwidth performance. The process uti-

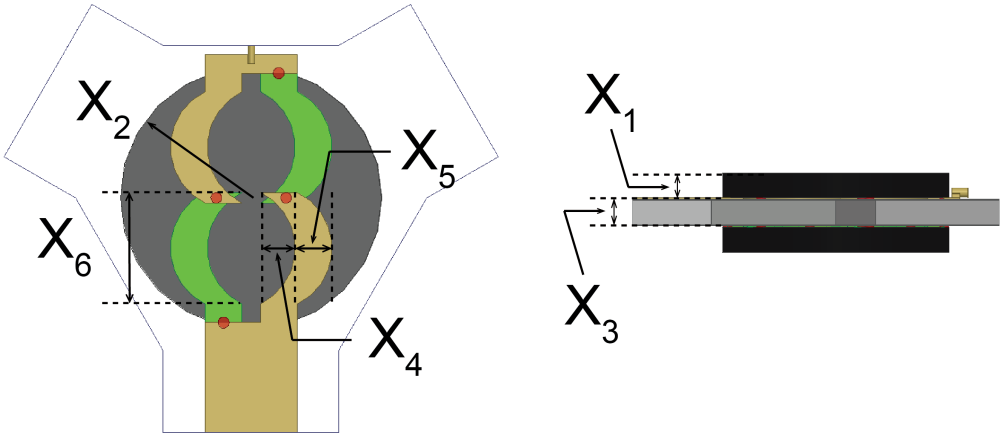

Figure 3.4: Physical parameters of the spiral trace topology. One trace is shown for clarity.

lizes a modified form of Powell's method as algorithm to control the HFSS simulation of a crossover network with different geometrical designs. Once the simulations are finished, the optimizer predicts the bandwidth of the network from its circulator impedance, changes the geometry parameters and then runs a new simulation. The optimizing procedure repeatedly does these steps until the estimated bandwidth reaches its peak value.

3.2.2 Spiral Trace Design for 400 MHz Application

By using the 30 dB isolation bandwidth definition as a criterion, we applied the optimization procedure to the UHF frequency band and found that the following ferrite crossover network parameter set resulted in broad-band performance in the range of 225 to 400 MHz:

$$\begin{aligned} X_1 &= 0.5 \text{ mm}, \\ X_2 &= 7.13 \text{ mm}, \\ X_3 &= 0.5 \text{ mm}, \\ X_4 &= 1.9 \text{ mm}, \\ X_5 &= 2.8 \ \text{ mm}, \\ X_6 &= 6.1 \ \text{ mm}, \\ 4\pi M_s &= 1800 \text{ G}, \\ H_o &= 142.86 \text{ Oe}, \end{aligned} \tag{3.2.3}$$

with tuning elements given by

$$C_0 = 34 \text{ pF}, \quad C_g = 197 \text{ pF}. \tag{3.2.4}$$

The Z_{cm} calculated from simulated data is shown in Figure 3.5 by solid lines. For comparison, we optimized a traditional crossover network that has same ferrite disk dimension. The simulated Z_{cm} data of this crossover network are shown in Figure 3.5 using dashed lines.

The improvement brought about by the spiral trace geometry over the traditional Konishi geometry is understood by examining the two circulation impedance data sets of Figure 3.5. Recall that the circulation impedance Z_{cm} ($Z_{cm} = R_{cm} + jX_{cm}$) is the load impedance needed by the post-tuned crossover network to achieve perfect circulation. Ideally, the matching network and the load R_L of Figure 3.1 create an impedance Z_{Mat} (i.e., $Z_{Mat} = R_{Mat} + jX_{Mat} = R_L + j\omega L_1 + 1/j\omega C_1$) that matches Z_{cm} over a range of frequencies from f_a to f_b. Through resonance, X_{Mat} produces a positive slope that matches the positive slope characteristic of X_{cm} for both the Konishi and spiral topologies, which suggests that the match between R_{cm} and R_{Mat} determines device performance. Since the resistive load R_L is frequency independent, R_{cm} must also be designed to have frequency independence over the range f_a to f_b to obtain a good agreement with R_L. Clearly, the spiral geometry achieves this requirement better than the Konishi geometry when the range f_a to f_b is within the frequencies in which X_{cm} has positive slope. Clarification of this discussion is aided using Figure 3.6 by showing optimized Z_{Mat} data superimposed on

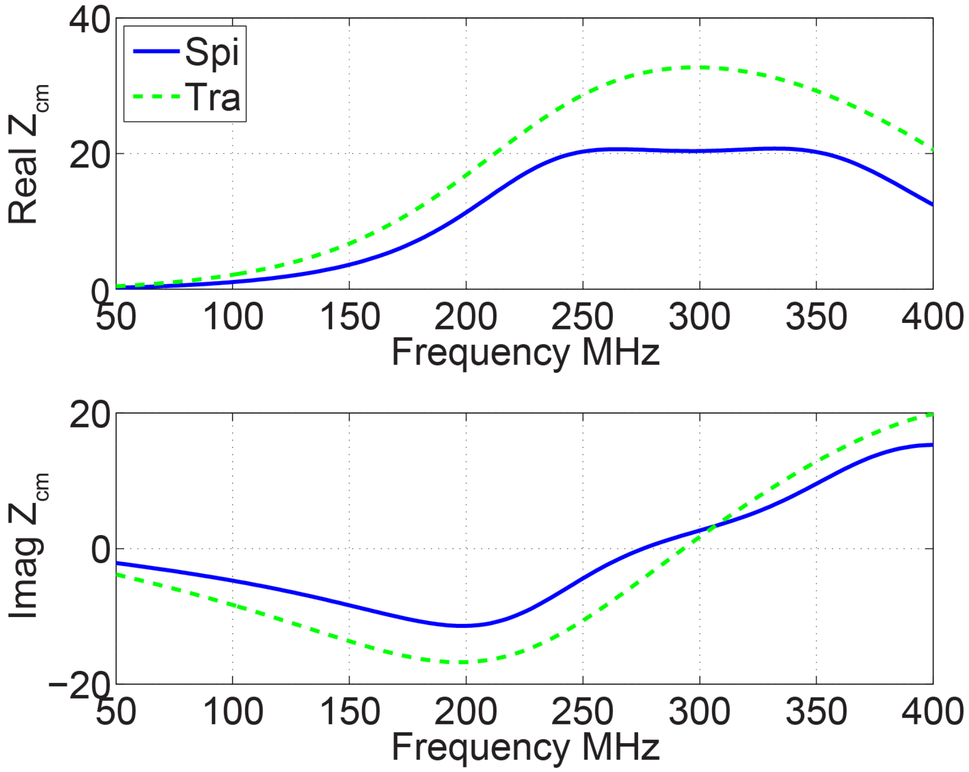

Figure 3.5: Simulated Z_{cm} data comparison between the optimal spiral and traditional trace geometries.

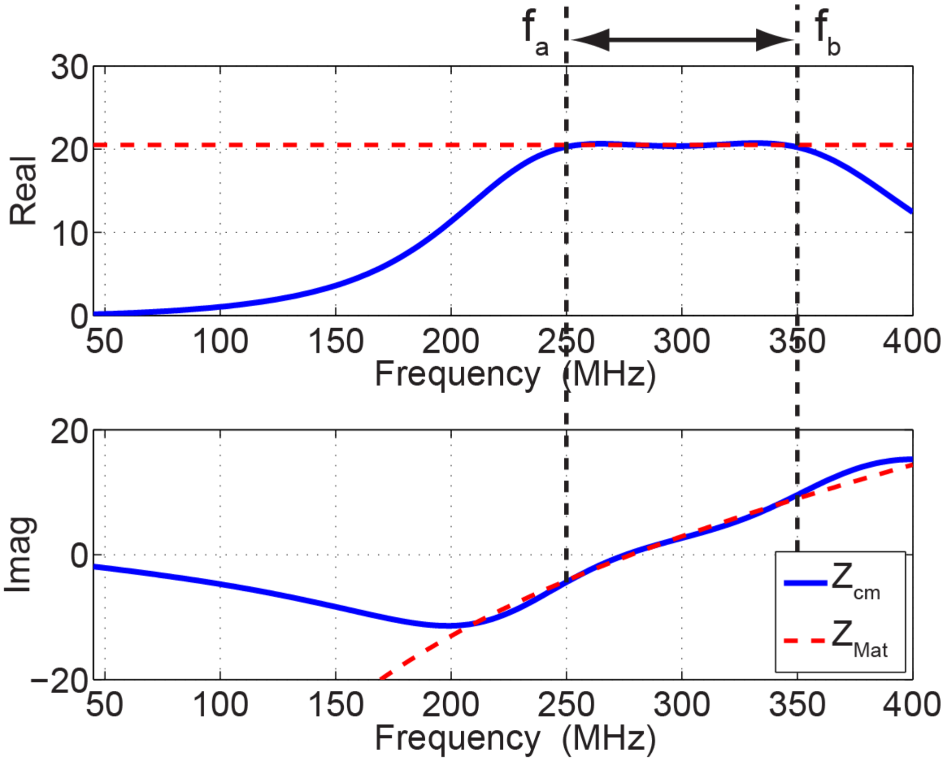

Figure 3.6: Simulated data comparison of Z_{cm} and Z_{Mat}. The estimated bandwidth (BW) for high isolation is also included.

Z_{cm} data for the spiral geometry. The high degree of correlation between these two data sets in the range of 250 to 350 MHz is seen and it is this correlation that produces high isolation performance. Thus, the optimization algorithm is constructed so that it chooses those designs that keep R_{cm} flat over the widest range of frequencies.

Once the trace dimensions are determined, the values of the matching network are calculated by employing the Pareto front algorithm discussed in the previous chapter. The resulting values are

$$R_L = 20.5\ \Omega, \quad C_1 = 29.5\ \text{pF}, \quad L_1 = 11.2\ \text{nH}. \tag{3.2.5}$$

The simulated frequency response of the circulator device, which consists of the spiral network, tuning elements and matching network, is shown in Figure 3.7 by solid lines. We see for 30 dB isolation the circulator has a bandwidth from 240 MHz to 355 MHz, which is in agreement with the data of Figure 3.6. The maximum insertion loss in this bandwidth is 0.3 dB. Also plotted in Figure 3.7 is the frequency response of the Konishi crossover

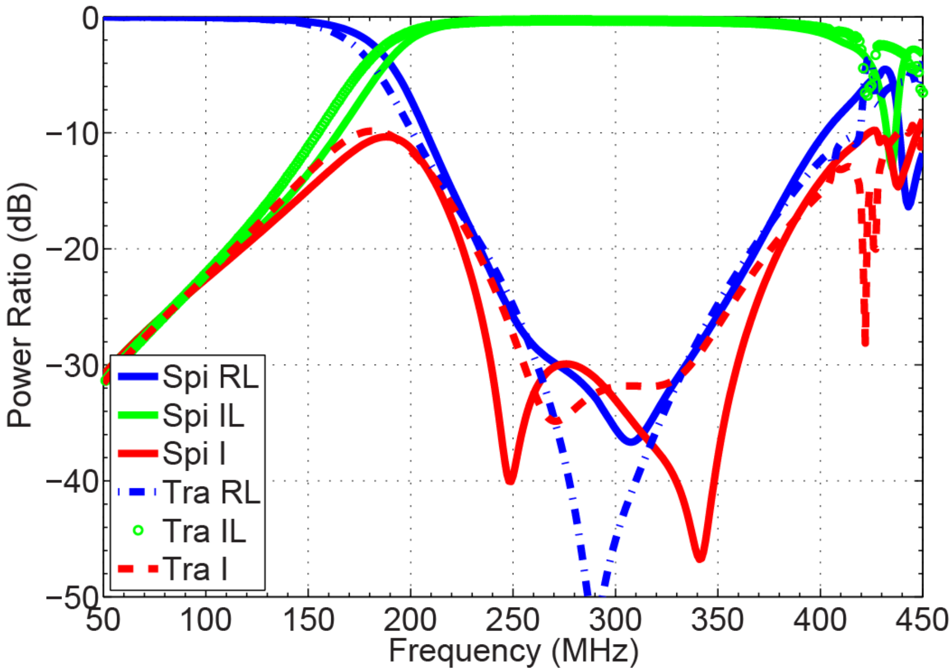

Figure 3.7: Simulated frequency response comparison between the spiral trace circulator and the traditional Konishi circulator.

network used for comparison when a corresponding matching network is designed. A narrower 30 dB isolation bandwidth (260–330 MHz) is observed from the figure, which is also consistent with the prediction from the comparison data of Figure 3.5.

3.3 Experimental Results

We fabricated and measured a circulator in laboratory to verify the simulated performance of the spiral trace topology. To have a circulator that can be fabricated, we redid the optimization on the spiral trace topology by considering only ferrites that are available in the open market. As a result, we found that within the 225 to 400 MHz band the

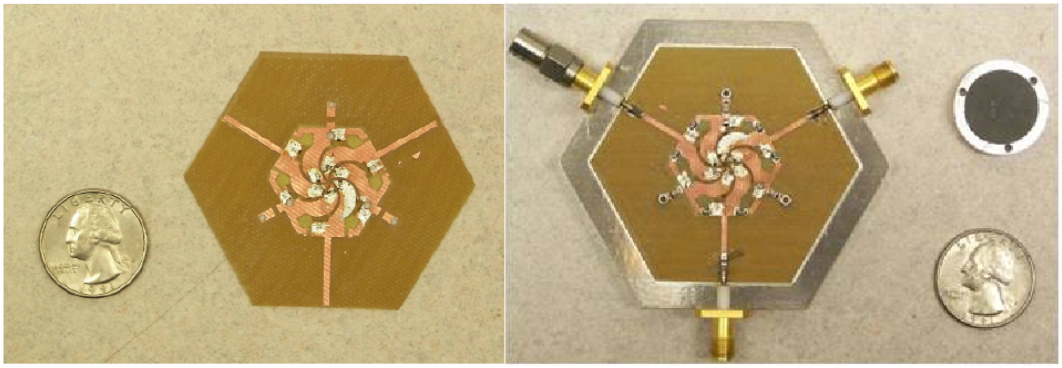

Figure 3.8: The fabricated spiral trace geometry crossover network (left); the crossover network with tuning elements (right).

following ferrite crossover parameter set has excellent device performance :

$$\begin{aligned} X_1 &= 0.58 \text{ mm}, \\ X_2 &= 8.93 \text{ mm}, \\ X_3 &= 14 \text{ mil}, \\ X_4 &= 2.4 \text{ mm}, \\ X_5 &= 3.5 \ \text{ mm}, \\ X_6 &= 8.2 \ \text{ mm}, \\ 4\pi M_s &= 1850 \text{ G}, \\ H_o &= 142.86 \text{ Oe}. \end{aligned} \tag{3.3.1}$$

The corresponding optimized tuning capacitors are

$$C_0 = 20 \text{ pF} \quad C_g = 168 \text{ pF}. \tag{3.3.2}$$

For the spiral trace network and tuning-elements C_0 and C_g, we used the design values from Eqns. (3.3.1) and (3.3.2). The ferrite disks are TTVG-1850 from Trans-Tech. An external field of 1630 Gauss was applied to force them into saturation. A picture of the fabricated crossover network is shown on the left side of Figure 3.8 and on the right side of the figure is the crossover network with tuning elements.

For the matching network and the resistive load, instead of using simulation-determined values, we determine their values based on measured data of the fabricated crossover network in Figure 3.8. This is necessary since the HFSS model idealizes certain aspects of the

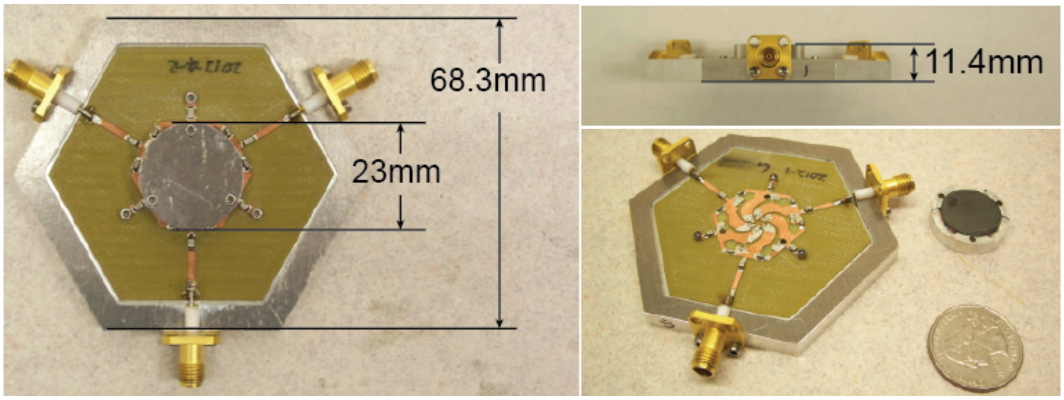

Figure 3.9: The fabricated spiral trace circulator.

device (e.g., homogeneous internal biasing field) to improve performance and creates ports for the lumped-element components that are not directly simulated. After modification, the values are:

$$R_L = 17\ \Omega, \quad C_1 = 56\ \text{pF}, \quad L_1 = 3.8\ \text{nH}. \tag{3.3.3}$$

The capacitors were implemented by lumped-element components and the inductors were embedded in the transmission lines on the printed circuit board (PCB). Pictures of the resulting device are shown in Figure 3.9 and its measured frequency response is shown in Figure 3.10 using dashed lines. It can be seen that a bandwidth associated with 30 dB isolation and 0.7 dB insertion loss is achieved from 260 MHz to 390 MHz. The frequency response of a simulated circulator is replotted in Figure 3.10 to show the good correlation between the measured and simulated data.

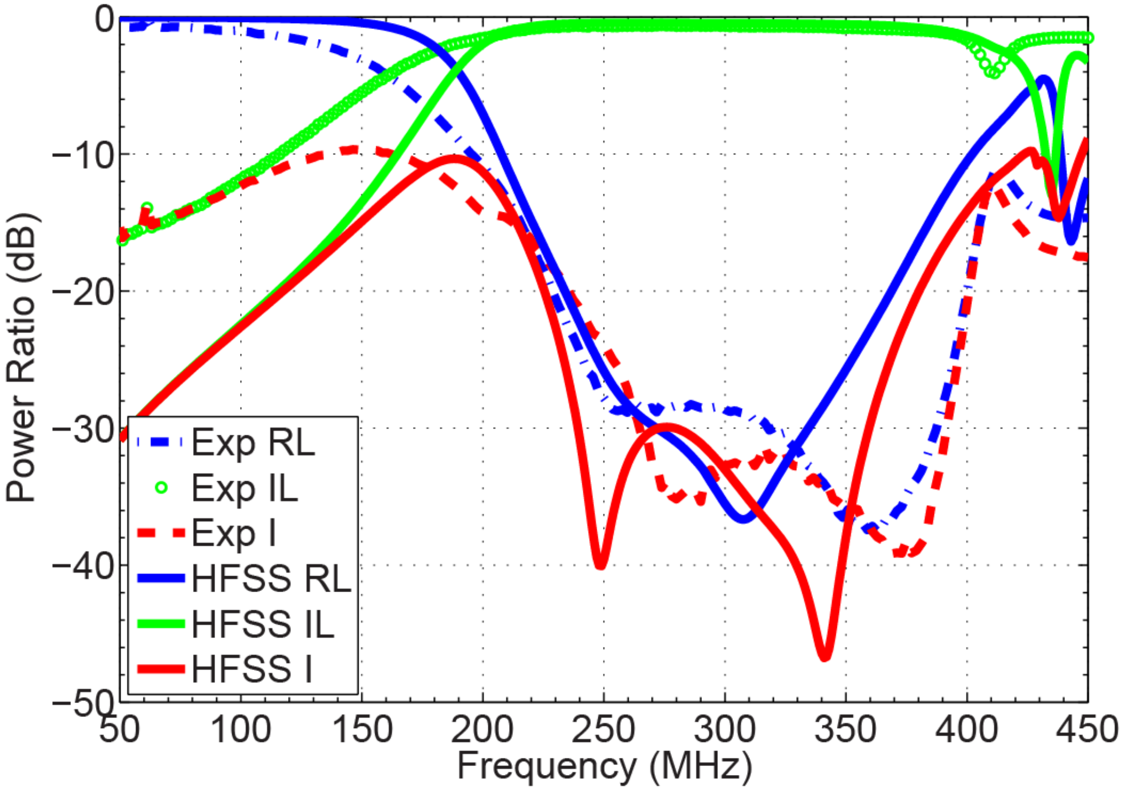

Figure 3.10: Simulated and measured frequency response of a spiral trace circulator for high isolation.

CHAPTER 4

CONNECTOR CHARACTERIZATION AND DE-EMBEDDING

4.1 Introduction

From the previous chapter we saw that a circulator used microstrip lines as its microwave network ports in HFSS simulations so that the impedance or transmission parameters of the network could be calculated from the electromagnetic field distribution at these ports. When fabricated devices are considered, measurement fixtures are needed to obtain the S or Z parameters of the circulator device. In University of Idaho (UI) Applied Electromagnetic Waves Laboratory (AEMWL), we use the Agilent E8363A programmable network analyser, which has two 3.5 mm male ports at the measurement interface. This means to obtain the response of the circulator device, we first need a transition between the interface on the network analyser and the port of the circulator.

Connectors are widely used as this type of transition. A picture of the 3.5mm connector that was used in our circulator measurement procedure is shown in Figure 4.1. Figure 4.2 shows one of the circulator ports connected to a measurement equipment port.

Consider a two-port network analyser to measure the frequency response of a two-port network. With the connectors on its ports, the measurement obtained by the network analyser is not the response of the two-port network. Instead, the analyser measures the S-parameters of a new network, which is composed of network as well as the two connector transitions. The structure of this new network is depicted in Figure 4.3. Therefore, to obtain the response of the device under test (DUT), we need to de-embed the connector from the measurement of the network analyser.

To accomplish the de-embedding procedure, we first need to characterize the connector. Several methods have been developed to assist this work, such as the T-shape circuit model method [24], the *Thru-Reflect-Line* (TRL) calibration technique [26], and the impedance parameters of transmission line method [27].

In this chapter we discuss the technique that was used in the circulator design work to characterize the connector transitions. It uses two passive two-port calibration devices as references to determine the frequency response of the connector. This frequency response

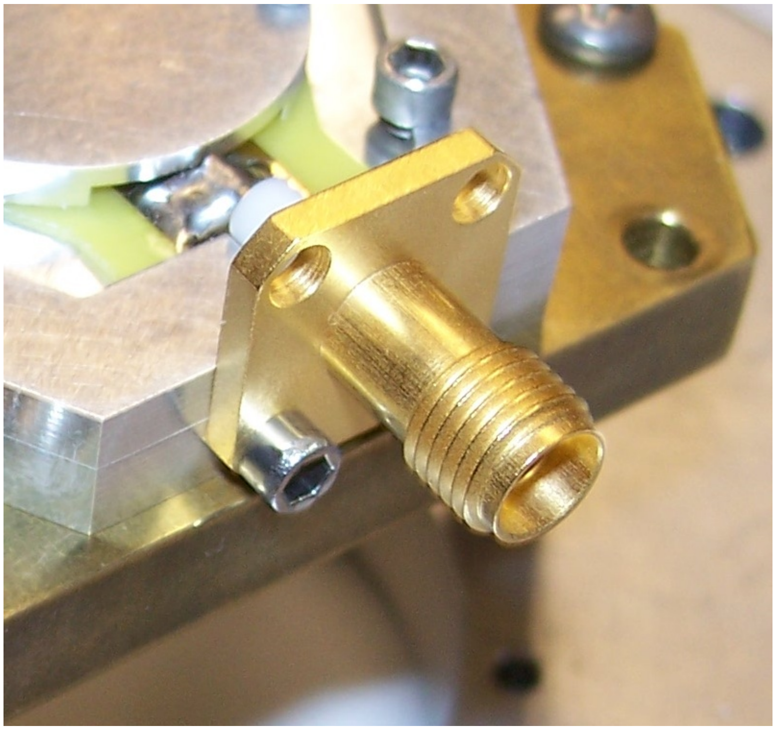

Figure 4.1: A typical 3.5mm connector.

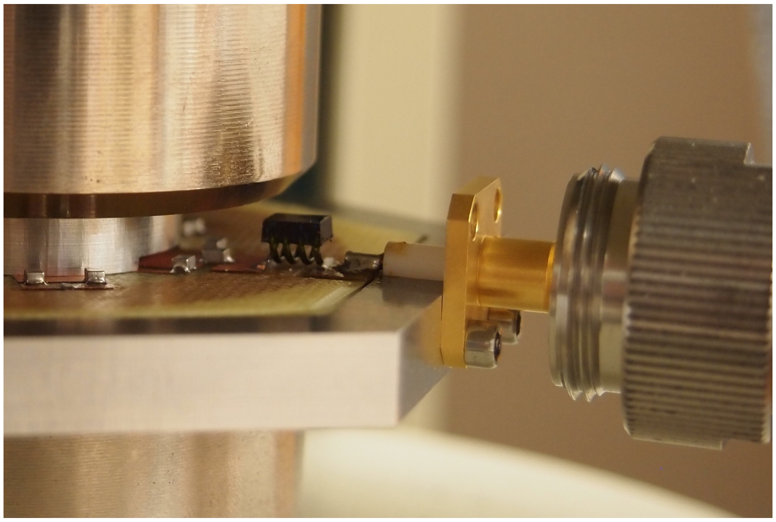

Figure 4.2: Connector used as a transition between the 3.5 mm coaxial cable and the microstrip line.

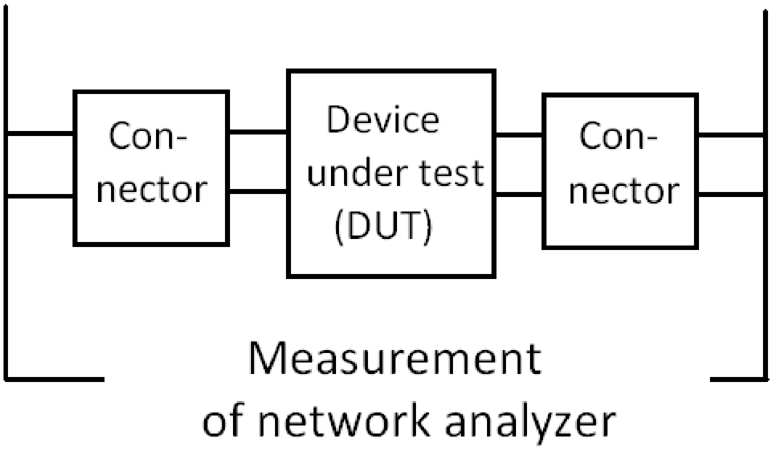

Figure 4.3: Depiction of the device under test (DUT) with connectors mounted on its ports.

is then used to factor out the influence of the connector mounted on the ports of the circulator.

4.2 Connector Transition Characterization

To characterize the connector transition, we need a calibration device N_{m1} that has the structure shown in Figure 4.4. The network N_{m1} is composed of three sections. The network N_1 is a two-port network whose frequency response is already known and expressed by the transmission matrix $[A_{d1}, B_{d1}; C_{d1}, D_{d1}]$. On the two ports of N_1 are the connectors we wish to characterize. They are assumed to be identical. If the transmission matrix of the connector on port one is expressed by $[A, B; C, D]$, then the transmission matrix of the connector on port two has a form of $[D, B; C, A]$ [26]. Since we can use a network analyser to measure the S-parameters of the calibration device N_{m1}, its frequency response can be calculated and expressed by $[A_{m1}, B_{m1}; C_{m1}, D_{m1}]$.

From the cascading property of the transmission matrix, we can write the following equation for the calibration device N_{m1}:

$$\begin{pmatrix} A_{m1} & B_{m1} \\ C_{m1} & D_{m1} \end{pmatrix} = \begin{pmatrix} A & B \\ C & D \end{pmatrix} \begin{pmatrix} A_{d1} & B_{d1} \\ C_{d1} & D_{d1} \end{pmatrix} \begin{pmatrix} D & B \\ C & A \end{pmatrix}. \tag{4.2.1}$$

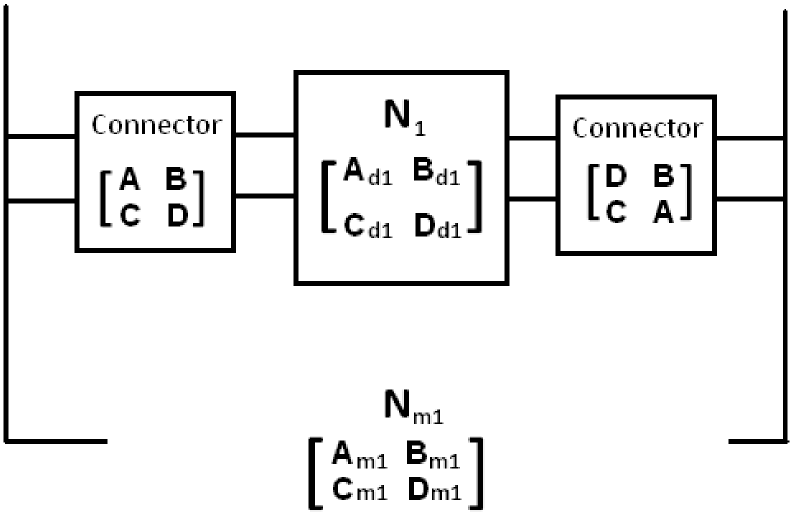

Figure 4.4: Topology of the calibration device.

Expansion of the right hand side of Eqn. (4.2.1) gives us

$$\begin{pmatrix} A_{m1} & B_{m1} \\ C_{m1} & D_{m1} \end{pmatrix} = \tag{4.2.2}$$

$$\begin{pmatrix} ADA_{d1} + BDC_{d1} + ACB_{d1} + BCD_{d1} & ABA_{d1} + B^2C_{d1} + A^2B_{d1} + ABD_{d1} \\ CDA_{d1} + D^2C_{d1} + C^2B_{d1} + CDD_{d1} & BCA_{d1} + BDC_{d1} + ACB_{d1} + ADD_{d1} \end{pmatrix}.$$

Considering each element in the matrix equation, we obtain

$$A_{m1} = ADA_{d1} + BDC_{d1} + ACB_{d1} + BCD_{d1} \tag{4.2.3}$$

$$B_{m1} = ABA_{d1} + B^2C_{d1} + A^2B_{d1} + ABD_{d1} \tag{4.2.4}$$

$$C_{m1} = CDA_{d1} + D^2C_{d1} + C^2B_{d1} + CDD_{d1} \tag{4.2.5}$$

$$D_{m1} = BCA_{d1} + BDC_{d1} + ACB_{d1} + ADD_{d1}. \tag{4.2.6}$$

Equation set (4.2.3) through (4.2.6) are second order equations of the unknowns A, B, C and D, but they are insufficient for solving for the unknowns. To address this problem, we set up another calibration device N_{m2} that has similar topology as N_{m1} but with a different middle section. This two-port network in the center of N_{m2} is N_2 and its transmission matrix is also known and expressed by $[A_{d2}, B_{d2}; C_{d2}, D_{d2}]$. Then similar to Eqns. (4.2.3) through (4.2.6), for N_{m2} we have

$$A_{m2} = ADA_{d2} + BDC_{d2} + ACB_{d2} + BCD_{d2} \tag{4.2.7}$$

$$B_{m2} = ABA_{d2} + B^2C_{d2} + A^2B_{d2} + ABD_{d2} \tag{4.2.8}$$

$$C_{m2} = CDA_{d2} + D^2C_{d2} + C^2B_{d2} + CDD_{d2} \tag{4.2.9}$$

$$D_{m2} = BCA_{d2} + BDC_{d2} + ACB_{d2} + ADD_{d2}. \tag{4.2.10}$$

We are now ready to solve the unknowns A, B, C and D. Consider the right-hand side of Eqn. (4.2.4); it can be simplified as

$$\begin{aligned} B_{m1} =& ABA_{d1} + B^2C_{d1} + A^2B_{d1} + ABD_{d1} \\ =& A^2\left[\frac{B}{A}A_{d1} + \left(\frac{B}{A}\right)^2 C_{d1} + B_{d1} + \frac{B}{A}D_{d1}\right] \\ =& A^2[B_{d1} + C_{d1}k^2 + (A_{d1} + D_{d1})k], \end{aligned} \tag{4.2.11}$$

where k is the factor between A and B such that

$$k = \frac{B}{A}. \tag{4.2.12}$$

Then from Eqn. (4.2.11), we have

$$A^2 = \frac{B_{m1}}{B_{d1} + C_{d1}k^2 + (A_{d1} + D_{d1})k}. \tag{4.2.13}$$

Similarly, from Eqn. (4.2.8) and Eqn. (4.2.12), we obtain

$$A^2 = \frac{B_{m2}}{B_{d2} + C_{d2}k^2 + (A_{d2} + D_{d2})k}. \tag{4.2.14}$$

Since A is property of the connector, its value will stay constant in both Eqn. (4.2.13) and Eqn. (4.2.14). This allows us to write

$$\frac{B_{m1}}{B_{d1} + C_{d1}k^2 + (A_{d1} + D_{d1})k} = A^2 = \frac{B_{m2}}{B_{d2} + C_{d2}k^2 + (A_{d2} + D_{d2})k}. \tag{4.2.15}$$

This equation yields the following quadratic equation for k

$$(B_{m2}C_{d1} - B_{m1}C_{d2})k^2 + [B_{m2}(A_{d1} + D_{d1}) - B_{m1}(A_{d2} + D_{d2})]k \\ + (B_{m2}B_{d1} - B_{m1}B_{d2}) = 0. \qquad (4.2.16)$$

As for the coefficients in Eqn. (4.2.16), A_{d1}, A_{d2}, B_{d1}, B_{d2}, C_{d1}, C_{d2}, D_{d1} and D_{d2}, they are already known from the transition matrices of the two middle sections N_1 and N_2. The coefficients B_{m1} and B_{m2} are calculated from the S-parameters of the two calibration devices N_{m1} and N_{m2}, which are measured by the network analyser. Therefore the roots k of Eqn. (4.2.16) can be calculated from

$$k_{1,2} = \frac{-b_k \pm \sqrt{b_k^2 - 4a_kc_k}}{2a_k}, \qquad (4.2.17)$$

where

$$\begin{aligned} a_k &= B_{m2}C_{d1} - B_{m1}C_{d2} \\ b_k &= B_{m2}(A_{d1} + D_{d1}) - B_{m1}(A_{d2} + D_{d2}) \\ c_k &= B_{m2}B_{d1} - B_{m1}B_{d2}. \end{aligned}$$

With the factor k known, we can calculate A and B. By inserting k_1 and k_2 into Eqn. (4.2.13), we obtain four possible solution sets for A and B; they are

$$\begin{aligned} A_1 &= \left[\frac{B_{m1}}{B_{d1} + C_{d1}k_1^2 + (A_{d1} + D_{d1})k_1}\right]^{\frac{1}{2}} \\ A_2 &= -\left[\frac{B_{m1}}{B_{d1} + C_{d1}k_1^2 + (A_{d1} + D_{d1})k_1}\right]^{\frac{1}{2}} \\ A_3 &= \left[\frac{B_{m1}}{B_{d1} + C_{d1}k_2^2 + (A_{d1} + D_{d1})k_2}\right]^{\frac{1}{2}} \\ A_4 &= -\left[\frac{B_{m1}}{B_{d1} + C_{d1}k_2^2 + (A_{d1} + D_{d1})k_2}\right]^{\frac{1}{2}} \end{aligned} \qquad (4.2.18)$$

and

$$\begin{aligned} B_1 &= k_1 A_1 \\ B_2 &= k_1 A_2 \\ B_3 &= k_2 A_3 \\ B_4 &= k_2 A_4. \end{aligned} \tag{4.2.19}$$

By applying a similar process using Eqn. (4.2.5) and (4.2.9), we obtain four possible solution sets for C and D, which are

$$\begin{aligned} C_1 &= \left[\frac{C_{m1}}{B_{d1} + C_{d1} m_1^2 + (A_{d1} + D_{d1}) m_1}\right]^{\frac{1}{2}} \\ C_2 &= -\left[\frac{C_{m1}}{B_{d1} + C_{d1} m_1^2 + (A_{d1} + D_{d1}) m_1}\right]^{\frac{1}{2}} \\ C_3 &= \left[\frac{C_{m1}}{B_{d1} + C_{d1} m_2^2 + (A_{d1} + D_{d1}) m_2}\right]^{\frac{1}{2}} \\ C_4 &= -\left[\frac{C_{m1}}{B_{d1} + C_{d1} m_2^2 + (A_{d1} + D_{d1}) m_2}\right]^{\frac{1}{2}}. \end{aligned} \tag{4.2.20}$$

Moreover,

$$\begin{aligned} D_1 &= m_1 C_1 \\ D_2 &= m_1 C_2 \\ D_3 &= m_2 C_3 \\ D_4 &= m_2 C_4, \end{aligned} \tag{4.2.21}$$

where m_i is the factor between C and D; that is, $m = D/C$, where

$$m_{1,2} = \frac{-b_m \pm \sqrt{b_m^2 - 4 a_m c_m}}{2 a_m}, \tag{4.2.22}$$

in which case

$$\begin{aligned} a_m &= C_{m2} C_{d1} - C_{m1} C_{d2} \\ b_m &= C_{m2}(A_{d1} + D_{d1}) - C_{m1}(A_{d2} + D_{d2}) \\ c_m &= C_{m2} B_{d1} - C_{m1} B_{d2}. \end{aligned}$$

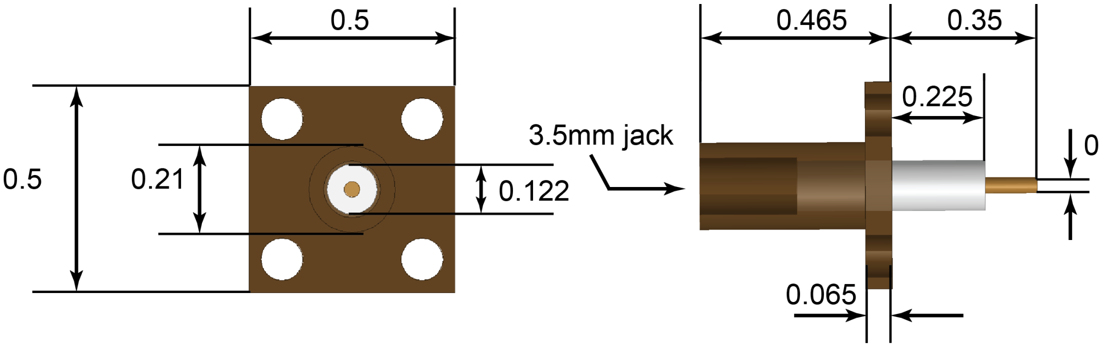

Figure 4.5: Physical dimensions of the connector. (All units are in inches.)

Having Eqns. (4.2.18) through (4.2.21), we have sixteen possible solution sets for the unknowns A, B, C and D. The next step is to select the “real” ones for the connector under investigation.

There are two conditions we use to distinguish the real solution set from the others. The first one is Eqn. (4.2.3). We insert each possible solution set into right-hand side of Eqn. (4.2.3) and compare the result against A_{m1}. For the genuine solution set the difference should be approximately equal to zero. Equations (4.2.7), (4.2.6) and (4.2.10) can also be used as the “check” equations of this method, which will give same selection as Eqn. (4.2.3) does.

The other condition is from the connector itself. As a reciprocal two-port network, the connector has a transmission matrix with the property

$$AD - BC = 1. \tag{4.2.23}$$

Therefore after having each possible solution set inserted into left side of above equation, we choose the one that gives result of 1 as the elements in transmission matrix of the connector.

4.3 Calculation Example

In this section, we utilize the mathematical method from previous section to characterize a hardware connector transition. The transition structure is composed of a connector and a microstrip transmission line with a width of 1.27mm. The physical dimensions of the connector are shown in Figure 4.5. The frequency range of interest is 50 to 450 MHz

(UHF band).

According to the derivation in previous section, we set up two calibration devices N_{m1} and N_{m2} with the connector transition mounted on their ends. As for their middle parts, we use a straight microstrip transmission line that has a width of 1.27mm, which is same width as the transmission line in the transition. There are two reasons we make this choice: 1), microstrip transmission lines have a simple geometry making them easy to fabricate and 2), the properties of the microstrip line, which need to be known in advance of the calculation, can be easily determined by either an ideal model or by simulation tools (e.g. HFSS [28]). Since the characterizing method asks for two different middle sections for the calibration kit, we implement this by making two microstrip lines of different lengths. Transmission line number 1 has length of 40mm and transmission line number 2 has length of 60mm. Pictures of the two calibration devices are shown Figure 4.6.

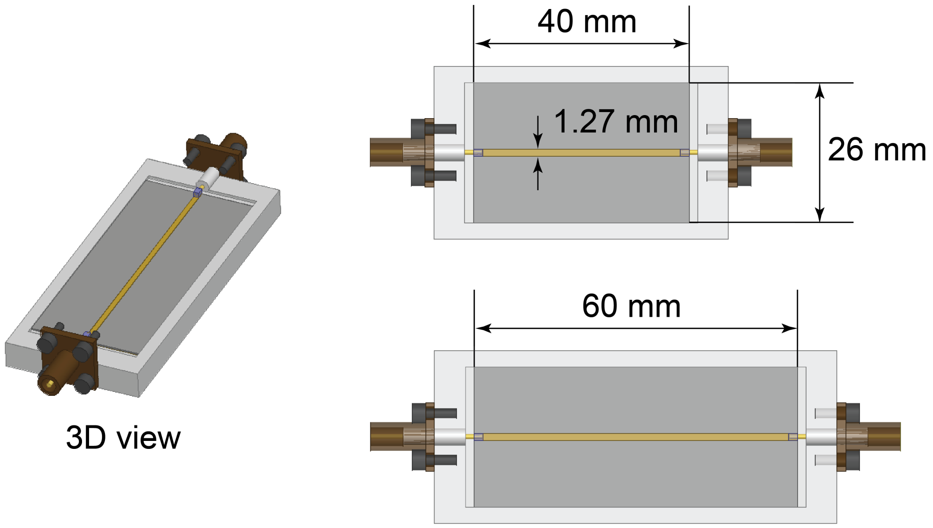

Figure 4.6: Two calibration devices with different microstrip lines as a middle section.

The ABCD matrices of the two calibration devices N_{m1} and N_{m2} and the two middle sections N_1 and N_2 can all be determined by HFSS simulations. Thus, the response of the transition can be calculated by using the method of the previous section. This response, as a function of frequency, is shown in Figure 4.7.

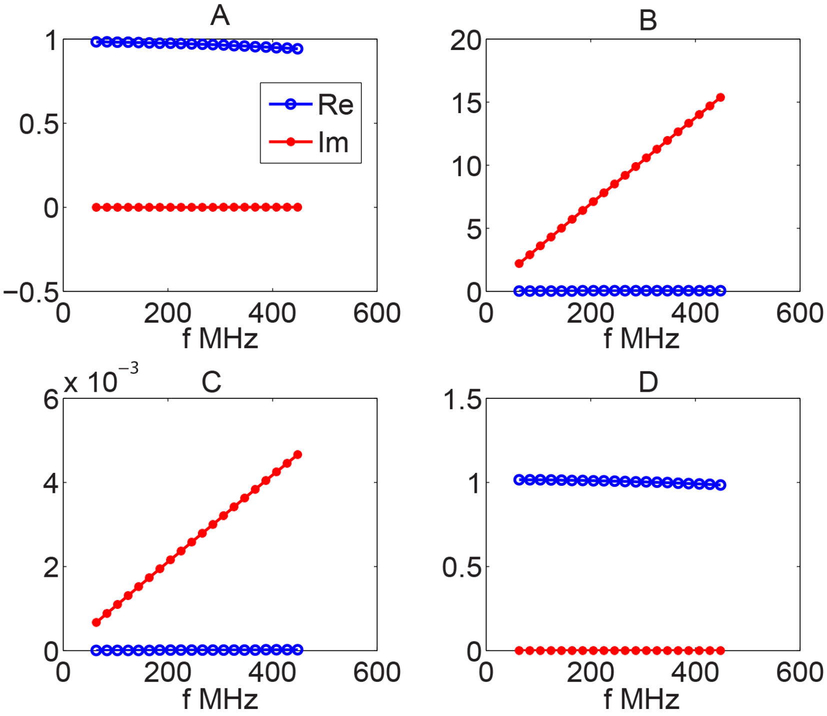

Figure 4.7: The ABCD parameters as a function of frequency for the connector transition.

4.4 Validation

To validate our method, we use another calibration device N_{m3}. It also uses the structure of Figure 4.3 with a known two-port network, namely N_3, as the middle section. On the ports of N_3 are the connectors we characterized from the previous section. Assuming the elements in transmission matrix of N_3 are A_{d3}, B_{d3}, C_{d3} and D_{d3}, we use the following steps to verify our connector characterizing method:

1. Utilizing the cascading connection property of the networks to calculate the ABCD matrix of N_{m3} from N_3 and the two connectors, we obtain

$$\begin{aligned}[ABCD]_{N_{m3-cal}} &= \begin{pmatrix} A_{m3-cal} & B_{m3-cal} \\ C_{m3-cal} & D_{m3-cal} \end{pmatrix} \\ &= \begin{pmatrix} A & B \\ C & D \end{pmatrix} \begin{pmatrix} A_{d3} & B_{d3} \\ C_{d3} & D_{d3} \end{pmatrix} \begin{pmatrix} D & B \\ C & A \end{pmatrix} . \end{aligned} \tag{4.4.1}$$

2. We directly measure the S parameters of N_{m3} and obtain its transmission matrix from measurement such that

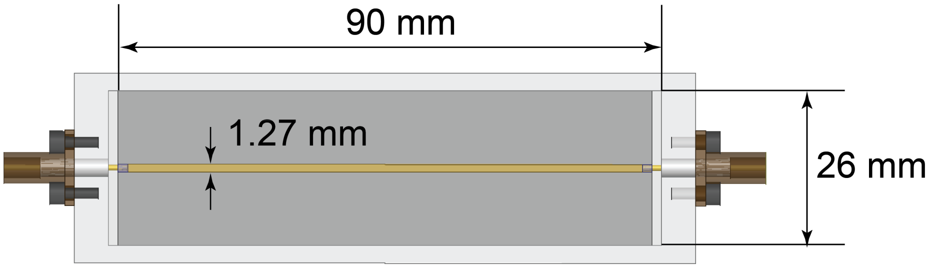

Figure 4.8: The device used in the validation procedure.

$$[ABCD]_{N_{m3-meas}} = \begin{pmatrix} A_{m3-meas} & B_{m3-meas} \\ C_{m3-meas} & D_{m3-meas} \end{pmatrix}. \tag{4.4.2}$$

3. We compare data to see if there are any differences between $[ABCD]_{N_{m3-cal}}$ and $[ABCD]_{N_{m3-meas}}$. If no difference is found, the ABCD parameters of the connector are accurate, which verifies the solution process of the previous section.

The simulation model of the calibration device N_{m3} that was used in the validation procedure is shown in Figure 4.8. The connectors are same as the ones used in the example from previous section and the middle section N_3 is a microstrip line with a length of 90mm.

Figure 4.9 shows the comparison between $[ABCD]_{N_{m3-cal}}$ and $[ABCD]_{N_{m3-meas}}$, i.e., the measured and calculated transmission matrices for N_{m3}. From this figure we observe a good agreement from the two results, which suggest our connector characterizing method is accurate.

4.5 Application to an UHF circulator

4.5.1 Connector De-embedding for a 3-port Network

Before de-embedding the influence of the connector from the measurement of a circulator, we need to derive the generalized procedure to de-embed a two-port network from the ports of a three-port network. The procedure can be accomplished by manipulating the Z-matrix of the three-port network.

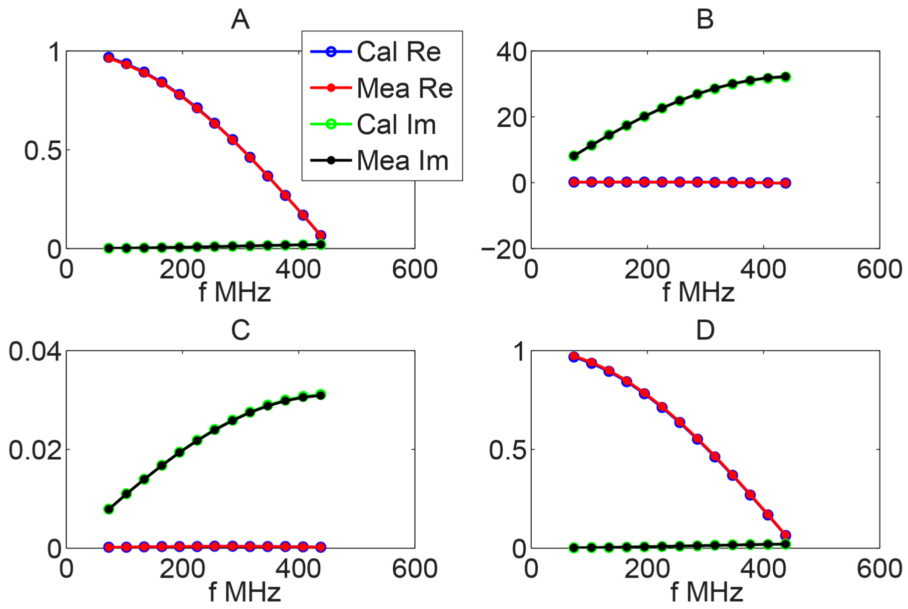

Figure 4.9: Comparison between $[ABCD]_{N_{m3-cal}}$ and $[ABCD]_{N_{m3-meas}}$.

Consider the structure depicted in Figure 4.10. A three-port network M with an impedance matrix $\mathbf{Z}_M$ has three connectors on its ports. The connectors are all identical two-port networks and have the same transmission matrices with elements A, B, C and D. With connectors on its ports, the impedance matrix $\mathbf{Z}_M$ of network M transforms into $\mathbf{Z}_{M'}$ to yield the network M'. If the $ABCD$ parameters of the connectors are known, we can derive the matrix $\mathbf{Z}_M$ from $\mathbf{Z}_{M'}$.

The derivation procedure starts with defining the voltages and currents at the ports of network M and M'. As shown in Figure 4.10, V_1, V_2 and V_3 are the voltages at the ports of M, while I_1, I_2 and I_3 are their corresponding currents. Similarly, V_4, V_5 and V_6, and I_4, I_5 and I_6 are defined at the three ports of M'. Thus, from the definition of impedance matrix [26], we can write the following two equations for $\mathbf{Z}_M$ and $\mathbf{Z}_{M'}$:

$$\begin{pmatrix} V_1 \\ V_2 \\ V_3 \end{pmatrix} = \mathbf{Z}_M \begin{pmatrix} I_1 \\ I_2 \\ I_3 \end{pmatrix} \tag{4.5.1}$$

and

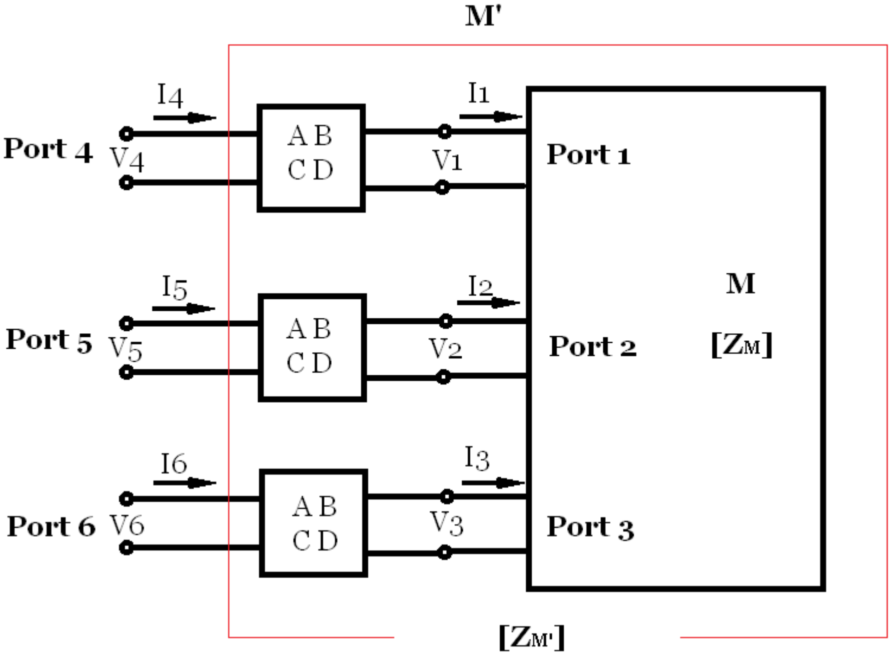

Figure 4.10: A typical three-port network with connectors on its ports.

$$\begin{pmatrix} V_4 \\ V_5 \\ V_6 \end{pmatrix} = \mathbf{Z}_{M'} \begin{pmatrix} I_4 \\ I_5 \\ I_6 \end{pmatrix} . \tag{4.5.2}$$

Since connector #1 is mounted between port 1 and port 4 (the first port of M'), then from its transmission matrix we have [26]

$$\begin{pmatrix} V_4 \\ I_4 \end{pmatrix} = \begin{pmatrix} A & B \\ C & D \end{pmatrix} \begin{pmatrix} V_1 \\ I_1 \end{pmatrix} . \tag{4.5.3}$$

For connector #2 between ports 2 and 5, and connector #3 between ports 3 and 6, we have similar expressions:

$$\begin{pmatrix} V_5 \\ I_5 \end{pmatrix} = \begin{pmatrix} A & B \\ C & D \end{pmatrix} \begin{pmatrix} V_2 \\ I_2 \end{pmatrix} , \tag{4.5.4}$$

and

$$\begin{pmatrix} V_6 \\ I_6 \end{pmatrix} = \begin{pmatrix} A & B \\ C & D \end{pmatrix} \begin{pmatrix} V_3 \\ I_3 \end{pmatrix} . \tag{4.5.5}$$

By expanding the right-hand sides of Eqns. (4.5.3) through (4.5.5), we obtain

$$V_4 = AV_1 + BI_1 \tag{4.5.6}$$

$$I_4 = CV_1 + DI_1, \tag{4.5.7}$$

$$V_5 = AV_2 + BI_2 \tag{4.5.8}$$

$$I_5 = CV_2 + DI_2 \tag{4.5.9}$$

and

$$V_6 = AV_3 + BI_3 \tag{4.5.10}$$

$$I_6 = CV_3 + DI_3. \tag{4.5.11}$$

Here we can re-organize Eqns. (4.5.6), (4.5.8) and (4.5.10) into a matrix equation for the network M' such that

$$\begin{pmatrix} V_4 \\ V_5 \\ V_6 \end{pmatrix} = A\mathbf{U} \begin{pmatrix} V_1 \\ V_2 \\ V_3 \end{pmatrix} + B\mathbf{U} \begin{pmatrix} I_1 \\ I_2 \\ I_3 \end{pmatrix}, \tag{4.5.12}$$

where

$$\mathbf{U} = \begin{bmatrix} 1 & 0 & 0 \\ 0 & 1 & 0 \\ 0 & 0 & 1 \end{bmatrix}, \tag{4.5.13}$$

which is the identity matrix. Equations (4.5.7), (4.5.9) and (4.5.11) can also be re-written into a matrix equation regarding currents at the ports of network M' as

$$\begin{pmatrix} I_4 \\ I_5 \\ I_6 \end{pmatrix} = C\mathbf{U} \begin{pmatrix} V_1 \\ V_2 \\ V_3 \end{pmatrix} + D\mathbf{U} \begin{pmatrix} I_1 \\ I_2 \\ I_3 \end{pmatrix}. \tag{4.5.14}$$

Note that Eqns. (4.5.12) and (4.5.14) define two terms in Eqn. (4.5.2). Therefore, by inserting them into Eqn. (4.5.2), we obtain

$$A\mathbf{U}\begin{pmatrix}V_1\\V_2\\V_3\end{pmatrix}+B\mathbf{U}\begin{pmatrix}I_1\\I_2\\I_3\end{pmatrix}=\mathbf{Z}_{M'}\left[C\mathbf{U}\begin{pmatrix}V_1\\V_2\\V_3\end{pmatrix}+D\mathbf{U}\begin{pmatrix}I_1\\I_2\\I_3\end{pmatrix}\right]. \tag{4.5.15}$$

After a few re-arrangements, the above equation has the form

$$\begin{pmatrix}V_1\\V_2\\V_3\end{pmatrix}=(A\mathbf{U}-\mathbf{Z}_{M'}C\mathbf{U})^{-1}(\mathbf{Z}_{M'}D\mathbf{U}-B\mathbf{U})\begin{pmatrix}I_1\\I_2\\I_3\end{pmatrix}. \tag{4.5.16}$$

A comparison between Eqns. (4.5.1) and (4.5.16) reveals that the impedance matrix $\mathbf{Z}_M$ is given by

$$\mathbf{Z}_M=(A\mathbf{U}-\mathbf{Z}_{M'}C\mathbf{U})^{-1}(\mathbf{Z}_{M'}D\mathbf{U}-B\mathbf{U}). \tag{4.5.17}$$

This is the final equation needed to derive the Z-parameter of network M from the impedance matrix of M'.

4.5.2 De-embedding a Connector from an UHF Circulator

The circulator that was designed for the UHF range operation is shown in Figure 4.11. It has a 3.5 mm connector (Part No. 311-37-00-010, SGMC Microwave) on each port.

To factor out the influence of the connector from the device's frequency response, we start with determining its response using the method discussed in Section 4.2. We fabricated two calibration devices. The connectors on their ports are the same as the ones mounted on the circulator. For the middle section of the calibration devices we use two microstrip transmission lines with different lengths (20mm and 30mm). To ensure the response of the connector transitions in the calibration kit and the circulator are identical, we set the microstrip lines to the same width, relative permittivity and substrate height as for the circulator. Figure 4.12 is a picture of these two calibration devices.

The transmission matrices of the calibration devices are measured by a network analyser. For the middle sections, we determine their ABCD matrices via simulation by

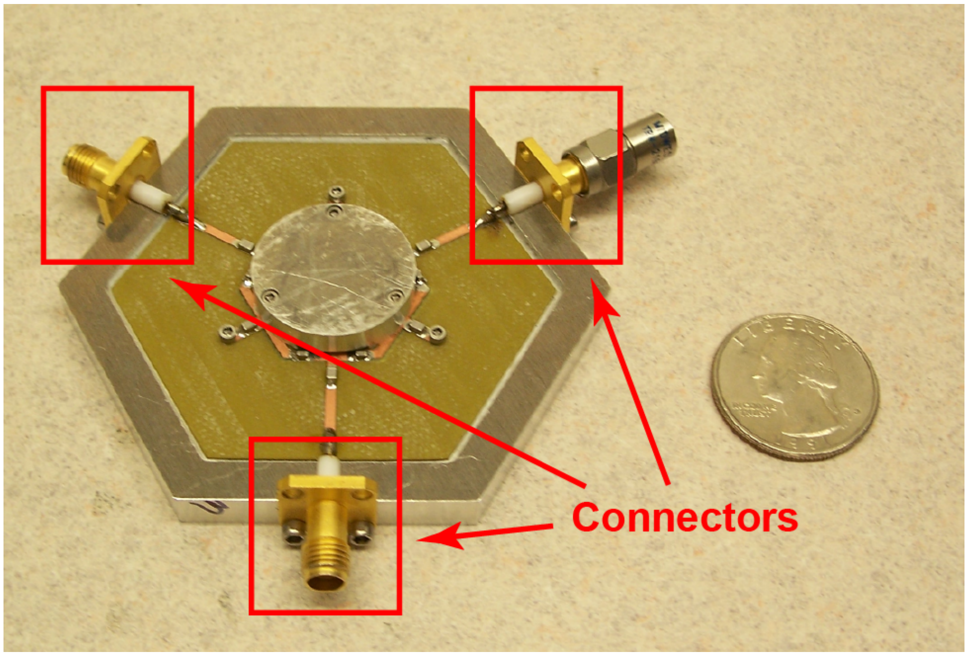

Figure 4.11: UHF circulator with connectors on its ports.

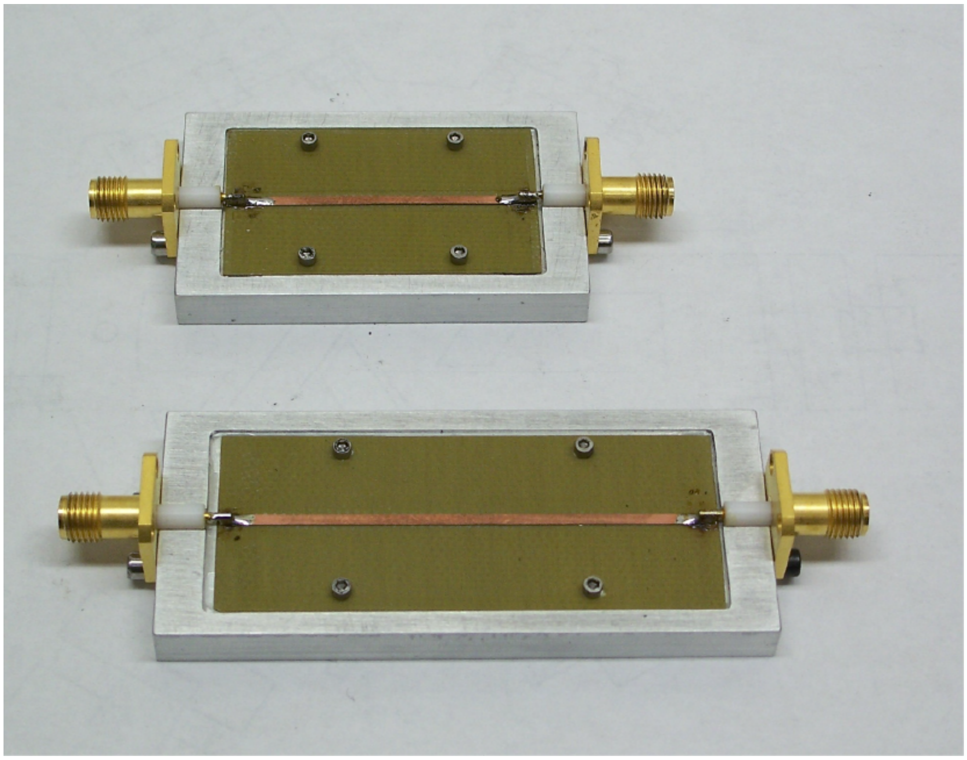

Figure 4.12: Two calibration devices for connector characterization.

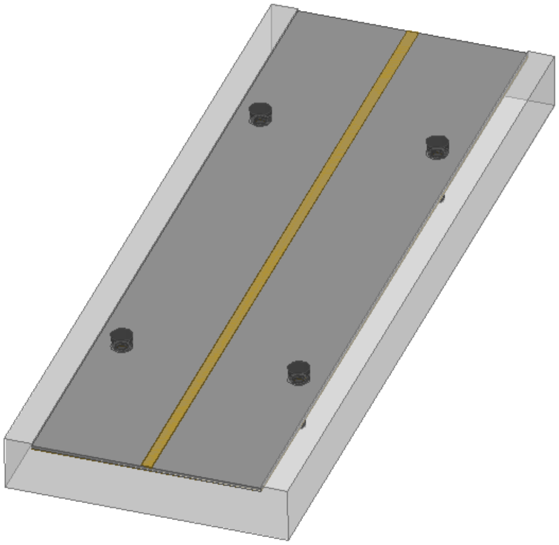

Figure 4.13: HFSS model of a transmission line used as the middle section of the calibration kit.

HFSS, since HFSS has been proven to be a precise simulation tool for dealing with simple structures like transmission lines. Figure 4.13 shows the simulation model in HFSS.

With the property of the calibration kit and their middle sections known, we calculate the response of the connector transition of the UHF circulator by using Eqns. (4.2.3) and (4.2.18) through (4.2.21). The ABCD elements of the connector for the frequency range 50 to 450 MHz are plotted in the Figure 4.14.

The next step is to use Eqn. (4.5.17) to remove the influence of the connector transition from the frequency response of the UHF circulator. The S-parameters of the device prior to the de-embedding process are measured and plotted in Figure 4.15. It does not have the high isolation performance we expect from the HFSS simulation. This is because the connector transition changes the design of the matching network. In fact, the connector can be considered as a “new” part of matching network cascading to the one that was designed. This “add-on” to the matching network introduces impedance mismatches between the network’s frequency response and the circulator impedance. Therefore the measured performance of the circulator has an offset from what was calculated.

Figure 4.16 shows the S-parameters of the UHF circulator after the connector was de-embedded, i.e., the performance of the actual circulator. From the figure we see a 30

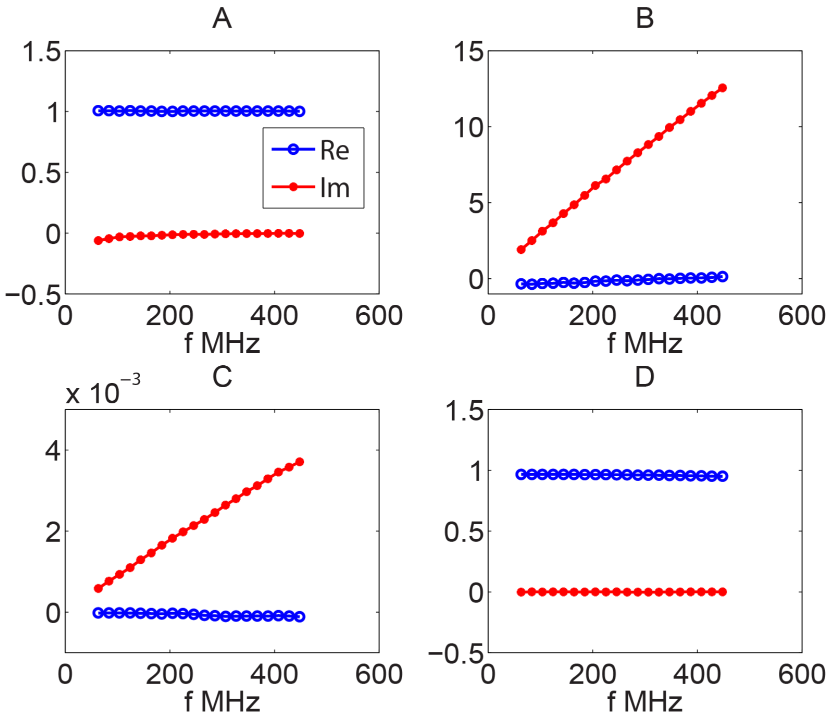

Figure 4.14: ABCD parameters of the connector for UHF circulator.

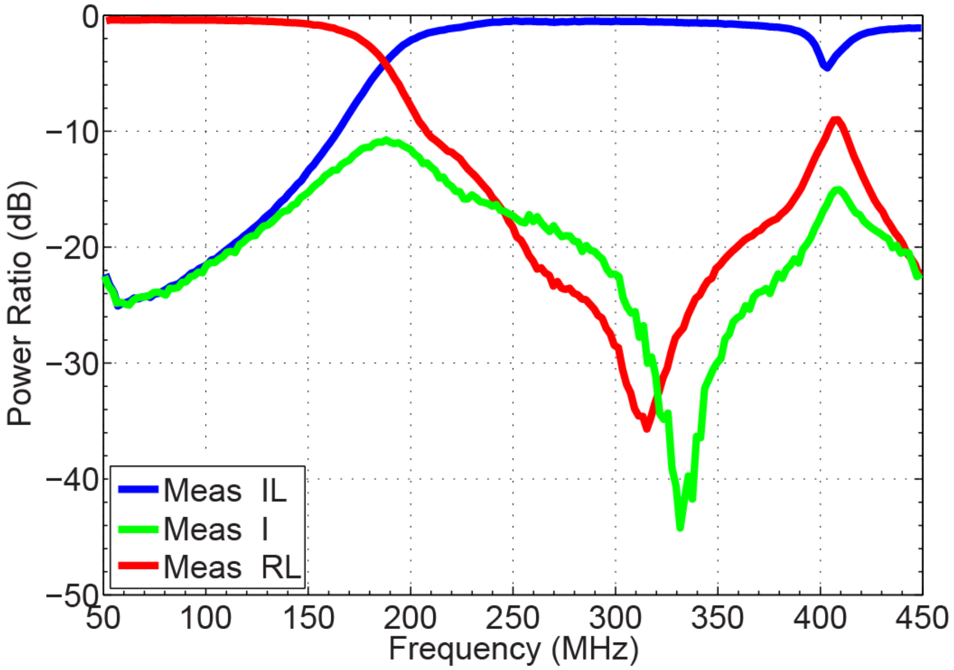

Figure 4.15: Frequency response of an UHF circulator before the influence of the connector is de-embedded.

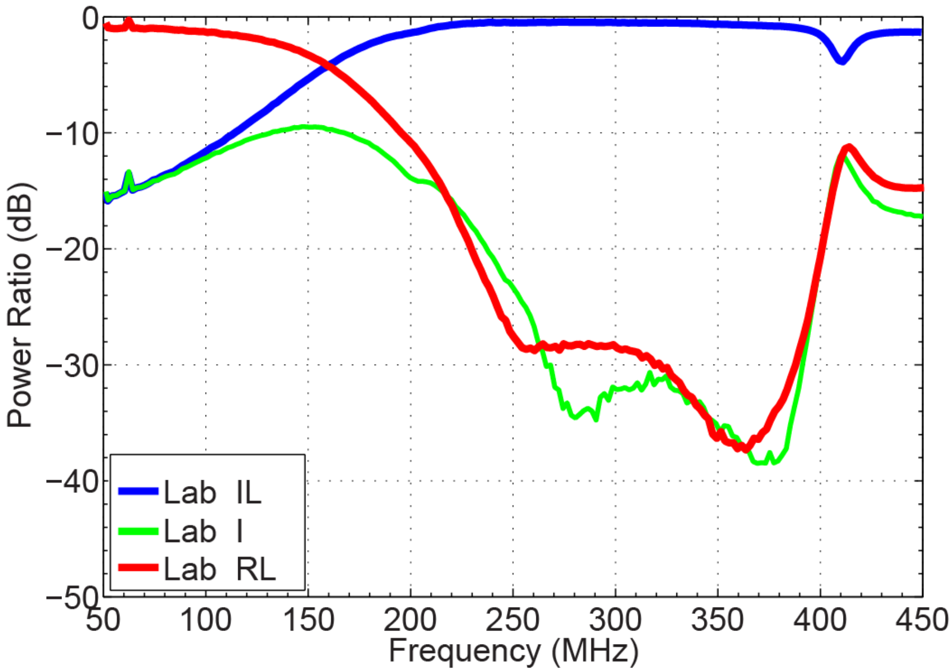

Figure 4.16: Frequency response of UHF circulator after the influence of the connector is de-embedded.

dB high isolation is obtained over 260 to 390 MHz range, which is consistent with the result predicted by HFSS simulation.

CHAPTER 5

DEMAGNETIZATION FACTOR OF A NON-ELLIPSOIDAL FERRITE SAMPLE

5.1 Introduction

When a ferrite sample is saturated by an external biasing filed $\mathbf{H}_a$, the magnetization inside the sample reduces the magnitude of the internal field $\mathbf{H}_0$, thus introducing a difference between $\mathbf{H}_0$ and $\mathbf{H}_a$, known as the demagnetizing field. Another term we use to describe this field difference is the demagnetization factor, which is a function of sample shape. Because the internal field $\mathbf{H}_0$ is an important parameter that determines the electromagnetic properties of the ferrite material, knowing the demagnetization factor of a ferrite sample will a) help us understand the operation mode of the ferrite components in the microwave circuit or system and b) provide an effective method for tuning and optimizing the performance variables that can be adjusted (e.g., $\mathbf{H}_a$, physical dimensions, etc.).

The calculation of the demagnetization factor depends exclusively on the geometrical shape of the ferrite sample. For a ferrite sample that is an ellipsoidal body, the demagnetization factor inside the ferrite is uniform, therefore the calculation is straightforward. However, for non-ellipsoidal ferrite bodies, the calculation is much more complicated. The non-uniform magnetization field makes the distribution of the demagnetization field a function of position, which makes the calculation non-trivial.

A newly developed demagnetization factor calculation method is discussed in this chapter. The method includes three steps. First, the ferrite sample is meshed into elements and each element is considered as a saturated ferrite volume, which creates a magnetic field $\mathbf{H}_i$. Second, the demagnetization-factor for a specified element is calculated by superimposing the demagnetizing field from the other elements. Third, the calculation is repeated for every single element.

The treatment that follows is divided into four parts. The theoretical analysis will be the topic of the first part. There is a brief introduction on the cubic element meshing technique, which will be used to illustrate the concept of our method. After that, the main

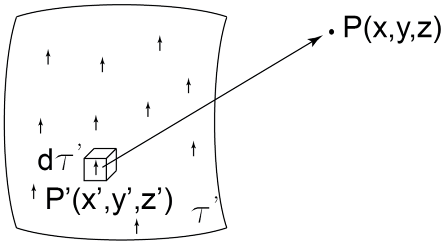

Figure 5.1: A ferrite sample.

discussion will be presented by deriving the expression of the demagnetization factor using two kinds of meshing elements: triangular prism and tetrahedra. Next, a validation will be given to compare the results from our method to well-known analytical solutions. Finally, some representative computational results will be provided.

5.2 Theoretical Analysis

Before providing the derivation, we first need to choose a system of units for the analysis. In the demagnetization factor calculation, the analysis uses CGS units, which are the standard units for the biasing field. In CGS, if a ferrite sample is uniformly saturated by a biasing field in the **m** direction (**m** is a unit vector), the magnetization of the ferrite sample is $4\pi\mathbf{M}_s = (4\pi M_s)\mathbf{m}$, which has units of Gauss.

A volume element $\mathrm{d}\tau'$ of this ferrite sample (depicted in Figure 5.1) at point $P'(x', y', z')$ can be considered as a magnetic dipole with a magnitude of $4\pi M_s$ in the direction of **m**. Then the magnetic vector potential created by it at an observation point $P(x, y, z)$ is [29]

$$\mathrm{d}\mathbf{A}_s = \frac{1}{4\pi}(4\pi\mathbf{M}_s) \times \frac{\mathbf{R}}{R^3}\mathrm{d}\tau' \tag{5.2.1}$$

where

$$\mathbf{R} = (x - x')\mathbf{a}_x + (y - y')\mathbf{a}_y + (z - z')\mathbf{a}_z \tag{5.2.2}$$

$$R = |\mathbf{R}| = \sqrt{(x - x')^2 + (y - y')^2 + (z - z')^2}. \tag{5.2.3}$$

The vector potential of the whole ferrite sample $\mathbf{A}_s$ is the integral of $\mathrm{d}\mathbf{A}_s$ over the sample volume τ'. The final form is given by [29]

$$\mathbf{A}_s = \frac{1}{4\pi}\int_{\tau'}\frac{\nabla' \times (4\pi\mathbf{M}_s)}{R}\mathrm{d}\tau' + \frac{1}{4\pi}\oint_{S'}\frac{(4\pi\mathbf{M}_s)\times\mathbf{n}'}{R}\mathrm{d}S', \tag{5.2.4}$$

where S' is the surface of volume τ' and $\mathbf{n}'$ is the outward normal of S'. Since we assume uniform magnetization within the ferrite sample, the curl of $4\pi\mathbf{M}_s$ with respect to the source position in Eqn. (5.2.4) is zero. Therefore the expression of $\mathbf{A}_s$ reduces to

$$\mathbf{A}_s = \frac{4\pi M_s}{4\pi}\oint_{S'}\frac{\mathbf{m}'\times\mathbf{n}'}{R}\mathrm{d}S'. \tag{5.2.5}$$

The demagnetization field is the difference between the internal magnetic intensity $\mathbf{H}_0$ and the external applied magnetic intensity $\mathbf{H}_a$ within the ferrite volume. Assume $\mathbf{B}_a$ is the external applied magnetic flux density. We can write the total field $\mathbf{B}_o$ that is contributed by the applied field and the ferrite sample as

$$\mathbf{B}_o = \mathbf{B}_a + \nabla \times \mathbf{A}_s. \tag{5.2.6}$$

For an observation point inside the ferrite sample, we can write the expression for the total field at that point as

$$\mathbf{B}_o = \mathbf{H}_0 + (4\pi M_s)\mathbf{m}. \tag{5.2.7}$$

By equating the previous two equations, we obtain

$$\mathbf{B}_a + \nabla \times \mathbf{A}_s = \mathbf{H}_0 + (4\pi M_s)\mathbf{m}, \tag{5.2.8}$$

which leads to

$$\mathbf{H}_0 = \mathbf{B}_a + \nabla \times \mathbf{A}_s - (4\pi M_s)\mathbf{m}. \tag{5.2.9}$$

In the CGS units system, $\mathbf{B}_a = \mathbf{H}_a$ in free space. Then from the equation above we have

$$\mathbf{H}_0 = \mathbf{H}_a + \nabla \times \mathbf{A}_s - (4\pi M_s)\mathbf{m}. \tag{5.2.10}$$

Therefore the difference between $\mathbf{H}_0$ and $\mathbf{H}_a$ can be included into a demagnetization factor $\mathbf{N}$ as

$$\mathbf{H}_0 = \mathbf{H}_a - 4\pi M_s\mathbf{N}, \tag{5.2.11}$$

where

$$\begin{aligned}\mathbf{N} &= \mathbf{m} - \frac{\nabla \times \mathbf{A}_s}{4\pi M_s} \\ &= \mathbf{m} - \frac{1}{4\pi}\left(\nabla \times \oint_S \frac{\mathbf{m}' \times \mathbf{n}'}{R}\mathrm{d}S'\right).\end{aligned} \tag{5.2.12}$$

The right-hand side of Eqn. (5.2.12) indicates that the demagnetization factor is a function of position: it depends on the magnetizations direction at the observation point (first term) as well as the source point (second term). More importantly, **N** is clearly a function of the geometry of the sample.

5.3 Discretization Using Cubic Cells

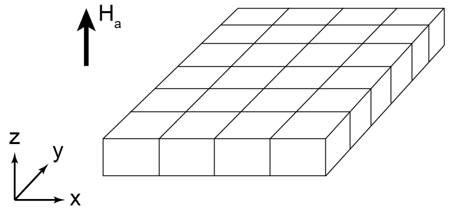

Figure 5.2: A ferrite slab meshed by cubic cells.

In most circulator design problems, researchers typically choose a rectangular slab or disk for the shape of the ferrite sample with the biasing field perpendicular to the face of the slab or disk. In this section, we evaluate the demagnetization factor of the ferrite sample of these two shapes by meshing it into small cells and applying Eqn. (5.2.12) at every cell.

Assume a ferrite rectangular slab placed on the $z = 0$ plane in the presence of an external field in the z-direction. As shown in Figure 5.2, we mesh the slab using cubic cells with an edge length of a, which makes the demagnetization factor from this slab at any observation point the superposition of the demagnetization field of each cell at that point. That is,

$$\mathbf{N}_{slab} = \sum \mathbf{N}_i \quad \text{at } P(x, y, z), \tag{5.3.1}$$

where $\mathbf{N}_i$ is the demagnetization factor created by cell i.

The selection of the edge length a must meet the requirement that a is small enough to ensure that the magnetization within the cell is uniform. Only if this condition is satisfied can every cell be considered as a single ferrite sample τ' discussed in preceding section. Therefore the demagnetization factor $\mathbf{N}_i$ for the cell can be determined via Eqn. (5.2.12). With the z-direction external field considered, $\mathbf{N}_i$ simplifies to

$$\mathbf{N}_i = \mathbf{a}_z - \frac{1}{4\pi}\left(\nabla \times \oint_{S_i} \frac{\mathbf{a}_z \times \mathbf{n}'}{R_i} \mathrm{d}S_i{}'\right). \tag{5.3.2}$$

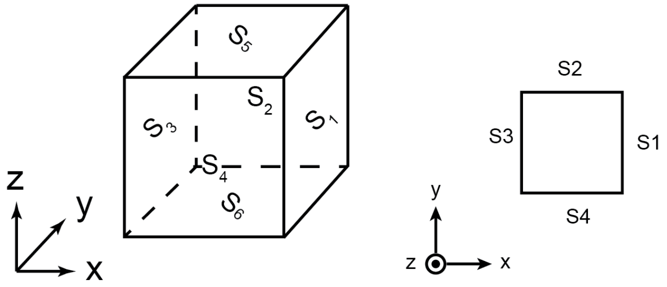

Figure 5.3: A single cubic cell. Here S_1, S_2, S_3, S_4, S_5 and S_6 are the right, back, left, front, top and bottom faces of the cell, respectively.

Let us start the calculation of Eqn. (5.3.2) for a single cell (shown in Figure 5.3), whose center is located at position $P_i'(x_i', y_i', z_i')$, by focusing on the curl-integral term, which is redefined as

$$\frac{1}{4\pi}(\nabla \times \mathbf{I}_{si}) \equiv \frac{1}{4\pi}\left(\nabla \times \oint_{S_i} \frac{\mathbf{a}_z \times \mathbf{n}'}{R_i} \mathrm{d}S_i{}'\right). \tag{5.3.3}$$

From the figure we see for a cubic cell the closed surface integral $\mathbf{I}_{si}$ is composed of four terms as follows:

$$\begin{aligned}\mathbf{I}_{si} &= \oint_{S_i} \frac{\mathbf{a}_z \times \mathbf{n}'}{R_i} \mathrm{d}S_i' \\ &= \int_{S_1} \frac{\mathbf{a}_z \times \mathbf{n}_1'}{R_i} \mathrm{d}S_1' + \int_{S_2} \frac{\mathbf{a}_z \times \mathbf{n}_2'}{R_i} \mathrm{d}S_2' + \int_{S_3} \frac{\mathbf{a}_z \times \mathbf{n}_3'}{R_i} \mathrm{d}S_3' + \int_{S_4} \frac{\mathbf{a}_z \times \mathbf{n}_4'}{R_i} \mathrm{d}S_4',\end{aligned} \tag{5.3.4}$$

where S_1, S_2, S_3 and S_4 are side-faces of the cube and $\mathbf{n}_1$, $\mathbf{n}_2$, $\mathbf{n}_3$ and $\mathbf{n}_4$ are their corresponding normals. Note: the integrals on the top and bottom faces are zero since $\mathbf{n}'$

is parallel to $\mathbf{a}_z$. Also, R_i is the distance from any point on cell's surface to the observation point. It is defined as

$$R_i = \sqrt{(x-x')^2 + (y-y')^2 + (z-z')^2}. \tag{5.3.5}$$

Therefore $\nabla \times \mathbf{I}_{si}$ can be rewritten as

$$\begin{aligned} \nabla \times \mathbf{I}_{si} = \nabla \times \int_{S_1} \frac{\mathbf{a}_z \times \mathbf{a}_x}{R_i} \mathrm{d}S_1 + \nabla \times \int_{S_2} \frac{\mathbf{a}_z \times \mathbf{a}_y}{R_i} \mathrm{d}S_2 \\ + \nabla \times \int_{S_3} \frac{\mathbf{a}_z \times (-\mathbf{a}_x)}{R_i} \mathrm{d}S_3 + \nabla \times \int_{S_4} \frac{\mathbf{a}_z \times (-\mathbf{a}_y)}{R_i} \mathrm{d}S_4. \end{aligned} \tag{5.3.6}$$

By inserting Eqns. (5.3.3) and (5.3.6) into (5.3.2), we can find the expression for the demagnetization factor at point $P(x, y, z)$ due to the magnetization from the meshing element centered at $P_i'(x_i', y_i', z_i')$. This gives,

$$\begin{aligned} \mathbf{N}_i = & \; N_{ix}\mathbf{a}_x + N_{iy}\mathbf{a}_y + N_{iz}\mathbf{a}_z \\ = & \; \mathbf{a}_x \frac{1}{4\pi}(\nabla \times \mathbf{I}_{si})_x + \mathbf{a}_y \frac{1}{4\pi}(\nabla \times \mathbf{I}_{si})_y + \mathbf{a}_z \left[1 - \frac{1}{4\pi}(\nabla \times \mathbf{I}_{si})_z\right]. \end{aligned} \tag{5.3.7}$$

Thus, the demagnetization field of the entire ferrite slab at $P(x, y, z)$ can be calculated from the superposition of $\mathbf{N}_i$ of all meshing cells within the ferrite volume. That is,

$$\begin{aligned} \mathbf{N}_{slab} = \sum \mathbf{N}_i = \mathbf{a}_x \sum N_{ix} + \mathbf{a}_y \sum N_{iy} + \mathbf{a}_z \sum N_{iz} \\ = \mathbf{a}_x \sum \frac{(\nabla \times \mathbf{I}_{si})_x}{4\pi} + \mathbf{a}_y \sum \frac{(\nabla \times \mathbf{I}_{si})_y}{4\pi} + \mathbf{a}_z \left[1 - \sum \frac{(\nabla \times \mathbf{I}_{si})_z}{4\pi}\right]. \end{aligned} \tag{5.3.8}$$

From Eqn. (5.3.4) we see that the direction of the integrand in $\mathbf{I}_{si}$ is determined by the cross product of the external applied field and the normal to the surface S_i. For two adjacent elements (as shown in Figure 5.4), the $\mathbf{I}_{si}$ on their common surface S_{com} have the same absolute value but different sign. That is, on S_{com}

$$\begin{aligned} (\mathbf{I}_{s,i})_{S_{com}} &= \int_{S_{com}} \frac{\mathbf{a}_z \times \mathbf{n}'_{S_{com}}}{R_i} \mathrm{d}S'_{com} \\ &= \int_{S_{com}} \frac{\mathbf{a}_z \times \mathbf{a}_x}{R_i} \mathrm{d}S'_{com} \end{aligned} \tag{5.3.9}$$

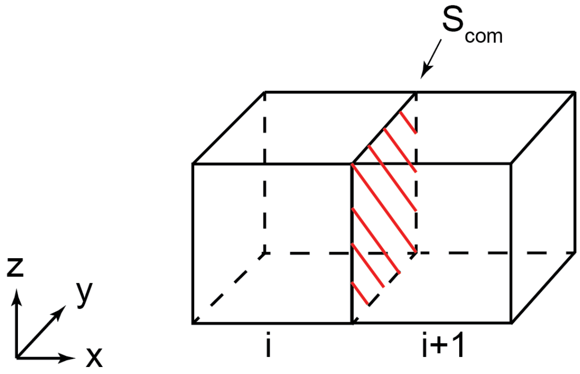

Figure 5.4: A common surface between two adjacent meshing elements.

for the ith element and

$$
\begin{aligned}
(\mathbf{I}_{s,i+1})_{S_{com}} &= \int_{S_{com}} \frac{\mathbf{a}_z \times \mathbf{n}'_{S_{com}}}{R_i} \mathrm{d}S'_{com} \\
&= \int_{S_{com}} \frac{\mathbf{a}_z \times (-\mathbf{a}_x)}{R_i} \mathrm{d}S'_{com} \qquad (5.3.10)
\end{aligned}
$$

for the $(i+1)$th element. Then from the previous two equations we conclude that

$$\mathbf{I}_{s,i} = -\mathbf{I}_{s,i+1} \quad \text{on } S_{com}. \qquad (5.3.11)$$

This means that when the summation is done in Eqn. (5.3.8), the overall integration $\mathbf{I}_s$ is zero on the surface S_{com} because it is summing $\mathbf{I}_{s,i}$ and $\mathbf{I}_{s,i+1}$. Since the demagnetization vector of a ferrite sample is calculated from the summation of the surface integration $\mathbf{I}_{si}$ for all meshing elements, the zero $\mathbf{I}_s$ on the common surface of adjacent elements makes this summation only related to integrations over the surface of the ferrite sample. This can simplify the demagnetization factor calculation by only meshing and integrating over the surface of the ferrite sample.

5.4 2D Discretization Using Triangular Prism

The cubic-cell discretization is perfect for illustrating the concept of the demagnetization factor calculation method. However, it lacks accuracy in meshing ferrite samples with a complicated geometrical shape. For example, when the ferrite sample is a disk, the meshing is not accurate on the side surface of the volume. There are two possible solutions to this problem: a) use cubic elements with smaller size or b) use other type of meshing elements that provide a better approximation. The later one is a better choice since the first increases the calculation time.

One widely used choice is the triangular element—triangle for a two-dimensional surface and tetrahedron for a three-dimensional volume. Since in this thesis we are focusing on a ferrite sample with a slab or disk shape, we will use the triangular prism, which is based upon triangular meshing as the discretization element. The meshing procedure uses the following steps. First, the top surface of the ferrite volume is meshed by triangles. Second, each triangle is then used as the top surface to form a triangular prism whose height is equal to the thickness of the ferrite slab or disk. These prisms are the meshing elements for the ferrite sample. The procedure is depicted in Figure 5.5.

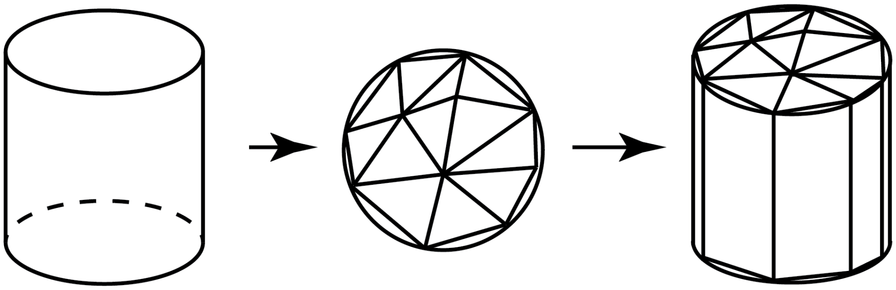

Figure 5.5: Meshing a ferrite sample using triangular prisms.

As for the meshing algorithm of the first step, researchers have put significant effort into developing algorithms that not only create high quality elements but have high efficiency. In our work, we employ the method developed by Persson [30] to mesh the top surface of the ferrite volume by triangle cells. The method uses Delaunay triangulation to generate cells and uses the force equilibrium concept to improve their quality in order to yield the best meshing for a specified domain. By taking the boundary of the computation domain as an input, the algorithm outputs the coordinates of the vertices in each triangular element.

With knowledge of the coordinates of the meshing cells' vertices, we can calculate the demagnetization factor at the observation point $P(x, y, z)$ from the superposition of its volume elements, as we have done in Section 5.3.

Similar to the example in Section 5.3, let us consider a ferrite disk with thickness h

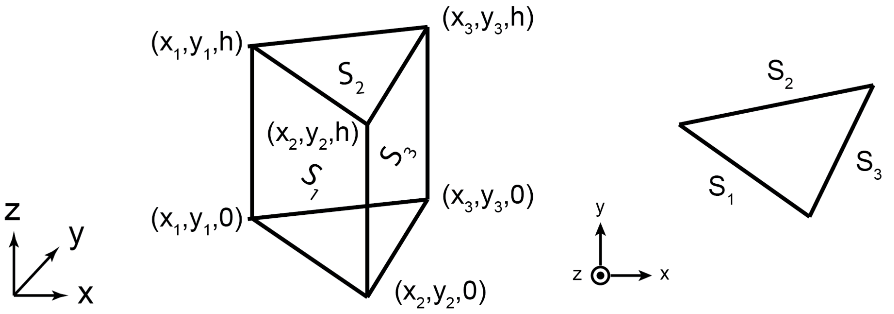

Figure 5.6: A single triangular prism cell.

resting on the $z = 0$ plane. It is saturated by a z-directed external field. From Eqn. (5.3.1), we know the demagnetization factor at observation point $P(x, y, z)$ from the disk is

$$\mathbf{N}_{disk} = \sum \mathbf{N}_{tpi} \quad \text{at } P(x,y,z), \tag{5.4.1}$$

where $\mathbf{N}_{tpi}$ is the demagnetization factor from the ith triangular prism cell. When the ith cell is a ferrite volume with uniform magnetization inside, then $\mathbf{N}_{tpi}$ is, per Eqn. (5.3.2),

$$\mathbf{N}_{tpi} = \mathbf{a}_z - \frac{1}{4\pi}\left(\nabla \times \oint_{S_{tpi}} \frac{\mathbf{a}_z \times \mathbf{n}'}{R_{tpi}} \mathrm{d}S'_{tpi}\right), \tag{5.4.2}$$

where

$$R_{tpi} = \sqrt{(x-x')^2 + (y-y')^2 + (z-z')^2}. \tag{5.4.3}$$

Figure 5.6 shows a picture of one triangular prism cell. From the picture we see that the closed surface integral in the second term of $\mathbf{N}_{tpi}$ can be split into three integrations on the side-faces of the triangular prism. That is

$$\begin{aligned} \mathbf{I}_{stpi} &= \oint_{S_{tpi}} \frac{\mathbf{a}_z \times \mathbf{n}'}{R_{tpi}} \mathrm{d}S'_{tpi} \\ &= \int_{S_1} \frac{\mathbf{a}_z \times \mathbf{n}'_1}{R_{tpi}} \mathrm{d}S'_1 + \int_{S_2} \frac{\mathbf{a}_z \times \mathbf{n}'_2}{R_{tpi}} \mathrm{d}S'_2 + \int_{S_3} \frac{\mathbf{a}_z \times \mathbf{n}'_3}{R_{tpi}} \mathrm{d}S'_3. \end{aligned} \tag{5.4.4}$$

Here S_1, S_2 and S_3 are the side surfaces. Also $\mathbf{n}_1$, $\mathbf{n}_2$ and $\mathbf{n}_3$ are the normals to each surface (shown in Figure 5.7), and they are calculated from the coordinates of the vertices of the prism cell's top (or bottom) surface, which are given by the meshing procedure.

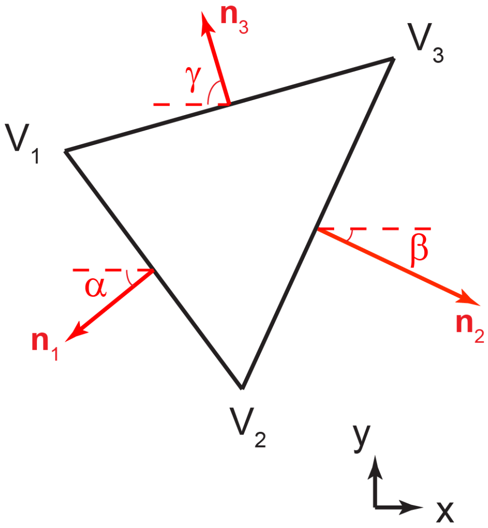

Figure 5.7: Normals to the triangular prism's side-faces.

Assume the vertices of the top surface have coordinates $\mathbf{V}_1(x_1,\ y_1,\ h)$, $\mathbf{V}_2(x_2,\ y_2,\ h)$ and $\mathbf{V}_3(x_3,\ y_3,\ h)$, where $\mathbf{V}_1$ and $\mathbf{V}_2$ are the top vertices of side-surface S_1; $\mathbf{V}_1$ and $\mathbf{V}_3$ are for S_2; $\mathbf{V}_2$ and $\mathbf{V}_3$ are for S_3. The normal $\mathbf{n}_1$ for the surface S_1, expressed by components in the x and y directions, is

$$\begin{aligned}\mathbf{n}_1 &= n_{1x}\mathbf{a}_x + n_{1y}\mathbf{a}_y\\ &= \cos\alpha\mathbf{a}_x - \sin\alpha\mathbf{a}_y,\end{aligned} \tag{5.4.5}$$

where α is the angle between $\mathbf{n}_1$ and $\mathbf{a}_x$ such that

$$\cos\alpha = \frac{y_2 - y_1}{l_1}, \tag{5.4.6}$$

$$\sin\alpha = \frac{x_2 - x_1}{l_1}, \tag{5.4.7}$$

and

$$l_1 = \sqrt{(x_2 - x_1)^2 + (y_2 - y_1)^2}, \tag{5.4.8}$$

which is the top edge length of face S_1. Similarly, the normal vectors for S_2 and S_3 are

$$\begin{aligned}\mathbf{n}_2 &= n_{2x}\mathbf{a}_x + n_{2y}\mathbf{a}_y \\ &= \cos\beta\mathbf{a}_x - \sin\beta\mathbf{a}_y \end{aligned} \tag{5.4.9}$$

with

$$\cos\beta = \frac{y_3 - y_2}{l_2}, \tag{5.4.10}$$

$$\sin\beta = \frac{x_3 - x_2}{l_2}, \tag{5.4.11}$$

$$l_2 = \sqrt{(x_3 - x_2)^2 + (y_3 - y_2)^2}. \tag{5.4.12}$$

Finally,

$$\begin{aligned}\mathbf{n}_3 &= n_{3x}\mathbf{a}_x + n_{3y}\mathbf{a}_y \\ &= \cos\gamma\mathbf{a}_x - \sin\gamma\mathbf{a}_y \end{aligned} \tag{5.4.13}$$

with

$$\cos\gamma = \frac{y_1 - y_3}{l_3}, \tag{5.4.14}$$

$$\sin\gamma = \frac{x_1 - x_3}{l_3}, \tag{5.4.15}$$

$$l_3 = \sqrt{(x_1 - x_3)^2 + (y_1 - y_3)^2}. \tag{5.4.16}$$

By inserting Eqns. (5.4.5)–(5.4.13) into Eqn. (5.4.4), we obtain the curl of $\mathbf{I}_{stpi}$ in the following form:

$$\begin{aligned}\nabla\times\mathbf{I}_{stpi} = \nabla\times &\int_{S_1} \frac{\mathbf{a}_z\times(\cos\alpha\mathbf{a}_x + \sin\alpha\mathbf{a}_y)}{R_{tpi}}\mathrm{d}S_1' \\ + \nabla\times &\int_{S_2} \frac{\mathbf{a}_z\times(\cos\beta\mathbf{a}_x + \sin\beta\mathbf{a}_y)}{R_{tpi}}\mathrm{d}S_2' \\ + \nabla\times &\int_{S_3} \frac{\mathbf{a}_z\times(\cos\gamma\mathbf{a}_x + \sin\gamma\mathbf{a}_y)}{R_{tpi}}\mathrm{d}S_3'. \end{aligned} \tag{5.4.17}$$

We next observe that $\nabla\times\mathbf{I}_{stpi}$ can be evaluated using surface integration. For clarity, we focus on the first term of the right-hand side of Eqn. (5.4.17), which is

$$\begin{aligned}
(\nabla \times \mathbf{I}_{stpi})_{S_1} &= \nabla \times \int_{S_1} \frac{\mathbf{a}_z \times (\cos\alpha \mathbf{a}_x - \sin\alpha \mathbf{a}_y)}{R_{tpi}} \mathrm{d}S_1' \\
&= \nabla \times \int_{S_1} \left[\frac{1}{R_{tpi}} (\sin\alpha \mathbf{a}_x + \cos\alpha \mathbf{a}_y) \right] \mathrm{d}S_1' \\
&= \nabla \times \left[\sin\alpha \int_{S_1} \frac{1}{R_{tpi}} \mathrm{d}S_1' \mathbf{a}_x + \cos\alpha \int_{S_1} \frac{1}{R_{tpi}} \mathrm{d}S_1' \mathbf{a}_y \right] \\
&= -\left[\cos\alpha \left(\frac{\partial}{\partial z} \int_{S_1} \frac{1}{R_{tpi}} \mathrm{d}S_1' \right) \right] \mathbf{a}_x \\
&+ \left[\sin\alpha \left(\frac{\partial}{\partial z} \int_{S_1} \frac{1}{R_{tpi}} \mathrm{d}S_1' \right) \right] \mathbf{a}_y \\
&+ \left[\cos\alpha \left(\frac{\partial}{\partial x} \int_{S_1} \frac{1}{R_{tpi}} \mathrm{d}S_1' \right) - \sin\alpha \left(\frac{\partial}{\partial y} \int_{S_1} \frac{1}{R_{tpi}} \mathrm{d}S_1' \right) \right] \mathbf{a}_z. \qquad (5.4.18)
\end{aligned}$$

As for the terms like

$$\frac{\partial}{\partial x} \int_{S_1} \frac{1}{R_{tpi}} \mathrm{d}S_1', \ \frac{\partial}{\partial y} \int_{S_1} \frac{1}{R_{tpi}} \mathrm{d}S_1' \text{ and } \frac{\partial}{\partial z} \int_{S_1} \frac{1}{R_{tpi}} \mathrm{d}S_1',$$

the integral $\int_{S_1} 1/R_{tpi} \, \mathrm{d}S_1'$ may have a singularity depending on the position of the observation point. If we evaluate the surface integral for S_1 using double integration, we obtain

$$\begin{aligned}
&\int_{S_1} \frac{1}{R_{tpi}} \mathrm{d}S_1' = \iint_{x'z'} \frac{1}{R_{tpi}} \sqrt{\left(\frac{\partial y'}{\partial x'}\right)^2 + 1 + \left(\frac{\partial y'}{\partial z'}\right)^2} \mathrm{d}z' \mathrm{d}x' \\
&= \int_{x1}^{x2} \int_0^h \left[(x-x')^2 + (y - y'(x',z'))^2 + (z-z')^2 \right]^{-\frac{1}{2}} \sqrt{\left(\frac{\partial y'}{\partial x'}\right)^2 + 1 + \left(\frac{\partial y'}{\partial z'}\right)^2} \mathrm{d}z' \mathrm{d}x'. \qquad (5.4.19)
\end{aligned}$$

From the equation above we see that when the observation point is not located on the side-surfaces of the cell, the distance $R_{tpi} = [(x-x')^2 + (y - y'(x,z))^2 + (z-z')^2]^{\frac{1}{2}}$ is not equal to zero within the integration range. Therefore the integration can be evaluated numerically. However, when the observation point $P(x,y,z)$ falls on the side-faces S_1, i.e., the coordinates of P are in the ranges of

$$
\begin{aligned}
&x \in [x_1, x_2],\\
&y \in [y_1, y_2],\\
&z \in [0, h],
\end{aligned} \tag{5.4.20}
$$

the integration is weakly singular and it can be shown that this singularity is extractable. We will discuss this in the next section as a special case.

When the observation point is not on the surface S_1, the integrand $1/R_{tpi}$ is a continuous function over the integral ranges, so the derivative with respect to the observation point can be moved within the integrand, such that

$$
\begin{aligned}
\frac{\partial}{\partial x}\int_{S_1}\frac{1}{R_{tpi}}\mathrm{d}S_1' &= \int_{S_1}\frac{\partial}{\partial x}\left(\frac{1}{R_{tpi}}\right)\mathrm{d}S_1'\\
&= \int_{S_1}\frac{\partial}{\partial x}\left[(x-x')^2+(y-y')^2+(z-z')^2\right]^{-\frac{1}{2}}\mathrm{d}S_1'\\
&= -\int_{S_1}\left[(x-x')^2+(y-y')^2+(z-z')^2\right]^{-\frac{3}{2}}(x-x')\mathrm{d}S_1'.
\end{aligned} \tag{5.4.21}
$$

To evaluate the integration on the surface S_1, we first need the equation of the plane on which S_1 resides. This can be accomplished by using its normal $\mathbf{n}_1$ given in Eqns. (5.4.5)–(5.4.8) and the coordinates of vertex $\mathbf{V}_1$. From the mathematical definition of a plane, the equation for S_1 is

$$
n_{1x}(x-x_1)+n_{1y}(y-y_1)+n_{1z}(z-z_1)=0, \tag{5.4.22}
$$

which is equal to

$$
(x-x_1)\cos\alpha-(y-y_1)\sin\alpha=0. \tag{5.4.23}
$$

Note that the term associated with the z-component has vanished. This is consistent with the fact that surface S_1 is parallel to the z direction. If we write this equation in the form $y = y(x, z)$, we have

$$
\begin{aligned}
y &= y(x,z)\\
&= y_1+\frac{\cos\alpha}{\sin\alpha}(x-x_1).
\end{aligned} \tag{5.4.24}
$$

With this equation and the definition of the surface integral, Eqn. (5.4.21) is evaluated as

$$\begin{aligned}
\frac{\partial}{\partial x}\int_{S_1}\frac{1}{R_{tpi}}\mathrm{d}S_1' = & -\int_{S_1}\left[(x-x')^2+(y-y')^2+(z-z')^2\right]^{-\frac{3}{2}}(x-x')\mathrm{d}S_1' \\
= & -\iint_{x'z'}\frac{(x-x')}{\left[(x-x')^2+(y-y'(x,z))^2+(z-z')^2\right]^{\frac{3}{2}}}\sqrt{\left(\frac{\partial y'}{\partial x'}\right)^2+1+\left(\frac{\partial y'}{\partial z'}\right)^2}\mathrm{d}z'\mathrm{d}x' \\
= & -\sqrt{\left(\frac{\cos\alpha}{\sin\alpha}\right)^2+1}\int_{x1}^{x2}\int_0^h (x-x')T_{R1}\mathrm{d}z'\mathrm{d}x', \qquad (5.4.25)
\end{aligned}$$

where

$$T_{R1} = \left[(x-x')^2+\left[y-y_1-\frac{\cos\alpha}{\sin\alpha}(x'-x_1)\right]^2+(z-z')^2\right]^{-\frac{3}{2}}. \qquad (5.4.26)$$

When the observation point is not located on the side-surfaces of the meshing element, Eqns. (5.4.25) and (5.4.26) can be calculated by numerical integration methods. If we apply similar evaluation processes to the other integrations in Eqn (5.4.18), we can obtain all of their values numerically using the following equations:

$$\frac{\partial}{\partial y}\int_{S_1}\frac{1}{R_{tpi}}\mathrm{d}S_1' = -\sqrt{\left(\frac{\cos\alpha}{\sin\alpha}\right)^2+1}\int_{x1}^{x2}\int_0^h\left[y-y_1-\frac{\cos\alpha}{\sin\alpha}(x'-x_1)\right]T_{R_1}\mathrm{d}z'\mathrm{d}x' \qquad (5.4.27)$$

$$\frac{\partial}{\partial z}\int_{S_1}\frac{1}{R_{tpi}}\mathrm{d}S_1' = -\sqrt{\left(\frac{\cos\alpha}{\sin\alpha}\right)^2+1}\int_{x1}^{x2}\int_0^h (z-z')T_{R1}\mathrm{d}z'\mathrm{d}x'. \qquad (5.4.28)$$

The computations of Eqns. (5.4.25)–(5.4.28) only need the vertices of the surface S_1 and the height of the ferrite sample h. When this is finished, the portion associated with S_1 in the term $\nabla\times\mathbf{I}_{stpi}$ is known. When the same manipulation given in Eqns. (5.4.18)–(5.4.28) is employed to the portion related to surface S_2 and S_3 in $\nabla\times\mathbf{I}_{stpi}$ (i.e., the second and third terms of the right hand side of Eqn. (5.4.17)), we are able to calculate the value of $\nabla\times\mathbf{I}_{stpi}$. The directional components of $\nabla\times\mathbf{I}_{stpi}$ are listed in following equations:

$$\begin{aligned}(\nabla\times\mathbf{I}_{stpi})_x &= \cos\alpha\sqrt{\left(\frac{\cos\alpha}{\sin\alpha}\right)^2+1}\int_{x1}^{x2}\int_0^h(z-z')T_{R1}\mathrm{d}z'\mathrm{d}x'\\ &+\cos\beta\sqrt{\left(\frac{\cos\beta}{\sin\beta}\right)^2+1}\int_{x2}^{x3}\int_0^h(z-z')T_{R2}\mathrm{d}z'\mathrm{d}x'\\ &+\cos\gamma\sqrt{\left(\frac{\cos\gamma}{\sin\gamma}\right)^2+1}\int_{x3}^{x1}\int_0^h(z-z')T_{R3}\mathrm{d}z'\mathrm{d}x',\end{aligned}\tag{5.4.29}$$

$$\begin{aligned}(\nabla\times\mathbf{I}_{stpi})_y = &-\sin\alpha\sqrt{\left(\frac{\cos\alpha}{\sin\alpha}\right)^2+1}\int_{x1}^{x2}\int_0^h(z-z')T_{R1}\mathrm{d}z'\mathrm{d}x'\\ &-\sin\beta\sqrt{\left(\frac{\cos\beta}{\sin\beta}\right)^2+1}\int_{x2}^{x3}\int_0^h(z-z')T_{R2}\mathrm{d}z'\mathrm{d}x'\\ &-\sin\gamma\sqrt{\left(\frac{\cos\gamma}{\sin\gamma}\right)^2+1}\int_{x3}^{x1}\int_0^h(z-z')T_{R3}\mathrm{d}z'\mathrm{d}x'\end{aligned}\tag{5.4.30}$$

and

$$\begin{aligned}(\nabla\times\mathbf{I}_{stpi})_z = &-\cos\alpha\sqrt{\left(\frac{\cos\alpha}{\sin\alpha}\right)^2+1}\int_{x1}^{x2}\int_0^h(x-x')T_{R1}\mathrm{d}z'\mathrm{d}x'\\ &+\sin\alpha\sqrt{\left(\frac{\cos\alpha}{\sin\alpha}\right)^2+1}\int_{x1}^{x2}\int_0^h\left[y-y_1-\frac{\cos\alpha}{\sin\alpha}(x'-x_1)\right]T_{R1}\mathrm{d}z'\mathrm{d}x'\\ &-\cos\beta\sqrt{\left(\frac{\cos\beta}{\sin\beta}\right)^2+1}\int_{x2}^{x3}\int_0^h(x-x')T_{R2}\mathrm{d}z'\mathrm{d}x'\\ &+\sin\beta\sqrt{\left(\frac{\cos\beta}{\sin\beta}\right)^2+1}\int_{x2}^{x3}\int_0^h\left[y-y_2-\frac{\cos\beta}{\sin\beta}(x'-x_2)\right]T_{R2}\mathrm{d}z'\mathrm{d}x'\\ &-\cos\gamma\sqrt{\left(\frac{\cos\gamma}{\sin\gamma}\right)^2+1}\int_{x3}^{x1}\int_0^h(x-x')T_{R3}\mathrm{d}z'\mathrm{d}x'\\ &+\sin\gamma\sqrt{\left(\frac{\cos\gamma}{\sin\gamma}\right)^2+1}\int_{x3}^{x1}\int_0^h\left[y-y_3-\frac{\cos\gamma}{\sin\gamma}(x'-x_3)\right]T_{R3}\mathrm{d}z'\mathrm{d}x',\end{aligned}\tag{5.4.31}$$

where T_{R1} is given by Eqn. (5.4.26), and T_{R2} and T_{R3} are given by

$$T_{R2}=\left[(x-x')^2+[y-y_2-\frac{\cos\beta}{\sin\beta}(x'-x_2)]^2+(z-z')^2\right]^{-\frac{3}{2}}\tag{5.4.32}$$

and

$$T_{R3} = \left[(x - x')^2 + [y - y_3 - \frac{\cos\gamma}{\sin\gamma}(x' - x_3)]^2 + (z - z')^2\right]^{-\frac{3}{2}}. \tag{5.4.33}$$

This finishes the derivation procedure for the term $\nabla \times \mathbf{I}_{stpi}$ in Eqn. (5.4.2). We are now ready to calculate the demagnetization factor from the ith triangular prism cell at observation point $P(x, y, z)$ from the cell's top surface coordinate vertices by inserting Eqns. (5.4.4), (5.4.29) through (5.4.31) into Eqn. (5.4.2). Doing so, we obtain

$$\begin{aligned}\mathbf{N}_{tpi} =& N_{tpix}\mathbf{a}_x + N_{tpiy}\mathbf{a}_y + N_{tpiz}\mathbf{a}_z \\ =& \mathbf{a}_x\frac{(\nabla \times \mathbf{I}_{stpi})_x}{4\pi} + \mathbf{a}_y\frac{(\nabla \times \mathbf{I}_{stpi})_y}{4\pi} + \mathbf{a}_z\left[1 - \frac{(\nabla \times \mathbf{I}_{stpi})_z}{4\pi}\right].\end{aligned} \tag{5.4.34}$$

The demagnetization factor induced by the ferrite sample is calculated from the superposition of the $\mathbf{N}_{tpi}$ of all meshing elements using Eqn. (5.4.1).

5.4.1 Singularity Extraction

As was mentioned in previous section, when we calculate the demagnetization factor from the ith meshing element, the integrand associated with the integral

$$\int_{S_1} \frac{1}{R_{tpi}}\mathrm{d}S_1' = \int_{S_1} [(x - x')^2 - (y - y')^2 + (z - z')^2]^{-\frac{1}{2}}\mathrm{d}S_1' \tag{5.4.35}$$

in Eqn. (5.4.18) is weakly singular when the observation point is on the element's side-surfaces. The equation above uses S_1 as example. Let this singularity be located at $P_s(x_s, y_s, z_s)$. When P_s is on the plane of surface S_1 given by Eqn. (5.4.23) and falls into the range

$$\begin{aligned}&x_s \in [x_1, x_2],\\ &y_s \in [y_1, y_2],\\ &z_s \in [0, h],\end{aligned} \tag{5.4.36}$$

the distance R between the source point and observation point may be zero, i.e.,

$$R_s = \sqrt{(x_s - x')^2 + (y_s - y')^2 + (z_s - z')^2} = 0, \tag{5.4.37}$$

which makes integration of Eqn. (5.4.35) difficult to calculate.

This singularity, however, is extractable from the calculation. By inserting the plane equation for S_1, i.e., $y = y_1 + (\cos\alpha/\sin\alpha)(x - x_1)$, into the integration of Eqn. (5.4.35), we see that

$$\begin{aligned}
\int_{S_1} \frac{1}{R_{tpi}} \mathrm{d}S_1' &= \int_{S_1} \left[(x-x')^2 + (y-y')^2 + (z-z')^2\right]^{-\frac{1}{2}} \mathrm{d}S_1' \\
&= \int_{x1}^{x2} \int_0^h \left[(x-x')^2 + (y - y'(x',z'))^2 + (z-z')^2\right]^{-\frac{1}{2}} \sqrt{\left(\frac{\partial y'}{\partial x'}\right)^2 + 1 + \left(\frac{\partial y'}{\partial z'}\right)^2} \mathrm{d}z' \mathrm{d}x' \\
&= \sqrt{\left(\frac{\cos\alpha}{\sin\alpha}\right)^2 + 1} \int_{x1}^{x2} \int_0^h \left[(x-x')^2 + \left[y - y_1 - \frac{\cos\alpha}{\sin\alpha}(x' - x_1)\right]^2 + (z-z')^2\right]^{-\frac{1}{2}} \mathrm{d}z' \mathrm{d}x' \\
&= \sqrt{\left(\frac{\cos\alpha}{\sin\alpha}\right)^2 + 1} \int_{x1}^{x2} \int_0^h \frac{\mathrm{d}z'}{\sqrt{(z-z')^2 + Q^2}} \mathrm{d}x',
\end{aligned} \tag{5.4.38}$$

where

$$Q^2 = (x-x')^2 + \left[y - y_1 - \frac{\cos\alpha}{\sin\alpha}(x' - x_1)\right]^2. \tag{5.4.39}$$

As for the integrand

$$\int_0^h \frac{\mathrm{d}z'}{\sqrt{(z-z')^2 + Q^2}},$$

we observe from Schaum # 17.9.1 [31] that,

$$\int \frac{\mathrm{d}x}{\sqrt{x_2 + \beta_2}} = \ln(x + \sqrt{x^2 + \beta^2}), \tag{5.4.40}$$

in which case

$$\begin{aligned}
\int_0^h \frac{\mathrm{d}z'}{\sqrt{(z-z')^2 + Q^2}} &= -\int_{z-h}^{z} \frac{\mathrm{d}m}{\sqrt{m^2 + Q^2}} \\
&= \ln(m + \sqrt{m^2 + Q^2})\big|_{m=z-h} - \ln(m + \sqrt{m^2 + Q^2})\big|_{m=z}.
\end{aligned} \tag{5.4.41}$$

A change of variable $m = z - z'$ in the above equation was used for simplicity. From Eqn. (5.4.41), Eqn. (5.4.38) can be written as

$$\begin{aligned}\int_{S_1} \frac{1}{R_{tpi}} \mathrm{d}S_1' &= \sqrt{\left(\frac{\cos\alpha}{\sin\alpha}\right)^2 + 1} \int_{x1}^{x2} [\ln(z - h + \sqrt{(z-h)^2 + Q^2}) - \ln(z + \sqrt{z^2 + Q^2})] \mathrm{d}x' \\ &= \sqrt{\left(\frac{\cos\alpha}{\sin\alpha}\right)^2 + 1}\, [T(x, y, z - h) - T(x, y, z)]\,, \end{aligned} \tag{5.4.42}$$

where

$$T(x, y, z) = \int_{x1}^{x2} \ln(z + \sqrt{z^2 + Q^2}) \mathrm{d}x'. \tag{5.4.43}$$

When the observation point $P(x, y, z)$ is at $P_s(x_s, y_s, z_s)$, the term Q^2 becomes

$$\begin{aligned} Q^2\big|_{at\ P_s} =& (x_s - x')^2 + \left[y_s - y_1 - \frac{\cos\alpha}{\sin\alpha}(x' - x_1)\right]^2 \\ =& (x_s - x')^2 + \left[y_1 + \frac{\cos\alpha}{\sin\alpha}(x_s - x_1) - y_1 - \frac{\cos\alpha}{\sin\alpha}(x' - x_1)\right]^2 \\ =& \left(1 + \frac{\cos\alpha}{\sin\alpha}\right)(x_s - x')^2, \end{aligned} \tag{5.4.44}$$

which makes Eqn. (5.4.42) singular under the following three cases:

Case 1: $x' = x_s$ and $0 < z_s < h$,

Case 2: $x' = x_s$ and $z_s = h$,

Case 3: $x' = x_s$ and $z_s = 0$.

Let us first consider the case $0 < z_s < h$ in which the function $T(x, y, z-h)$ is singular. In order to evaluate the integration, we break it into two parts with the singular point on the edges of the two integrals. That is,

$$\begin{aligned} T(x, y, z - h) =& \int_{x1}^{x2} \ln(z - h + \sqrt{(z-h)^2 + Q^2}) \mathrm{d}x' \\ =& \int_{x1}^{x_s} \ln(z - h + \sqrt{(z-h)^2 + Q^2}) \mathrm{d}x' \\ +& \int_{x_s}^{x2} \ln(z - h + \sqrt{(z-h)^2 + Q^2}) \mathrm{d}x', \\ =& I_{T1} + I_{T2}, \end{aligned} \tag{5.4.45}$$

where,

$$I_{T1} = \int_{x_1}^{x_s} \ln(t)\mathrm{d}x', \tag{5.4.46}$$

$$I_{T2} = \int_{x_s}^{x_2} \ln(t)\mathrm{d}x' \tag{5.4.47}$$

and

$$t = z - h + \sqrt{(z-h)^2 + Q^2}. \tag{5.4.48}$$

According to Amari *et al.* [32], both I_{T1} and I_{T2} are integrable. For I_{T1}, we can write

$$\begin{aligned} I_{T1} &= \int_{x1}^{x_s} \ln(t)\mathrm{d}x' \\ &= \int_{x1}^{x_s} \frac{\ln(t)}{\ln(x'-x_s)} \ln(x'-x_s)\mathrm{d}x'. \end{aligned} \tag{5.4.49}$$

By using integration-by-parts, we rewrite I_{T1} as

$$\begin{aligned} I_{T1} &= \int_{x1}^{x_s} \frac{\ln(t)}{\ln(x'-x_s)} \ln(x'-x_s)\mathrm{d}x' \\ &= \int_{x1}^{x_s} \frac{\mathrm{d}}{\mathrm{d}x'}\left[[(x'-x_s)\ln(x'-x_s) - (x'-x_s)]\frac{\ln(t)}{\ln(x'-x_s)}\right]\mathrm{d}x' \\ &- \int_{x1}^{x_s} [(x'-x_s)\ln(x'-x_s) - (x'-x_s)]\frac{\mathrm{d}}{\mathrm{d}x'}\left[\frac{\ln(t)}{\ln(x'-x_s)}\right]\mathrm{d}x' \\ &= \left[[(x'-x_s)\ln(x'-x_s) - (x'-x_s)]\frac{\ln(t)}{\ln(x'-x_s)}\right]\Bigg|_{x_1}^{x_s} \\ &- \int_{x1}^{x_s} [(x'-x_s)\ln(x'-x_s) - (x'-x_s)]\frac{\mathrm{d}}{\mathrm{d}x'}\left[\frac{\ln(t)}{\ln(x'-x_s)}\right]\mathrm{d}x'. \end{aligned} \tag{5.4.50}$$

The first term on the right-hand side of Eqn. (5.4.50) has a finite value when evaluated at $x' = x_1$. In the case when $x' = x_s$, it can be calculated by employing L'Hospital's rule such that

$$\begin{aligned} &\lim_{x'\to x_s}\left[[(x'-x_s)\ln(x'-x_s) - (x'-x_s)]\frac{\ln(t)}{\ln(x'-x_s)}\right] \\ &\qquad = \lim_{x'\to x_s}(x'-x_s)\ln(t) - \lim_{x'\to x_s}\frac{(x'-x_s)\ln(t)}{\ln(x'-x_s)}. \end{aligned} \tag{5.4.51}$$

As for the term $(x' - x_s)\ln(t)$, we have

$$\begin{aligned}\lim_{x'\to x_s}(x'-x_s)\ln(t) &= \lim_{x'\to x_s}\frac{\ln(t)}{(x'-x_s)^{-1}}\\ &= \lim_{x'\to x_s} -\frac{t'(x'-x_s)^2}{t}\\ &= \lim_{x'\to x_s} -\frac{t''(x'-x_s)^2}{t'} + \lim_{x'\to x_s} 2(x'-x_s).\end{aligned} \tag{5.4.52}$$

Here t' and t'' in Eqn. (5.4.52) are the first and second order derivatives of the function t defined in Eqn. (5.4.48). When $x' = x_s$, t can be expanded as

$$t = z - h + \sqrt{(z-h)^2 + Q^2} = z - h + \sqrt{(z-h)^2 + \left(1 + \frac{\cos\alpha}{\sin\alpha}\right)(x_s - x')^2}, \tag{5.4.53}$$

so that

$$\begin{aligned}t' &= \frac{\partial t}{\partial x'} = -\left(1+\frac{\cos\alpha}{\sin\alpha}\right)\left[(z-h)^2+Q^2\right]^{-\frac{1}{2}}(x'-x_s),\\ t'' &= \frac{\partial t'}{\partial x'} = -\left(1+\frac{\cos\alpha}{\sin\alpha}\right)\left[\left(1+\frac{\cos\alpha}{\sin\alpha}\right)(z-h+Q^2)^{-\frac{3}{2}}(x'-x_s)^2-(z-h+Q^2)^{-\frac{3}{2}}\right].\end{aligned} \tag{5.4.54}$$

Note that at the singular point, t' is proportional to the term $(x' - x_s)$ and t'' has a finite value of $(1 + \cos\alpha/\sin\alpha)(z - h)^{-\frac{3}{2}}$. With these properties known, we are able to determine the limit in Eqn. (5.4.52) by noting that

$$\begin{aligned}\lim_{x'\to x_s}(x'-x_s)\ln(t) &= \lim_{x'\to x_s} -\frac{t''(x'-x_s)^2}{t'} + \lim_{x'\to x_s} 2(x'-x_s)\\ &= \lim_{x'\to x_s} -\frac{t''(x'-x_s)^2}{(x'-x_s)} + 0\\ &= 0.\end{aligned} \tag{5.4.55}$$

The limit of the other term in Eqn. (5.4.51) for $x' = x_s$ can be calculate using a similar approach. Specifically,

$$\begin{aligned}\lim_{x'\to x_s}\frac{(x'-x_s)\ln(t)}{\ln(x'-x_s)} &= \lim_{x'\to x_s}\frac{\ln(t)+(x'-x_s)\frac{t'}{t}}{(x'-x_s)^{-1}}\\ &= \lim_{x'\to x_s}\ln(t)(x'-x_s)+\lim_{x'\to x_s}\frac{(x'-x_s)^2t'}{t}\\ &= 0+\lim_{x'\to x_s}2(x'-x_s)+\lim_{x'\to x_s}\frac{(x'-x_s)^2t''}{t'}\\ &= 0. \qquad (5.4.56)\end{aligned}$$

Thus, from Eqns. (5.4.51), (5.4.55) and (5.4.56), the first term of I_{T1} in Eqn. (5.4.50) can be evaluated using

$$\begin{aligned}&\left[[(x'-x_s)\ln(x'-x_s)-(x'-x_s)]\frac{\ln(t)}{\ln(x'-x_s)}\right]\Bigg|_{x_1}^{x_s}\\ &\qquad = -[(x_1-x_s)\ln(x_1-x_s)-(x_1-x_s)]\frac{\ln(t)|_{x'=x_1}}{\ln(x_1-x_s)}. \qquad (5.4.57)\end{aligned}$$

The second term of the right-hand side of Eqn. (5.4.50), namely

$$\int_{x1}^{x_s}[(x'-x_s)\ln(x'-x_s)-(x'-x_s)]\frac{\mathrm{d}}{\mathrm{d}x'}\left[\frac{\ln(t)}{\ln(x'-x_s)}\right]\mathrm{d}x',$$

is also bounded. This can be proved by calculating the limit of the integrand when the condition $x'\to x_s$ is applied. To do this, we start with the following simplification:

$$\begin{aligned}&[(x'-x_s)\ln(x'-x_s)-(x'-x_s)]\frac{\mathrm{d}}{\mathrm{d}x'}\left[\frac{\ln(t)}{\ln(x'-x_s)}\right]\\ &= [(x'-x_s)\ln(x'-x_s)-(x'-x_s)]\left[\frac{t'}{t\ln(x'-x_s)}-\frac{\ln(t)}{\ln^2(x'-x_s)(x'-x_s)}\right]\\ &= \frac{(x'-x_s)t'}{t}-\frac{\ln(t)}{\ln(x'-x_s)}-\frac{(x'-x_s)t'}{\ln(x'-x_s)t}+\frac{\ln(t)}{\ln^2(x'-x_s)}. \qquad (5.4.58)\end{aligned}$$

The limits of the terms on the bottom line of Eqn. (5.4.58) can be evaluated by using L'Hospital's rule and using expressions of t and its derivatives in Eqn. (5.4.54). These terms are:

$$\begin{aligned}
\lim_{x'\to x_s} \frac{(x'-x_s)t'}{t} &= \lim_{x'\to x_s} \frac{t' + (x'-x_s)t''}{t'} \\
&= 1, \\
\lim_{x'\to x_s} \frac{\ln(t)}{\ln(x'-x_s)} &= \lim_{x'\to x_s} \frac{(x'-x_s)t'}{t} \\
&= \lim_{x'\to x_s} \frac{t' + (x'-x_s)t''}{t'} \\
&= 1, \\
\lim_{x'\to x_s} \frac{(x'-x_s)t'}{\ln(x'-x_s)t} &= \lim_{x'\to x_s} \frac{4t''(x'-x_s)}{-t + 2(x'-x_s)t' + \ln(x'-x_s)(x'-x_s)^2 t''} \\
&= \lim_{x'\to x_s} \frac{4t''(x'-x_s)}{3(x'-x_s)t'' + 2t''(x'-x_s)\ln(x'-x_s)} \\
&= 0, \\
\lim_{x'\to x_s} \frac{\ln(t)}{\ln^2(x'-x_s)} &= \lim_{x'\to x_s} \frac{t'(x'-x_s)}{2\ln(x'-x_s)t} \\
&= \lim_{x'\to x_s} \frac{4(x'-x_s) + 2t''}{12t'' + 4t''\ln(x'-x_s)} \\
&= 0. \qquad (5.4.59)
\end{aligned}$$

Note that some of the steps in the above derivation are omitted for simplicity. If we insert the above limits back into Eqn. (5.4.58), we have

$$\lim_{x'\to x_s} [(x'-x_s)\ln(x'-x_s) - (x'-x_s)] \left[\frac{\ln(t)}{\ln(x'-x_s)}\right]' = 1 - 1 - 0 + 0 = 0. \qquad (5.4.60)$$

The previous derivation shows that the integration I_{T1} has a finite value even though the singularity is in its integral range. The expression for I_{T1}, from Eqns. (5.4.50), (5.4.57) and (5.4.60), is then

$$\begin{aligned}
I_{T1} &= \int_{x1}^{x_s} \ln(t)\mathrm{d}x' \\
&= -\left[(x_1-x_s)\ln(x_1-x_s) - (x_1-x_s)\right] \frac{\ln(t)\big|_{x'=x_1}}{\ln(x_1-x_s)} \\
&\quad - \int_{x1}^{x_s} [(x'-x_s)\ln(x'-x_s) - (x'-x_s)] \left[\frac{\ln(t)}{\ln(x'-x_s)}\right]' \mathrm{d}x'. \qquad (5.4.61)
\end{aligned}$$

The previous integral can be evaluated using standard numerical integration methods. If we apply a similar treatment to the other integral I_{T2} in Eqn. (5.4.42), namely,

$$I_{T2} = \int_{x_s}^{x_2} \ln(z-h+\sqrt{(z-h)^2+Q^2})\mathrm{d}x', \tag{5.4.62}$$

we obtain a similar integrable result:

$$\begin{aligned} I_{T2} = {} & [(x_2-x_s)\ln(x_2-x_s)-(x_2-x_s)]\frac{\ln(t)\big|_{x'=x_2}}{\ln(x_2-x_s)} \\ & - \int_{x_s}^{x_2} [(x'-x_s)\ln(x'-x_s)-(x'-x_s)]\left[\frac{\ln(t)}{\ln(x'-x_s)}\right]' \mathrm{d}x, \end{aligned} \tag{5.4.63}$$

where $t = z-h+\sqrt{(z-h)^2+Q^2}$.

Therefore, when $0 < z < h$ and from Eqns. (5.4.42), (5.4.45), (5.4.61) and (5.4.63), we have the expression of $\int_{S_1}(1/R_{tpi})\mathrm{d}S_1'$ in a form that can be numerically evaluated as

$$\left[\int_{S_1}\frac{1}{R_{tpi}}\mathrm{d}S_1'\right]\Bigg|_{0<z<h} = [I_{T1}+I_{T2}-T(x,y,z)]\sqrt{\left(\frac{\cos\alpha}{\sin\alpha}\right)^2+1}. \tag{5.4.64}$$

We now consider the situation $z_s = h$. When this is the case, the function $T(x,y,z-h)$ in Eqn. (5.4.42) becomes $T(x,y,0)$, which is equivalent to

$$\begin{aligned} T(x,y,0) &= \int_{x1}^{x2}\ln(z+\sqrt{z^2+Q^2})\mathrm{d}x'\Bigg|_{z=0} \\ &= \int_{x1}^{x2}\ln(Q)\mathrm{d}x' \\ &= \int_{x1}^{x2}\ln\left[\sqrt{1+\frac{\cos\alpha}{\sin\alpha}}(x_s-x')\right]\mathrm{d}x'. \end{aligned} \tag{5.4.65}$$

It is obvious that $x' = x_s$ defines the singular point. The integration through this singularity begins with breaking it into two parts such that

$$\begin{aligned} & \int_{x1}^{x2}\ln\left[\sqrt{1+\frac{\cos\alpha}{\sin\alpha}}(x_s-x')\right]\mathrm{d}x' \\ = {} & \int_{x1}^{x_s}\ln\left[\sqrt{1+\frac{\cos\alpha}{\sin\alpha}}(x_s-x')\right]\mathrm{d}x' + \int_{x_s}^{x2}\ln\left[\sqrt{1+\frac{\cos\alpha}{\sin\alpha}}(x_s-x')\right]\mathrm{d}x'. \end{aligned} \tag{5.4.66}$$

For the integration from x_1 to x_s, we have

$$\begin{aligned}\int_{x_1}^{x_s} \ln\left[\sqrt{1+\frac{\cos\alpha}{\sin\alpha}}(x_s-x')\right] \mathrm{d}x' &= \int_{x_1}^{x_s} \ln\left(\sqrt{1+\frac{\cos\alpha}{\sin\alpha}}\right) \mathrm{d}x' + \int_{x_1}^{x_s} \ln(x_s-x')\mathrm{d}x' \\ &= \sqrt{1+\frac{\cos\alpha}{\sin\alpha}}(x_s-x_1) + \int_{x_1}^{x_s} \ln(x_s-x')\mathrm{d}x'. \quad (5.4.67)\end{aligned}$$

The singularity in second term of the right-hand side of the above equation can be extracted through the following manipulation:

$$\begin{aligned}\int_{x_1}^{x_s} \ln(x_s-x')\mathrm{d}x' &= \int_{x_1}^{x_s} \frac{\ln(x_s-x')}{\ln(x_s-x')} \ln(x_s-x')\mathrm{d}x' \\ &= \int_{x_1}^{x_s} \frac{\mathrm{d}}{\mathrm{d}x'}\left[[(x_s-x')-(x_s-x')\ln(x_s-x')]\frac{\ln(x_s-x')}{\ln(x_s-x')}\right]\mathrm{d}x' \\ &- \int_{x_1}^{x_s} [(x_s-x')-(x_s-x')\ln(x_s-x')]\frac{\mathrm{d}}{\mathrm{d}x'}\left[\frac{\ln(x_s-x')}{\ln(x_s-x')}\right]\mathrm{d}x' \\ &= \left[[(x_s-x')-(x_s-x')\ln(x_s-x')]\frac{\ln(x_s-x')}{\ln(x_s-x')}\right]\Bigg|_{x_1}^{x_s} \\ &- \int_{x_1}^{x_s} [(x_s-x')-(x_s-x')\ln(x_s-x')] * 0 \ \mathrm{d}x' \\ &= -[(x_s-x_1)-(x_s-x_1)\ln(x_s-x_1)], \quad (5.4.68)\end{aligned}$$

by which we utilized the fact that

$$\begin{aligned}&\lim_{x'\to x_s}\left[[(x_s-x')-(x_s-x')\ln(x_s-x')]\frac{\ln(x_s-x')}{\ln(x_s-x')}\right] \\ &= \lim_{x'\to x_s}(x_s-x') - \lim_{x'\to x_s}(x_s-x')\ln(x_s-x') \\ &= 0 - \lim_{x'\to x_s}\frac{(x_s-x')^{-1}}{-(x_s-x')^{-2}} \\ &= 0. \quad (5.4.69)\end{aligned}$$

Thus, the integration from x_1 to x_s in $T(x, y, 0)$ can be calculated in closed-form such that

$$\begin{aligned}&\int_{x_1}^{x_s} \ln\left[\sqrt{1+\frac{\cos\alpha}{\sin\alpha}}(x_s-x')\right] \mathrm{d}x' \\ &= \sqrt{1+\frac{\cos\alpha}{\sin\alpha}}(x_s-x_1) - [(x_s-x_1)-(x_s-x_1)\ln(x_s-x_1)]. \quad (5.4.70)\end{aligned}$$

By applying this same treatment to the other part of the integration (i.e., from x_s to x_2) in $T(x, y, 0)$, we obtain

$$\begin{aligned}&\int_{x_s}^{x_2} \ln\left[\sqrt{1+\frac{\cos\alpha}{\sin\alpha}}(x_s - x')\right]\mathrm{d}x' \\ &= \sqrt{1+\frac{\cos\alpha}{\sin\alpha}}(x_2 - x_s) + [(x_s - x_2) - (x_s - x_2)\ln(x_s - x_2)]. \qquad (5.4.71)\end{aligned}$$

Combining Eqns. (5.4.65), (5.4.70) and (5.4.71), we obtain

$$\begin{aligned}T(x, y, 0) = &\sqrt{1+\frac{\cos\alpha}{\sin\alpha}}(x_s - x_1) + \sqrt{1+\frac{\cos\alpha}{\sin\alpha}}(x_2 - x_s) \\ &+ [(x_s - x_2) - (x_s - x_2)\ln(x_s - x_2)] \\ &- [(x_s - x_1) - (x_s - x_1)\ln(x_s - x_1)], \qquad (5.4.72)\end{aligned}$$

which can be inserted into Eqn. (5.4.42) to obtain an expression for $\int_{S_1}(1/R_{tpi})\mathrm{d}S_1'$. Therefore,

$$\left[\int_{S_1}\frac{1}{R_{tpi}}\mathrm{d}S_1'\right]\bigg|_{z=h} = [T(x, y, 0) - T(x, y, h)]\sqrt{\left(\frac{\cos\alpha}{\sin\alpha}\right)^2 + 1}. \qquad (5.4.73)$$

The last case is when $z = 0$. For this specific value of z, both $T(x, y, z - h)$ and $T(x, y, z)$ in Eqn. (5.4.42) are singular since

$$T(x, y, z - h)\big|_{z=0} = T(x, y, -h) \qquad (5.4.74)$$

$$T(x, y, z)\big|_{z=0} = T(x, y, 0). \qquad (5.4.75)$$

However, a close look at these terms reveals that they are actually combinations of Case 1 and Case 2: $T(x, z, -h)$ can be treated by the method used in evaluating $T(x, y, z - h)$ when $0 < z < h$, and $T(x, y, 0)$ is given by Eqn. (5.4.72). As a result, we can directly write the equation for $\int_{S_1}(1/R_{tpi})\mathrm{d}S_1'$ from Eqns. (5.4.42), (5.4.45) and (5.4.72) as

$$\begin{aligned}\left[\int_{S_1}\frac{1}{R_{tpi}}\mathrm{d}S_1'\right]\bigg|_{z=0} &= [T(x, y, -h) - T(x, y, 0)]\sqrt{\left(\frac{\cos\alpha}{\sin\alpha}\right)^2 + 1} \\ &= \left[I_{T1}\big|_{z=0} + I_{T2}\big|_{z=0} - T(x, y, 0)\right]\sqrt{\left(\frac{\cos\alpha}{\sin\alpha}\right)^2 + 1}, \qquad (5.4.76)\end{aligned}$$

where $I_{T1}\big|_{z=0}$ and $I_{T2}\big|_{z=0}$ are given by Eqns. (5.4.61) and (5.4.63), respectively.

In summary, the singularity in the term $\int_{S_1}(1/R)\mathrm{d}S_1'$, which comes from the observation being located on the surface of the integral, is integrable in the calculation. Depending on the value of z, the calculations by numerical methods can be implemented using Eqns. (5.4.64), (5.4.73) or (5.4.76). For the case when the observation point is on the surfaces S_2 and S_3 of the triangular prism cell, the extraction treatment is similar.

5.5 3D Discretization Using Tetrahedra

In many numerical computational methods tetrahedra are used as the element for meshing the computational domain. An example is the finite element method (FEM). In demagnetization factor problems, using tetrahedra as an element provides us with a more accurate subdivision of the volume, particularly when the ferrite sample has a complicated shape. Tetrahedra elements are also useful in calculating the demagnetization factor from an arbitrarily-directed biasing field. When using triangular prism cells, we recall the fact $\mathbf{m} \times \mathbf{n} = 0$ on the top and bottom surfaces of the element. However, this is not the case when the biasing field is in an arbitrary direction, which means we will need to add two more integrations to cover the biasing direction change. But by using tetrahedra meshing, we only need to update four factors to include this directional change into the calculation.

For the meshing algorithm, we still use the method from Persson [30] to obtain the coordinates of the four vertices in every tetrahedra element for a given ferrite volume. The calculation of the demagnetization factor $\mathbf{N}$ is based on these vertices and the direction of the biasing field.

Before the derivation of the demagnetization factor is provided, we first need to define the way the tetrahedron's vertices are numbered. After obtaining the coordinates for vertices of a single element from the meshing procedure, we use the following method to number them: a) Choose two of the four points randomly and define them as vertices $\mathbf{V}_1(x_1, y_1, z_1)$ and $\mathbf{V}_2(x_2, y_2, z_2)$. b) Number the other two points $\mathbf{V}_3(x_3, y_3, z_3)$ and $\mathbf{V}_4(x_4, y_4, z_4)$ so that the normal $\mathbf{n}_{bot}$ to the triangle on the bottom of $\triangle\mathbf{V}_2\mathbf{V}_3\mathbf{V}_4$ spans at least a 90° angle from the vector $\mathbf{n}_c$. Here $\mathbf{n}_{bot}$ is defined as

$$\mathbf{n}_{bot} = \mathbf{V}_{32} \times \mathbf{V}_{34} = (\mathbf{V}_2 - \mathbf{V}_3) \times (\mathbf{V}_4 - \mathbf{V}_3) \tag{5.5.1}$$

and $\mathbf{n}_c$ is the vector from centroid of the triangle $\triangle \mathbf{V}_2\mathbf{V}_3\mathbf{V}_4$ to $\mathbf{V}_1$, as

$$\mathbf{n}_c = \mathbf{V}_{c1} = \mathbf{V}_1 - \mathbf{V}_c, \tag{5.5.2}$$

where

$$\mathbf{V}_c = \left(\frac{x_2 + x_3 + x_4}{3}, \frac{y_2 + y_3 + y_4}{3}, \frac{z_2 + z_3 + z_4}{3} \right). \tag{5.5.3}$$

This numbering scheme is shown in Figure 5.8.

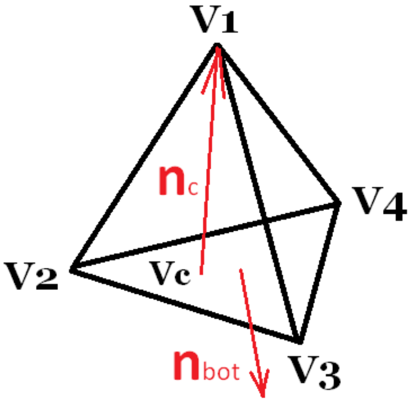

Figure 5.8: The vectors $\mathbf{n}_{bot}$ and $\mathbf{n}_c$.

5.5.1 Ferrite Sample Saturated by z-directed External Field

We begin our derivation with a simple case with the biasing field along z-direction, i.e.,

$$\mathbf{m} = \mathbf{a}_z. \tag{5.5.4}$$

A standard tetrahedra element is redrawn in Figure 5.9, and we define its surface as

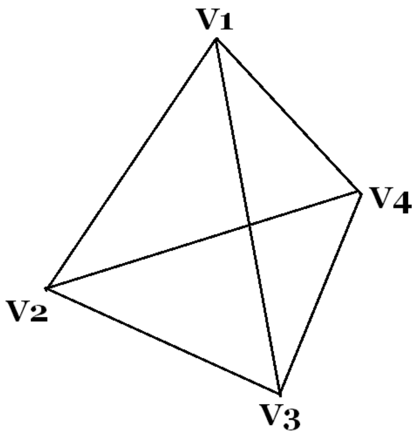

Figure 5.9: A tetrahedra meshing element.

$$
\begin{aligned}
S_{t1} &: \triangle \mathbf{V}_1\mathbf{V}_3\mathbf{V}_4, \\
S_{t2} &: \triangle \mathbf{V}_1\mathbf{V}_2\mathbf{V}_4, \\
S_{t3} &: \triangle \mathbf{V}_1\mathbf{V}_2\mathbf{V}_3, \\
S_{t4} &: \triangle \mathbf{V}_2\mathbf{V}_3\mathbf{V}_4.
\end{aligned}
\tag{5.5.5}
$$

Let us assume that the ith cell in the ferrite sample is the focus of attention and it is saturated by a z-directed biasing field. Due to the existence of this cell, the demagnetization factor $\mathbf{N}_{ti}$ at the observation $P(x,y,z)$ within the ferrite sample is

$$\mathbf{N}_{ti} = \mathbf{a}_z - \frac{1}{4\pi}\left(\nabla \times \oint_{S_i} \frac{\mathbf{a}_z \times \mathbf{n}'}{R} \mathrm{d}S_i{}'\right), \tag{5.5.6}$$

where

$$R = \sqrt{(x-x')^2 + (y-y')^2 + (z-z')^2}.$$

Of course, the total demagnetization factor from the ferrite volume at point P is the superposition of $\mathbf{N}_{ti}$ of all elements such that

$$\mathbf{N}_P = \sum \mathbf{N}_{ti} \quad \text{at } P(x,y,z). \tag{5.5.7}$$

Let us start the calculation of $\mathbf{N}_{ti}$ by defining $\mathbf{I}_{sti}$ as

$$\mathbf{I}_{sti} \equiv \oint_{S_i} \frac{\mathbf{a}_z \times \mathbf{n}'}{R} \mathrm{d}S_i{}', \tag{5.5.8}$$

which allows $\mathbf{N}_{ti}$ to be written as

$$\mathbf{N}_{ti} = \mathbf{a}_z - \frac{1}{4\pi} \left(\nabla \times \mathbf{I}_{sti} \right). \tag{5.5.9}$$

By breaking the closed-surface integral of $\mathbf{I}_{sti}$ into four integrations on the surfaces of the tetrahedra cell, we can rewrite the curl of $\mathbf{I}_{sti}$ in the form below:

$$\begin{aligned}
\nabla \times \mathbf{I}_{sti} &= \nabla \times \oint_{S_i} \frac{\mathbf{a}_z \times \mathbf{n}'}{R} \mathrm{d}S_i{}' \\
&= \nabla \times \int_{S_{t1}} \frac{\mathbf{a}_z \times \mathbf{n}'_{t1}}{R} \mathrm{d}S'_{t1} + \nabla \times \int_{S_{t2}} \frac{\mathbf{a}_z \times \mathbf{n}'_{t2}}{R} \mathrm{d}S'_{t2} \\
&\quad + \nabla \times \int_{S_{t3}} \frac{\mathbf{a}_z \times \mathbf{n}'_{t3}}{R} \mathrm{d}S'_{t3} + \nabla \times \int_{S_{t4}} \frac{\mathbf{a}_z \times \mathbf{n}'_{t4}}{R} \mathrm{d}S'_{t4}.
\end{aligned} \tag{5.5.10}$$

Let us focus on the term associated with integral on surface S_{t1}, which is triangle $\triangle \mathbf{V}_1\mathbf{V}_3\mathbf{V}_4$, since we know the manipulation of the other three terms will be similar. By using the definition of the surface integral, we rewrite this term by

$$\begin{aligned}
&\nabla \times \int_{S_{t1}} \frac{\mathbf{a}_z \times \mathbf{n}'_{t1}}{R} \mathrm{d}S'_{t1} \\
&= \nabla \times \iint_{x'y'} \frac{\mathbf{a}_z \times \mathbf{n}'_{t1}}{R} \sqrt{1 + \left(\frac{\partial z'}{\partial x'}\right)^2 + \left(\frac{\partial z'}{\partial y'}\right)^2}\, \mathrm{d}x'\mathrm{d}y' \\
&= \nabla \times \int_{x'_3}^{x'_4} \int_{y'_3}^{y'_4} \frac{\mathbf{a}_z \times \mathbf{n}'_{t1}}{R} \sqrt{1 + \left(\frac{\partial z'(x',y')}{\partial x'}\right)^2 + \left(\frac{\partial z'(x',y')}{\partial y'}\right)^2}\, \mathrm{d}x'\mathrm{d}y',
\end{aligned} \tag{5.5.11}$$

where $z' = z'(x', y')$ is the equation of the plane S_{t1} that is determined by the coordinates of $\mathbf{V}_1$, $\mathbf{V}_3$ and $\mathbf{V}_4$.

The right hand side of Eqn. (5.5.11) is integrable when the observation point $P(x, y, z)$ is not on the surface S_{t1}. However, when P falls onto S_{t1}, the integration has a singularity. To evaluate the integration, we apply two approximations so that this singularity can be extracted. First, since S_{t1} is one of the four surfaces of a meshing element, its dimension is small. Thus, we assume the distance from the source point on surface S_{t1} to the observation point is approximately equal to the distance from the centroid of S_{t1} to the observation point. That is

$$R \approx R_{t1} = \sqrt{(x - x_{tc1})^2 + (y - y_{tc1})^2 + (z - z_{tc1})^2} \tag{5.5.12}$$

and

$$x_{tc1} = \frac{x_1 + x_3 + x_4}{3}, \tag{5.5.13}$$
$$y_{tc1} = \frac{y_1 + y_3 + y_4}{3}, \tag{5.5.14}$$
$$z_{tc1} = \frac{z_1 + z_3 + z_4}{3}. \tag{5.5.15}$$

This moves the singularity of the integration to the centroid of the S_{t1}. Second, the small dimension of S_{t1} allows us to assume that the integrand $(\mathbf{a}_z \times \mathbf{n}'_{t1})/R_{t1}$ is a constant over the surface. Therefore we can simplify the calculation by using a simple product to approximate the integration. We then have

$$\nabla \times \int_{S_{t1}} \frac{\mathbf{a}_z \times \mathbf{n}'_{t1}}{R_{t1}} \mathrm{d}S'_{t1} \approx \nabla \times \left(A_{St1} \frac{\mathbf{a}_z \times \mathbf{n}'_{t1}}{R_{t1}} \right), \tag{5.5.16}$$

in which A_{St1} is the area of $\triangle \mathbf{V}_1\mathbf{V}_3\mathbf{V}_4$, and the distance R_{t1} is given by Eqn. (5.5.12).

The two approximations above are valid when the distance between the surface S_1 and the observation point is large. However, when the observation point is located at the centroid of S_1, the distance R_{t1} is zero and the integration is singular. When this is the case, we set the value of the integration $\mathbf{I}_{sti}$ to zero according to two facts: a) the ith tetrahedra element has a small dimension and can be considered as a source point and b) the demagnetization field at the source point is zero.

We can now address the evaluation procedure for Eqn. (5.5.16). The first step is to find the normal to the surface S_{t1}. This can be done by calculating the cross product of two vectors from S_{t1}. The most convenient way of doing this is to use the edges of $\triangle \mathbf{V}_1\mathbf{V}_3\mathbf{V}_4$ such that

$$\begin{aligned}
\mathbf{n}'_{t1} &= \frac{\mathbf{V}_{41} \times \mathbf{V}_{43}}{|\mathbf{V}_{41} \times \mathbf{V}_{43}|} \\
&= \frac{(\mathbf{V}_1 - \mathbf{V}_4) \times (\mathbf{V}_3 - \mathbf{V}_4)}{M_{St1}} \\
&= \frac{1}{M_{St1}} \begin{vmatrix} \mathbf{a}_x & \mathbf{a}_y & \mathbf{a}_z \\ x_1 - x_4 & y_1 - y_4 & z_1 - z_4 \\ x_3 - x_4 & y_3 - y_4 & z_3 - z_4 \end{vmatrix} \\
&= \frac{Tt_{12}}{M_{St1}}\mathbf{a}_x - \frac{Tt_{11}}{M_{St1}}\mathbf{a}_y + \frac{Tt_{13}}{M_{St1}}\mathbf{a}_z, \qquad (5.5.17)
\end{aligned}$$

where we have defined

$$M_{St1} = |\mathbf{V}_{41} \times \mathbf{V}_{43}| \qquad (5.5.18)$$

and

$$\begin{aligned}
Tt_{11} &= (x_1 - x_4)(z_3 - z_4) - (x_3 - x_4)(z_1 - z_4), \\
Tt_{12} &= (y_1 - y_4)(z_3 - z_4) - (y_3 - y_4)(z_1 - z_4), \\
Tt_{13} &= (x_1 - x_4)(y_3 - y_4) - (x_3 - x_4)(y_1 - y_4). \qquad (5.5.19)
\end{aligned}$$

Therefore the term $\mathbf{a}_z \times \mathbf{n}'_{t1}$ in Eqn. (5.5.16) now becomes

$$\begin{aligned}
\mathbf{a}_z \times \mathbf{n}'_{t1} &= \mathbf{a}_z \times \left(\frac{Tt_{12}}{M_{St1}}\mathbf{a}_x - \frac{Tt_{11}}{M_{St1}}\mathbf{a}_y + \frac{Tt_{13}}{M_{St1}}\mathbf{a}_z \right) \\
&= \frac{Tt_{11}}{M_{St1}}\mathbf{a}_x + \frac{Tt_{12}}{M_{St1}}\mathbf{a}_y. \qquad (5.5.20)
\end{aligned}$$

The other term in Eqn. (5.5.16) is the area A_{St1} of $\triangle \mathbf{V}_1\mathbf{V}_3\mathbf{V}_4$, which can be easily calculated by the property of triangles such that

$$A_{St1} = \frac{1}{2}|\mathbf{V}_{41} \times \mathbf{V}_{43}|. \qquad (5.5.21)$$

From this and Eqn. (5.5.18) we obtain

$$A_{St1} = \frac{1}{2}M_{St1}. \qquad (5.5.22)$$

Thus by inserting Eqns. (5.5.20) and (5.5.22) back into (5.5.16), we can express the term $(\nabla \times \mathbf{I}_{sti})_{S_{t1}}$ as

$$
\begin{aligned}
(\nabla \times \mathbf{I}_{sti})_{S_{t1}} &= \nabla \times \int_{S'_{t1}} \frac{\mathbf{a}_z \times \mathbf{n}'_{t1}}{R} \mathrm{d}S'_{t1} \\
&\approx \nabla \times \left(A_{St1} \frac{\mathbf{a}_z \times \mathbf{n}'_{t1}}{R_{t1}} \right) \\
&= \nabla \times \left[\frac{M_{St1}}{2} \left(\frac{Tt_{11}}{M_{St1} R_{t1}} \mathbf{a}_x + \frac{Tt_{12}}{M_{St1} R_{t1}} \mathbf{a}_y \right) \right] \\
&= \frac{1}{2} \nabla \times \left(\frac{Tt_{11}}{R_{t1}} \mathbf{a}_x + \frac{Tt_{12}}{R_{t1}} \mathbf{a}_y \right) \\
&= -\frac{1}{2} \left[Tt_{12} \frac{\partial}{\partial z} \left(\frac{1}{R_{t1}} \right) \right] \mathbf{a}_x + \frac{1}{2} \left[Tt_{11} \frac{\partial}{\partial z} \left(\frac{1}{R_{t1}} \right) \right] \mathbf{a}_y \\
&\quad + \frac{1}{2} \left[Tt_{12} \frac{\partial}{\partial x} \left(\frac{1}{R_{t1}} \right) - Tt_{11} \frac{\partial}{\partial y} \left(\frac{1}{R_{t1}} \right) \right] \mathbf{a}_z. \qquad (5.5.23)
\end{aligned}
$$

Every term in the right hand side of Eqn. (5.5.23) can be calculated from the coordinates of the tetrahedron's vertices. When the position of the observation point is inserted into the equation above, we can find the value of $(\nabla \times \mathbf{I}_{sti})_{S_{t1}}$.

As for the curl of the integrations with respect to S_{t2}, S_{t3} and S_{t4} in $\nabla \times \mathbf{I}_{sti}$, i.e., $(\nabla \times \mathbf{I}_{sti})_{S_{t2}}$, $(\nabla \times \mathbf{I}_{sti})_{S_{t3}}$ and $(\nabla \times \mathbf{I}_{sti})_{S_{t4}}$, the manipulation is similar. For the purpose of clarity, we only list the result. On triangle S_{t2}, we have

$$
\begin{aligned}
(\nabla \times \mathbf{I}_{sti})_{S_{t2}} = &-\frac{1}{2} \left[Tt_{22} \frac{\partial}{\partial z} \left(\frac{1}{R_{t2}} \right) \right] \mathbf{a}_x + \frac{1}{2} \left[Tt_{21} \frac{\partial}{\partial z} \left(\frac{1}{R_{t2}} \right) \right] \mathbf{a}_y \\
&+ \frac{1}{2} \left[Tt_{22} \frac{\partial}{\partial x} \left(\frac{1}{R_{t2}} \right) - Tt_{21} \frac{\partial}{\partial y} \left(\frac{1}{R_{t2}} \right) \right] \mathbf{a}_z, \qquad (5.5.24)
\end{aligned}
$$

where

$$
\begin{aligned}
Tt_{21} &= (x_2 - x_4)(z_1 - z_4) - (x_1 - x_4)(z_2 - z_4), \\
Tt_{22} &= (y_2 - y_4)(z_1 - z_4) - (y_1 - y_4)(z_2 - z_4), \\
Tt_{23} &= (x_2 - x_4)(y_1 - y_4) - (x_1 - x_4)(y_2 - y_4). \qquad (5.5.25)
\end{aligned}
$$

On S_{t3}, the term $(\nabla \times \mathbf{I}_{sti})_{S_{t3}}$ is

$$\begin{aligned}(\nabla\times\mathbf{I}_{sti})_{S_{t3}} = & -\frac{1}{2}\left[Tt_{32}\frac{\partial}{\partial z}\left(\frac{1}{R_{t3}}\right)\right]\mathbf{a}_x + \frac{1}{2}\left[Tt_{31}\frac{\partial}{\partial z}\left(\frac{1}{R_{t3}}\right)\right]\mathbf{a}_y \\ & + \frac{1}{2}\left[Tt_{32}\frac{\partial}{\partial x}\left(\frac{1}{R_{t3}}\right) - Tt_{31}\frac{\partial}{\partial y}\left(\frac{1}{R_{t3}}\right)\right]\mathbf{a}_z, \qquad (5.5.26)\end{aligned}$$

with

$$\begin{aligned}Tt_{31} &= (x_1-x_3)(z_2-z_3)-(x_2-x_3)(z_1-z_3), \\ Tt_{32} &= (y_1-y_3)(z_2-z_3)-(y_2-y_3)(z_1-z_3), \\ Tt_{33} &= (x_1-x_3)(y_2-y_3)-(x_2-x_3)(y_1-y_3). \qquad (5.5.27)\end{aligned}$$

Also for S_{t4},

$$\begin{aligned}(\nabla\times\mathbf{I}_{sti})_{S_{t4}} = & -\frac{1}{2}\left[Tt_{42}\frac{\partial}{\partial z}\left(\frac{1}{R_{t4}}\right)\right]\mathbf{a}_x + \frac{1}{2}\left[Tt_{41}\frac{\partial}{\partial z}\left(\frac{1}{R_{t4}}\right)\right]\mathbf{a}_y \\ & + \frac{1}{2}\left[Tt_{42}\frac{\partial}{\partial x}\left(\frac{1}{R_{t4}}\right) - Tt_{41}\frac{\partial}{\partial y}\left(\frac{1}{R_{t4}}\right)\right]\mathbf{a}_z \qquad (5.5.28)\end{aligned}$$

and

$$\begin{aligned}Tt_{41} &= (x_2-x_3)(z_4-z_3)-(x_4-x_3)(z_2-z_3), \\ Tt_{42} &= (y_2-y_3)(z_4-z_3)-(y_4-y_3)(z_2-z_3), \\ Tt_{43} &= (x_2-x_3)(y_4-y_3)-(x_4-x_3)(y_2-y_3). \qquad (5.5.29)\end{aligned}$$

Terms Tt_{23}, Tt_{33} and Tt_{43} are not used in the expression for $\mathbf{I}_{sti}$ at this point, but we still list them here because they will be useful in the calculation of the demagnetization factor from a non-z-directed biasing field, which will be discussed later.

The distances R_{t2}, R_{t3} and R_{t4} in the Eqns. (5.5.24), (5.5.26) and (5.5.28) are the distances from the observation point to the centroids of surfaces S_{t2}, S_{t3} and S_{t4}, respectively. They have a similar form as R_{t1} in Eqn. (5.5.12):

$$\begin{aligned}R_{t2} &= \sqrt{(x-x_{tc2})^2+(y-y_{tc2})^2+(z-z_{tc2})^2} \\ &= \sqrt{\left(x-\frac{x_1+x_2+x_4}{3}\right)^2+\left(y-\frac{y_1+y_2+y_4}{3}\right)^2+\left(z-\frac{z_1+z_2+z_4}{3}\right)^2}, \qquad (5.5.30)\end{aligned}$$

$$\begin{aligned} R_{t3} &= \sqrt{(x - x_{tc3})^2 + (y - y_{tc3})^2 + (z - z_{tc3})^2} \\ &= \sqrt{\left(x - \frac{x_1 + x_2 + x_3}{3}\right)^2 + \left(y - \frac{y_1 + y_2 + y_3}{3}\right)^2 + \left(z - \frac{z_1 + z_2 + z_3}{3}\right)^2} \end{aligned} \tag{5.5.31}$$

and

$$\begin{aligned} R_{t4} &= \sqrt{(x - x_{tc4})^2 + (y - y_{tc4})^2 + (z - z_{tc4})^2} \\ &= \sqrt{\left(x - \frac{x_2 + x_3 + x_4}{3}\right)^2 + \left(y - \frac{y_2 + y_3 + y_4}{3}\right)^2 + \left(z - \frac{z_2 + z_3 + z_4}{3}\right)^2}. \end{aligned} \tag{5.5.32}$$

The generalized form of the derivatives of $1/R_{ti}$ with respect to x, y, and z are expressed by

$$\begin{aligned} \frac{\partial}{\partial x}\left(\frac{1}{R_{ti}}\right) &= -[(x - x_{tci})^2 + (y - y_{tci})^2 + (z - z_{tci})^2]^{-\frac{3}{2}}(x - x_{tci}) \\ \frac{\partial}{\partial y}\left(\frac{1}{R_{ti}}\right) &= -[(x - x_{tci})^2 + (y - y_{tci})^2 + (z - z_{tci})^2]^{-\frac{3}{2}}(y - y_{tci}) \\ \frac{\partial}{\partial z}\left(\frac{1}{R_{ti}}\right) &= -[(x - x_{tci})^2 + (y - y_{tci})^2 + (z - z_{tci})^2]^{-\frac{3}{2}}(z - z_{tci}), \end{aligned} \tag{5.5.33}$$

where $(x_{tci}, y_{tci}, z_{tci})$ is the centroid of the surface of the tetrahedra cell.

With all of the above equations, we can obtain the demagnetization factor at an arbitrary point $P(x, y, z)$ by the ith tetrahedra element from Eqn. (5.5.9). The value of the term $\nabla \times \mathbf{I}_{sti}$ in the equation can be obtained from Eqns. (5.5.10), (5.5.23), (5.5.24), (5.5.26) and (5.5.28).

5.5.2 Ferrite Sample Saturated by Field in the Non-z-direction

One of the advantages of using tetrahedra as a meshing element in the demagnetization factor calculation is apparent when the biasing field is not z-oriented. In this case, we only need to update four factors in the expression of $\nabla \times \mathbf{I}_{sti}$. This update has little influence on the calculation procedure and will not lower the efficiency of the numerical computation in solving practical problems, as compared to meshing with the triangular prism element, which needs two more integrations (i.e., on the top and bottom surfaces).

Assume the biasing field has an arbitrary direction given by the vector

$$\mathbf{m} = m_x\mathbf{a}_x + m_y\mathbf{a}_y + m_z\mathbf{a}_z. \tag{5.5.34}$$

Then the expression of the demagnetization factor from the ith cell to $P(x, y, z)$ in Eqn. (5.5.6) transforms into

$$\mathbf{N}_{arb-ti} = \mathbf{m} - \frac{1}{4\pi}\left(\nabla \times \oint_{S_i} \frac{\mathbf{m} \times \mathbf{n}'}{R}\mathrm{d}{S_i}'\right), \tag{5.5.35}$$

which leads to

$$\begin{aligned}
\nabla \times \mathbf{I}_{arb-sti} &= \nabla \times \oint_{S_i} \frac{\mathbf{m} \times \mathbf{n}'}{R}\mathrm{d}{S_i}' \\
&= \nabla \times \int_{S_{t1}} \frac{\mathbf{m} \times \mathbf{n}'_{t1}}{R}\mathrm{d}S'_{t1} + \nabla \times \int_{S_{t2}} \frac{\mathbf{m} \times \mathbf{n}'_{t2}}{R}\mathrm{d}S'_{t2} \\
&+ \nabla \times \int_{S_{t3}} \frac{\mathbf{m} \times \mathbf{n}'_{t3}}{R}\mathrm{d}S'_{t3} + \nabla \times \int_{S_{t4}} \frac{\mathbf{m} \times \mathbf{n}'_{t4}}{R}\mathrm{d}S'_{t4}.
\end{aligned} \tag{5.5.36}$$

Focusing on the first term on the right-hand side of the above equation, with the help of Eqn. (5.5.20), we have

$$\begin{aligned}
\mathbf{m} \times \mathbf{n}'_{t1} &= \mathbf{m} \times \left(\frac{Tt_{12}}{M_{St1}}\mathbf{a}_x - \frac{Tt_{11}}{M_{St1}}\mathbf{a}_y + \frac{Tt_{13}}{M_{St1}}\mathbf{a}_z\right) \\
&= \frac{m_yTt_{13} + m_zTt_{11}}{M_{St1}}\mathbf{a}_x + \frac{-m_xTt_{13} + m_zTt_{12}}{M_{St1}}\mathbf{a}_y + \frac{-m_xTt_{11} - m_yTt_{12}}{M_{St1}}\mathbf{a}_z.
\end{aligned} \tag{5.5.37}$$

Note the z-component of $\mathbf{m} \times \mathbf{n}'_{t1}$ is not zero. If we define

$$\begin{aligned}
Qt_{11} &= m_yTt_{13} + m_zTt_{11}, \\
Qt_{12} &= -m_xTt_{13} + m_zTt_{12}, \\
Qt_{13} &= -m_xTt_{11} - m_yTt_{12},
\end{aligned} \tag{5.5.38}$$

the cross product of $\mathbf{m}$ and $\mathbf{n}'_{t1}$ becomes

$$\begin{aligned}(\nabla \times \mathbf{I}_{arb-sti})_{S_{t1}} = & \frac{1}{2}\left[Qt_{13}\frac{\partial}{\partial y}\left(\frac{1}{R_{t1}}\right) - Qt_{12}\frac{\partial}{\partial z}\left(\frac{1}{R_{t1}}\right)\right]\mathbf{a}_x \\ & + \frac{1}{2}\left[-Qt_{13}\frac{\partial}{\partial x}\left(\frac{1}{R_{t1}}\right) + Qt_{11}\frac{\partial}{\partial z}\left(\frac{1}{R_{t1}}\right)\right]\mathbf{a}_y \\ & + \frac{1}{2}\left[Qt_{12}\frac{\partial}{\partial x}\left(\frac{1}{R_{t1}}\right) - Qt_{11}\frac{\partial}{\partial y}\left(\frac{1}{R_{t1}}\right)\right]\mathbf{a}_z. \end{aligned} \tag{5.5.39}$$

Similarly, the terms $(\nabla \times \mathbf{I}_{sti})_{S_{t2}}$, $(\nabla \times \mathbf{I}_{sti})_{S_{t3}}$ and $(\nabla \times \mathbf{I}_{sti})_{S_{t4}}$ in Eqns. (5.5.24), (5.5.26) and (5.5.28) now become

$$\begin{aligned}(\nabla \times \mathbf{I}_{arb-sti})_{S_{t2}} = & \frac{1}{2}\left[Qt_{23}\frac{\partial}{\partial y}\left(\frac{1}{R_{t2}}\right) - Qt_{22}\frac{\partial}{\partial z}\left(\frac{1}{R_{t2}}\right)\right]\mathbf{a}_x \\ & + \frac{1}{2}\left[-Qt_{23}\frac{\partial}{\partial x}\left(\frac{1}{R_{t2}}\right) + Qt_{21}\frac{\partial}{\partial z}\left(\frac{1}{R_{t2}}\right)\right]\mathbf{a}_y \\ & + \frac{1}{2}\left[Qt_{22}\frac{\partial}{\partial x}\left(\frac{1}{R_{t2}}\right) - Qt_{21}\frac{\partial}{\partial y}\left(\frac{1}{R_{t2}}\right)\right]\mathbf{a}_z, \end{aligned} \tag{5.5.40}$$

$$\begin{aligned}(\nabla \times \mathbf{I}_{arb-sti})_{S_{t3}} = & \frac{1}{2}\left[Qt_{33}\frac{\partial}{\partial y}\left(\frac{1}{R_{t3}}\right) - Qt_{32}\frac{\partial}{\partial z}\left(\frac{1}{R_{t3}}\right)\right]\mathbf{a}_x \\ & + \frac{1}{2}\left[-Qt_{33}\frac{\partial}{\partial x}\left(\frac{1}{R_{t3}}\right) + Qt_{31}\frac{\partial}{\partial z}\left(\frac{1}{R_{t3}}\right)\right]\mathbf{a}_y \\ & + \frac{1}{2}\left[Qt_{32}\frac{\partial}{\partial x}\left(\frac{1}{R_{t3}}\right) - Qt_{31}\frac{\partial}{\partial y}\left(\frac{1}{R_{t3}}\right)\right]\mathbf{a}_z \end{aligned} \tag{5.5.41}$$

and

$$\begin{aligned}(\nabla \times \mathbf{I}_{arb-sti})_{S_{t4}} = & \frac{1}{2}\left[Qt_{43}\frac{\partial}{\partial y}\left(\frac{1}{R_{t4}}\right) - Qt_{42}\frac{\partial}{\partial z}\left(\frac{1}{R_{t4}}\right)\right]\mathbf{a}_x \\ & + \frac{1}{2}\left[-Qt_{43}\frac{\partial}{\partial x}\left(\frac{1}{R_{t4}}\right) + Qt_{41}\frac{\partial}{\partial z}\left(\frac{1}{R_{t4}}\right)\right]\mathbf{a}_y \\ & + \frac{1}{2}\left[Qt_{42}\frac{\partial}{\partial x}\left(\frac{1}{R_{t4}}\right) - Qt_{41}\frac{\partial}{\partial y}\left(\frac{1}{R_{t4}}\right)\right]\mathbf{a}_z. \end{aligned} \tag{5.5.42}$$

The general forms for the term Qt_{ij} in above equations are

$$\begin{aligned} Qt_{i1} &= m_y Tt_{i3} + m_z Tt_{i1}, \\ Qt_{i2} &= -m_x Tt_{i3} + m_z Tt_{i2}, \\ Qt_{i3} &= -m_x Tt_{i1} - m_y Tt_{i2}, \end{aligned} \tag{5.5.43}$$

where $i = 2,\ 3$ and 4 are for the surfaces S_{t2}, S_{t3} and S_{t4}, respectively.

By inserting Eqns. (5.5.39), (5.5.40)–(5.5.42) into Eqn. (5.5.35), we finish the derivation of the demagnetization factor expression at the observation point P from the tetrahedra cell number i when it is saturated by an arbitrarily directed external magnetic field. The total demagnetization factor $\mathbf{N}$ can be computed by superposing $\mathbf{N}_{arb-ti}$ of each subdivision element in the ferrite sample to yield

$$\mathbf{N}_{arb-P} = \sum \mathbf{N}_{arb-ti} \quad \text{at } P(x, y, z). \tag{5.5.44}$$

5.6 Validation

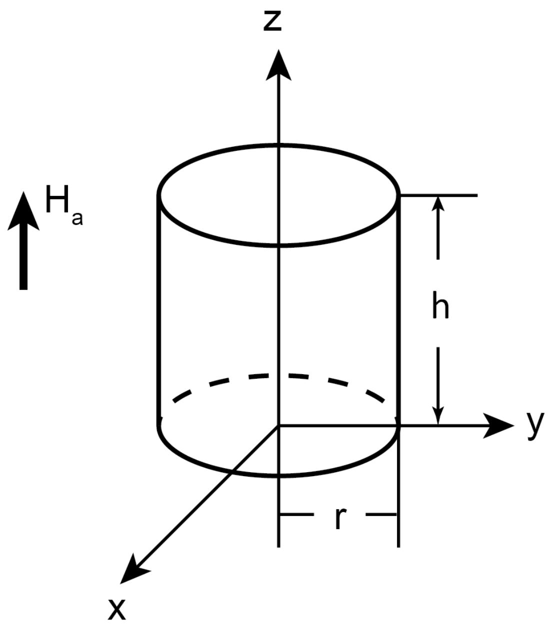

Figure 5.10: A ferrite cylinder with radius r and height h in a Cartesian coordinate system.

To validate the correctness and accuracy of our method, we calculate the demagnetization factor of cylinders with different radius-to-height ratios (i.e., r/h) and compare the results against the analytical solution given by Joseph and Schlomann [9]. As depicted in Figure 5.10, a ferrite cylinder with a uniform magnetization saturation of $4\pi M_s$ is placed in the Cartesian coordinate system the following way: the central axis of the cylinder is parallel to z axis; one of the endfaces is set on $z = 0$ plane and centered at the origin. The cylinder is saturated by an external field in the z-direction such that $\mathbf{H}_a = H_a\mathbf{a}_z$. Two comparisons are provided to ensure the validity of our method.

For the first comparison, we calculate the demagnetization factors in z-direction (i.e., N_z) along the radius of the endface from $(0, 0, 0)$ to $(0, r, 0)$ in steps of $0.02r$. We calculate N_z for three different height-to-radius ratios: $h/r = 0.2$, $h/r = 1$ and $h/r = 4$. In Figures 5.11 and 5.12, we show the comparison, using the triangular prism and the tetrahedra as meshing elements, respectively, between the results calculated by our method and the analytical solutions. We see good correlation.

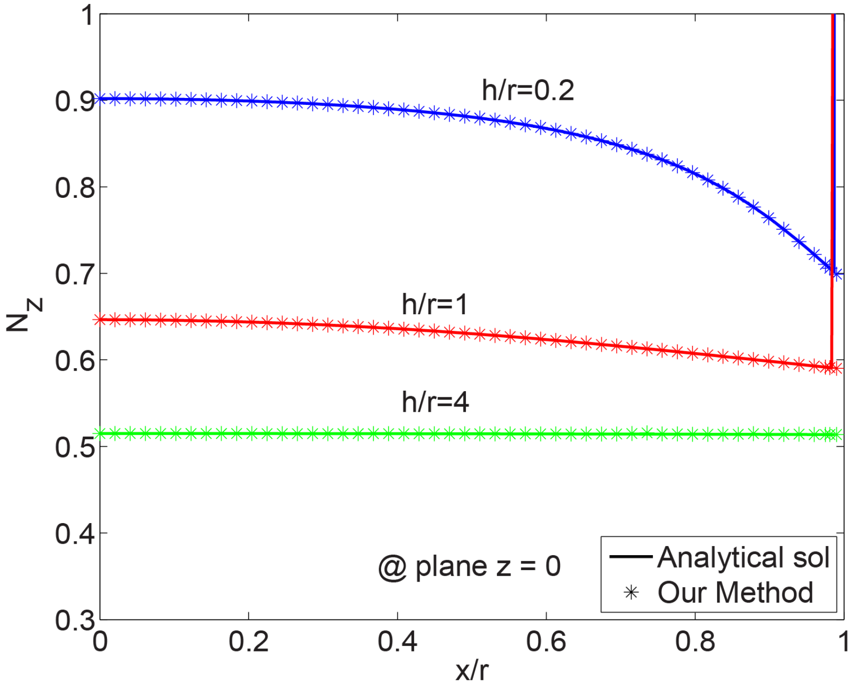

Figure 5.11: Comparison of N_z along the diameter of a cylinder on the $z = 0$ endface for different h/r ratios (triangular prism meshing element is used).

In the second case, we set up the ferrite cylinder in the same way as in first example but move the observation point to the mid-plane of the cylinder. The observation points are still along the radius from $(0, 0, h/2)$ to $(0, r, h/2)$. As we did in the first case, we changed the ratio h/r from $h/r = 0.2$ to $h/r = 1$, and then to $h/r = 5$. The demagnetization factor was calculated and plotted in Figures 5.13 and 5.14. The good agreement in both comparisons demonstrates the validity of our numerical method.

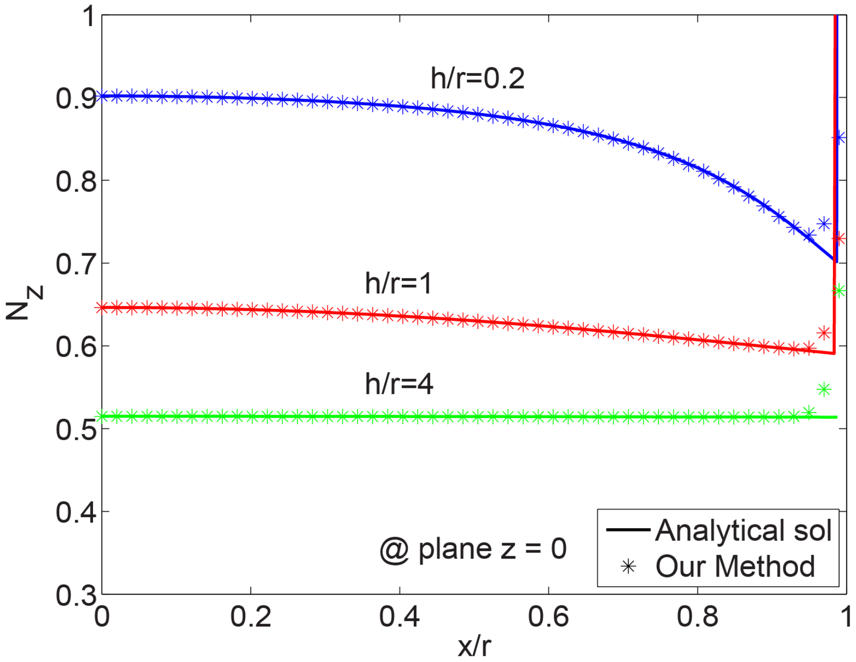

Figure 5.12: Comparison of N_z along the diameter of a cylinder on the $z = 0$ endface for different h/r ratios (tetrahedra meshing element is used).

5.7 Application

5.7.1 Demagnetization Factor for Ferrite Disk

In this example we apply our method to the ferrite disk used in the UHF circulator design. The disk sits with the endface on $z = 0$ plane, as shown in Figure 5.10. The radius of the ferrite is $r = 8.93$ mm and the height is $h = 0.58$ mm. Since this sample has a disk shape, we use the triangular prism as the meshing element and set the cell size to $0.02r$. The biasing field is in the positive z-direction, thus making the disk uniformly saturated in the same direction. The demagnetization factor N_z on the plane $z = 0$ is shown in Figure 5.15. Figure 5.16 shows N_z along the diameter of the plane from $(-9, 0, 0)$ to $(9, 0, 0)$. From this figure we see that under an uniform external biasing field, the demagnetization field is stronger towards the edge of the disk. This means when using a ferrite disk as component in a system, the designer needs to make sure the saturation at the edge of the disk is strong enough, otherwise the weaker internal field at the edge may introduce unwanted loss to the system.

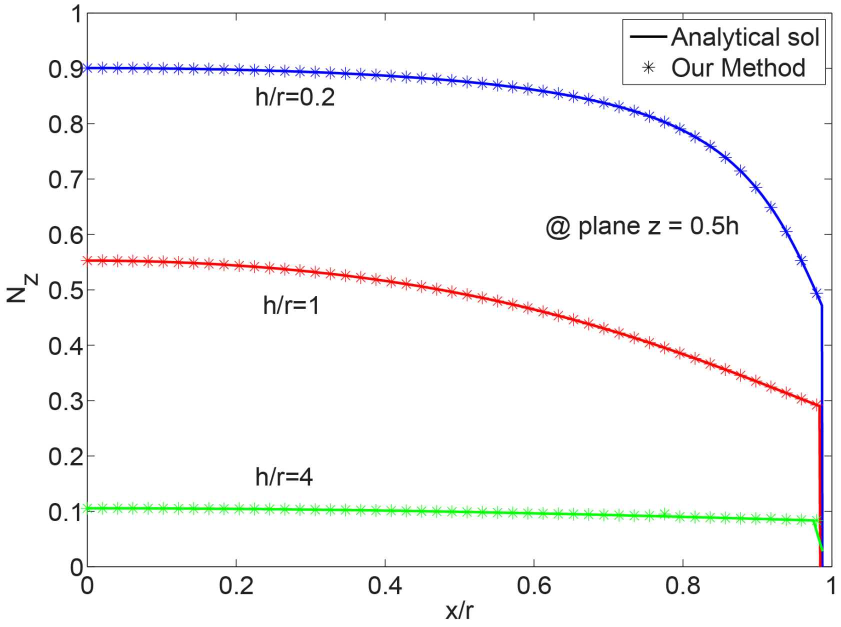

Figure 5.13: Comparison of N_z along the diameter of a cylinder on the $z = h$ mid-plane for different h/r ratios (triangular prism meshing element is used).

5.7.2 Demagnetization Factor for a Ferrite Slab with Irregular Shape

Most microwave ferrite devices use ferrite components with a circular or rectangular shape. It is not uncommon, however, to use different shapes, such as a hexagon. In this example, we apply our method to a ferrite slab that has irregular shape defined by its vertices. The top view of the slab is shown in Figure 5.17.

For the height of the slab, we set it to the value of 2 mm which is approximately 1/10 of the maximum value in x-direction, in order to use the triangular prism as elements in the meshing procedure. Its demagnetization factor on $z = 2$ mm plane associated with z-direction biasing field is calculated by our method and is shown in Figure 5.18.

5.7.3 The Demagnetization Factor of Ferrite Sample Saturated by a Biasing Field with Arbitrary Direction.

For the last example, we calculate the demagnetization factor for a ferrite disk under a non-z oriented biasing field; see the equations given in Section 5.5.2. As for the physical dimension, the disk is the same as for the design from our UHF circulator with r =8.92

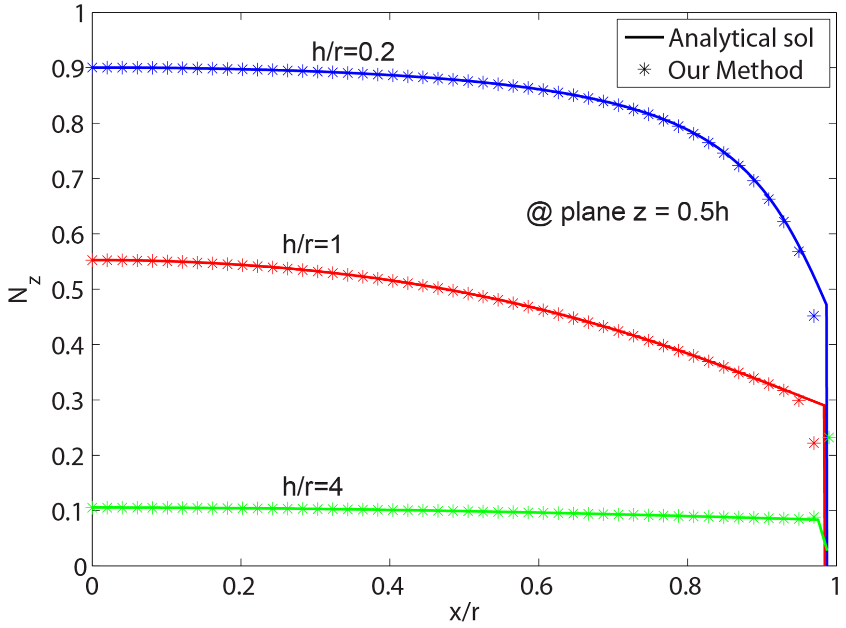

Figure 5.14: Comparison of N_z along the diameter of a cylinder on the $z = h$ mid-plane for different h/r ratios (tetrahedra meshing element is used).

mm and h =0.58 mm. It is set on the $z = 0$ plane with the center of the endface at the origin. We set the directional vector $\mathbf{m}$ as

$$\begin{aligned} \mathbf{m} &= m_x\mathbf{a}_x + m_y\mathbf{a}_y + m_z\mathbf{a}_z \\ &= 0.29\mathbf{a}_x + 0.55\mathbf{a}_y + 0.78\mathbf{a}_z, \end{aligned} \tag{5.7.1}$$

where the values of m_x, m_y and m_z are randomly picked. Figures (5.19)–(5.21) show the directional components of demagnetizing factor on the top surface ($z = h$) of the ferrite disk. From the plots we can see that in this situation, both N_x and N_y are non-zero, as opposite to z-directed case, which means if we excite electromagnetic wave along the top face of the disk (e.g., using cross-over traces as in circulator), the wave will be propagating in mixed mode of Farady rotation and birefringence.

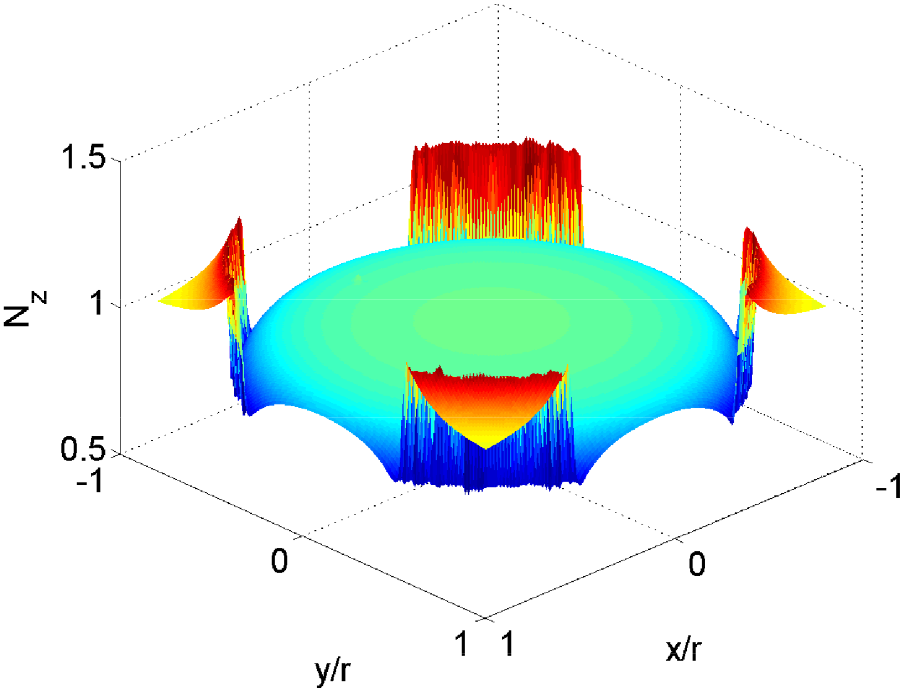

Figure 5.15: N_z on the $z = 0$ plane with $r = 8.92$ mm and $h = 0.58$ mm.

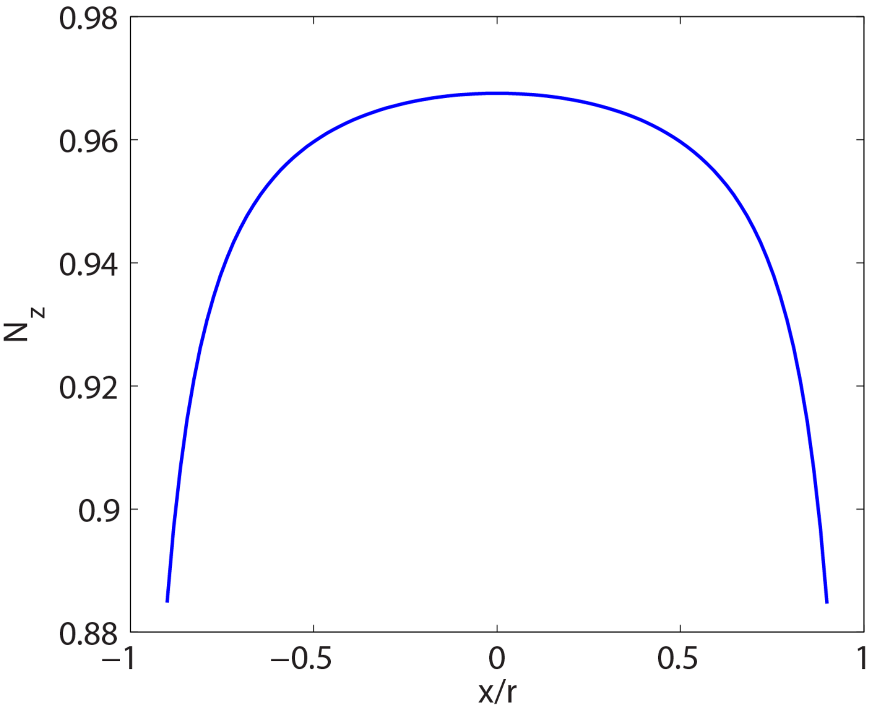

Figure 5.16: N_z along the diameter $((-r,0,0)$ to $(r,0,0))$ on the $z = 0$ plane with $r = 8.93$ mm and $h = 0.58$ mm.

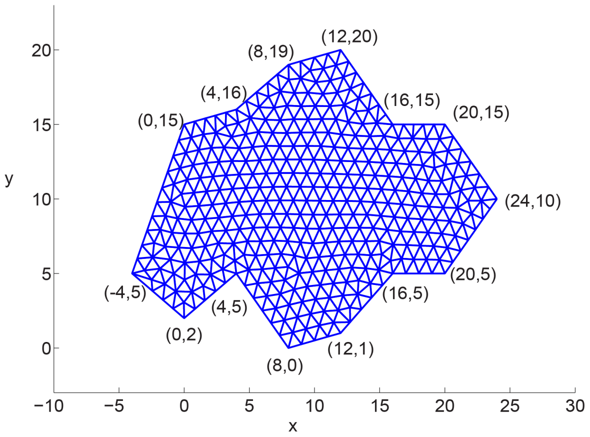

Figure 5.17: Top view of the ferrite slab with irregular shape (all units are in millimetres).

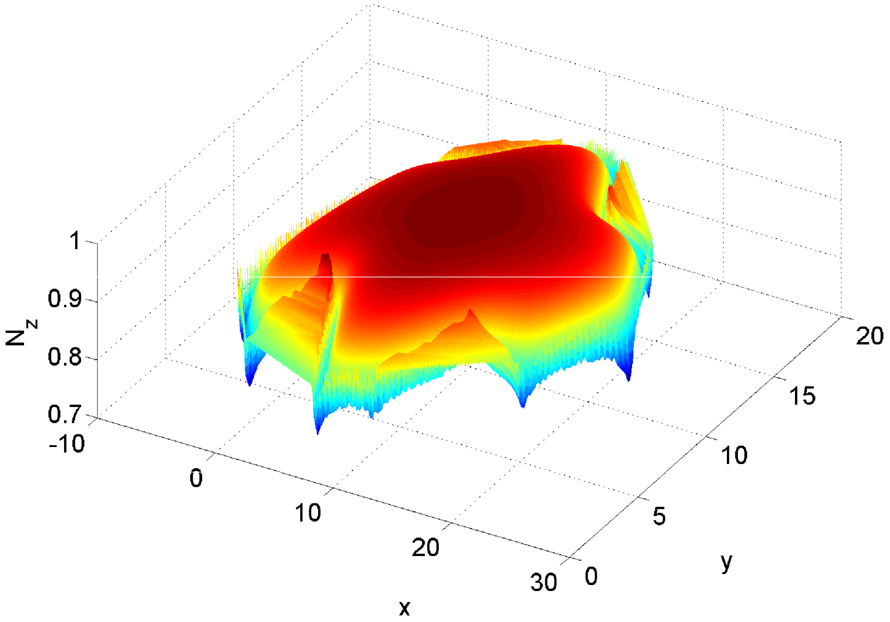

Figure 5.18: The z-component of the demagnetization factor on the top surface for a ferrite slab with irregular shape.

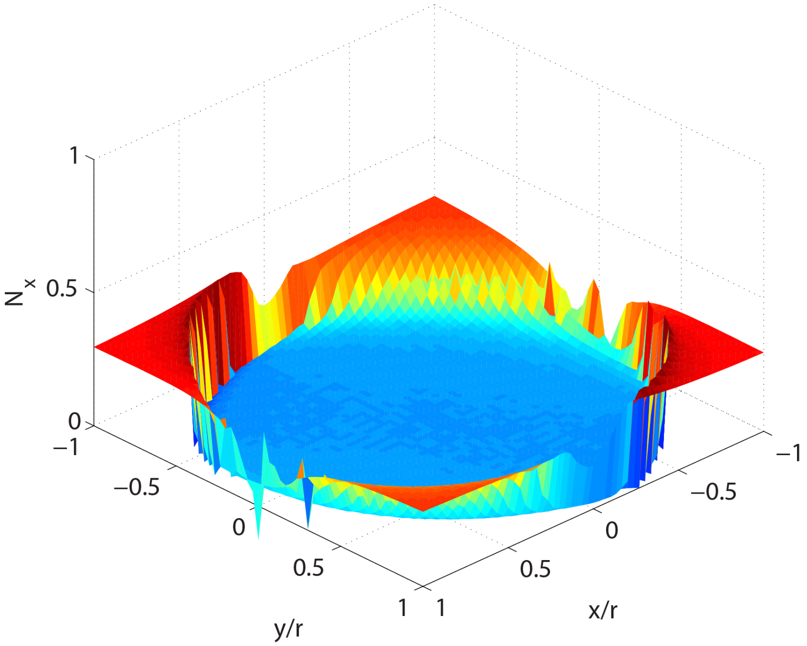

Figure 5.19: The x-component of the demagnetization factor for a ferrite disk saturated by a non-z-directed external field.

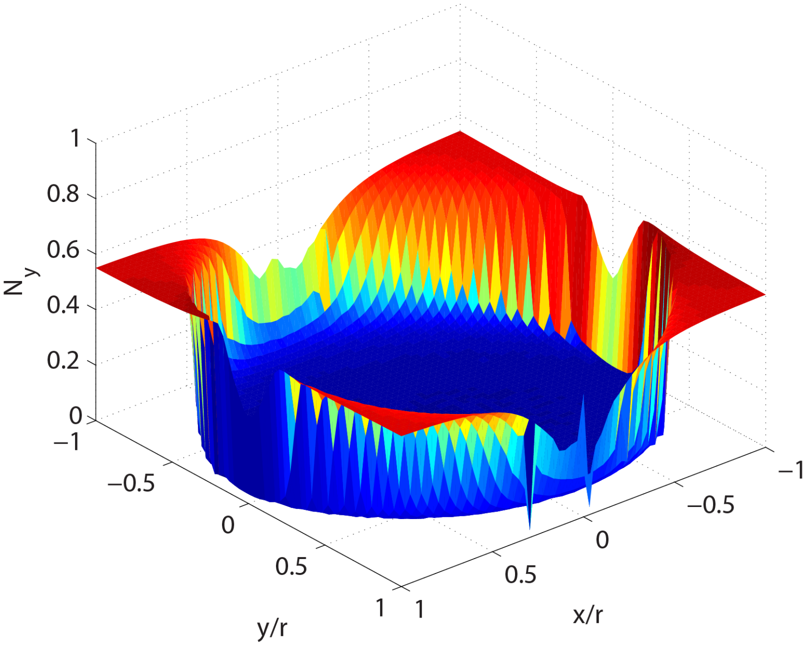

Figure 5.20: The y-component of demagnetization factor for a ferrite disk saturated by a non-z-directed external field.

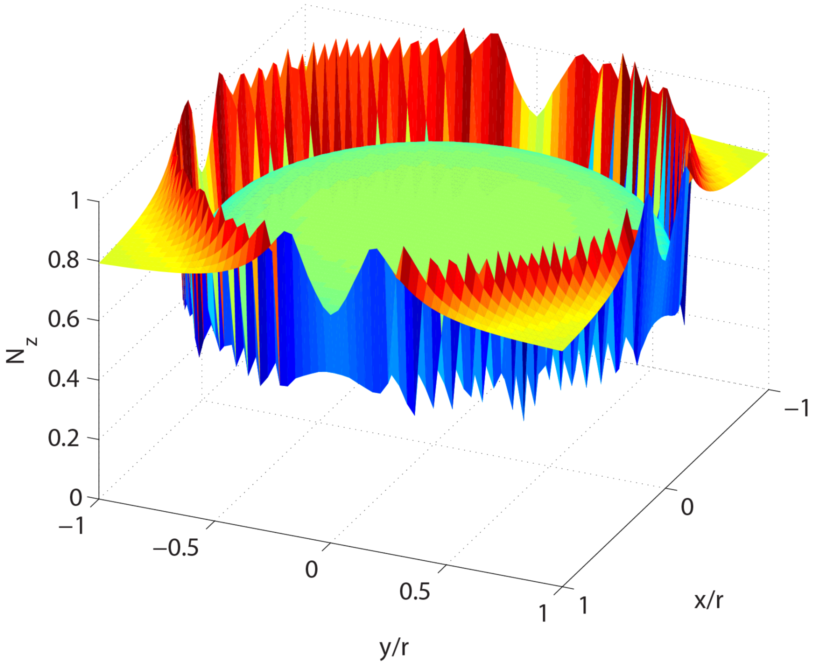

Figure 5.21: The z-component of demagnetization factor for a ferrite disk saturated by a non-z-directed external field.

CHAPTER 6

CONCLUSION

In this dissertation we discussed four topics that are related to lumped-element, crossover ferrite circulators. The first topic dealt with the upper limit for the operating bandwidth of a lumped-element, crossover ferrite circulator. Starting with the ideal network model, we developed an optimization procedure that maximizes the bandwidth of a ferrite circulator operating above-FMR. By utilizing this procedure, we found that a 194% bandwidth is theoretically obtainable by optimizing both the crossover structure and the matching network of a circulator device. Since the 194% bandwidth is obtained from a idealized model, it is believed to be the upper bound for the operating bandwidth of any above-FMR, lumped-element, ferrite circulator. The development of the optimization procedure uses frequency-normalization techniques. Therefore, we can fully generalize the optimizing method for above-FMR circulators in different frequency range applications. Moreover, when we applied this same optimizing method on hardware circulator devices, with the aid of simulation tools, we achieved bandwidths on the order of 130% from a laboratory-fabricated circulator.

The second topic in this dissertation considered a novel spiral trace topology for the lumped-element, ferrite circulator. Using this topology, we designed a UHF circulator and achieved a deep isolation (around 30 dB), wide-band (245-355 MHz) performance. By using a precise simulation tool, we compared the performance between the new trace topology and traditional trace geometry, and showed how the isolation and bandwidth was improved by the new center trace. From a fabricated circulator, a 30 dB isolation over 260-390 MHz bandwidth was measured. The good correlation between simulation and measurement data verified our claim on the new trace geometry.

The third topic focused on the technique that was used to characterize a connector-to-microstrip line transition, which was mounted on the ports of a circulator. Although the transition is needed by the network analyzer to measure the S-parameters of the device, it influences the measurement results. Therefore, to obtain the frequency response of the circulator, it is necessary to characterize this influence and then de-embed it from the results measured by the network analyzer. The characterizing technique discussed in this dissertation uses two passive calibration devices to obtain the characteristics of the connector. By utilizing the cascading property of the transmission matrix, the technique provides a simple way to solve the unknown connector's response from the transmission matrices of the calibration kit. The accuracy of the characterizing technique is validated by a third calibration device. It is also validated by the good correlation between simulated and measured frequency responses of a circulator.

The last topic of this dissertation focused on a newly developed numerical method for calculating the demagnetization factor of a non-ellipsoidal ferrite body. The demagnetization factor is an important property of a ferrite since it relates the external biasing field to the ferrite's internal field. Due to the non-uniformly distributed magnetization field inside the ferrite, it is more difficult to calculate the demagnetization factor for a non-ellipsoidal ferrite body. The method in this dissertation solves this type of problem by meshing the ferrite body using triangular prism or tetrahedra elements so that the non-uniformity of the magnetic field can be included into a distance factor in the calculation. Then by calculating the demagnetization field of each element, the demagnetization factor of the ferrite body is obtained from superposition. We demonstrated that the method has the capability of calculating the demagnetization factor of a rectangular slab, a disk and other irregular shapes. It also has the capability to model ferrite samples biased in non-z-direction.

6.1 Future Work

In the discussion of bandwidth optimization of an ideal ferrite circulator, we observed differences between the theoretical performance and the hardware performance. This suggests that there are deficiencies in the ideal model, e.g., the uniform internal field assumption. Therefore, the next step of research is to improve the ideal ferrite circulator model. Then by applying the bandwidth optimization procedure to this new model, we will have better prediction on the bandwidth limit of a circulator device.

The new center trace topology for a circulator discussed in this dissertation can be used in communication systems operating in frequency ranges other than 250-400 MHz. We have made progress on designing a lumped-element, ferrite circulator in the VHF band by re-optimizing the physical dimensions of the trace with the novel topology. There is more work that can be done along this direction, such as finishing the trace design and fabricating a hardware VHF circulator device with high isolation and wide bandwidth.

As for the demagnetization factor calculation method discussed in Chapter 5, there are two things that deserve additional attention. First, in Section 5.5, the treatment used to evaluate the surface integration over the side face of the tetrahedra elements is to approximate it by a product. This could be improved by directly evaluating the integration, as what was done in Section 5.4 for the triangular prism elements. This will result in a higher accurate method. Second, it is worth it to search for an algorithm that improves the calculation efficiency of the method. For example, for a ferrite sample with symmetrical geometrical shape, the current calculation treats it as a regular shaped body and uses a simple loop to obtain the demagnetization field from each meshing element. But with the improved method, the calculation time for a symmetrical shaped ferrite sample can be cut into half, or even by a quarter.

6.2 Publications

H. Dong, J. L. Young, J. R. Smith, and B. Aldecoa, "Maximum bandwidth performance for an ideal lumped-element circulator," *Progress in Electromagnetic Research C*, vol. 33, pp. 213–227, 2012.

H. Dong, J. R. Smith and J. L. Young, "A wide-band, high isolation UHF lumped-element ferrite circulator," *IEEE Microwave and Wireless Components Letters*, vol. 23, no. 6, pp. 294–296, 2013.

J. R. Smith, H. Dong, J. L. Young, B. Aldecoa, "Optimization of a broadband VHF lumped-element ferrite circulator," *Microwave and Optical Technology Letters*, vol. 55, issue 7, pp. 1476–1481, July 2013.

J. L. Young and H. Dong (Invited Keynote Speakers), "Recent advances in bandwidth and isolation enhancement for VHF-UHF lumped-element circulators," 9th IEEE International Symposium on Microwave, Antenna Propagation, and EMC Technologies for Wireless Communications, Chengdu, China, October 2013.

BIBLIOGRAPHY

[1] J. D. Adam, L. E. Davis, G. F. Dionne, E. F. Schloemann and S. N. Stitzer, “Ferrite devices and materials,” *IEEE Trans. Microwave Theory and Techniques*, vol. 50, no. 3, pp. 721–737, 2002.

[2] Y. Konishi, “Lumped element Y circulator,” *IEEE Trans. Microwave Theory and Techniques*, vol. 13, no. 6, pp. 852–864, 1965.

[3] T. Miura, M. Kobayashi and Y. Konishi, “Optimization of a lumped element circulator based on eigenvalue evaluation and structural improvement,” *IEEE Trans. Microwave Theory and Techniques*, vol. 44, no. 12, pp. 2648–2654, 1996.

[4] E. F. Schloemann, “Circulators for microwave and millimeter-wave integrated circuits,” *Proceedings of the IEEE*, vol. 76, no. 2, pp. 188–200, 1988.

[5] Y. Konishi, “New theoretical concept for wide band gyromagnetic devices,” *IEEE Trans. Magnetics*, vol. 8, no. 3, pp. 505–508, 1972.

[6] Y. Konishi, “Lumped element circulator,” *IEEE Trans. Microwave Theory and Techniques*, vol. 11, no. 5, pp. 1262–1266, 1975.

[7] S. Takeda, H. Mikami and Y. Sugiyama, “Lumped-element isolator with lower symmetrical configuration of three windings,” *IEEE Trans. Microwave Theory and Techniques*, vol. 52, no. 12, pp. 2697–2703, 2004.

[8] L.K. Anderson, “An analysis of broadband circulators with external tuning elements,” *IEEE Trans. Microwave Theory and Techniques*, vol. 15, no. 1, pp. 42–47, 1967.

[9] R. I. Joseph and E. Schlomann, “Demagnetizing field in nonellipsoidal bodies,” *Journal of Applied Physics*, vol. 36, no. 5, pp. 1579–1593, 1965.

[10] R. I. Joseph, “Ballistic demagnetizing factor in uniformly magnetized cylinders,” *Journal of Applied Physics*, vol. 37, no. 13, pp. 4639–4643, 1966.

[11] E. Schlomann, “A sum rule concerning the inhomogeneous demagnetizing field in nonellipsoidal samples,” *Journal of Applied Physics*, vol. 33, no. 9, pp. 2825–2826, 1962.

[12] L. Kraus, “The demagnetization tensor of a cylinder,” *Czechoslovak Journal of Physics B*, vol. 23, issue 5, pp. 512–519, 1973.

[13] M. Kobayashi and Y. Ishikawa, “Surface magnetic charge distributions and demagnetizing factors of circular cylinders,” *IEEE Trans. Magnetics*, vol. 28, no. 3, pp. 1810–1814, 1992.

[14] X.H. Huang and M. Pardavi-Horvath, “Local demagnetizing tensor calculation for arbitrary non-ellipsoidal bodies,” *IEEE Trans. Magnetics*, vol. 32, no. 5, pp. 4180–4182, 1996.

[15] J.O. Bergman, “Equivalent circuit for a lumped-element Y circulator,” *IEEE Trans. Microwave Theory and Techniques*, vol. 16, no. 5, pp. 308–310, 1968.

[16] D. Polder, “On the theory of ferromagnetic resonance,” *Philosophical Magazine*, vol. 40, issue 300, pp. 99–115, 1949.

[17] C. M. Krowne and R. E. Neidert, “Theory and numerical calculations for radially inhomogeneous circular ferrite circulators,” *IEEE Trans. Microwave Theory and Techniques*, vol. 44, no. 3, pp. 419–431, 1996.

[18] J. L. Young and C. M. Johnson, “A compact, recursive trans-impedance Green’s function for the inhomogeneous ferrite, microwave circulator,” *IEEE Trans. Microwave Theory and Techniques*, vol. 52, no. 7, pp. 1751–1759, 2004.

[19] Y. S. Wu and F. J. Rosenbaum, “Wide-band operation of microstrip circulators,” *IEEE Trans. Microwave Theory and Techniques*, vol. 22, no. 10, pp. 849–856, 1974.

[20] J. L. Young, R. S. Adams, B. O’Neil and C. M. Johnson, “Bandwidth optimization of an integrated microstrip circulator and antenna assembly: Part 2,” *IEEE Antennas and Propagation Magazine*, vol. 49, no. 1, pp. 82–91, 2007.

[21] R. H. Knerr and C. E. Barnes, “A compact broad-band thin-film lumped element L-band circulator,” *IEEE Trans. Microwave Theory and Techniques*, vol. 18, no. 12, pp. 1100–1108, 1970.

[22] R. H. Knerr, “An improved equivalent circuit for the thin-film lumped element circulator,” *IEEE Trans. Microwave Theory and Techniques*, vol. 20, no. 7, pp. 446–452, 1972.

[23] J. C. Allen, H^∞ *Engineering and Amplifier Optimization*, Birkhäuser, Boston, MA, 2004.

[24] B. J. Aldecoa, “Bandwidth optimization of UHF-VHF circulators, *Thesis (M.S., Electrical and Computer Engineering),* University of Idaho, December 2010.

[25] J. R. Smith, “The design, optimization and fabrication of UHF-VHF circulators,” *Thesis (M.S., Electrical and Computer Engineering),* University of Idaho, August 2012.

[26] D. M. Pozar, *Microwave Engineering, 3rd. Ed.*, John Wiley and Sons, Inc, Hoboken, NJ, 2005.

[27] M. A. Goodberlet and J. B. Mead, “Microwave connector characterization,” *IEEE Microwave Magazine*, October 2006.

[28] ANSYS, Inc., High Frequency Structural Simulator (HFSS). Available at http://www.ansys.com.

[29] Z. Chen and Z. Cui, *Fundamentals of Electromagnetics Theory, 2nd. Ed.*, Beijing Institute of Technology Press, 2010.

[30] P. Persson, “Mesh Generation for implicit geometries,” *Thesis (M.S., Department of Mathematics),* Massachusetts Institute of Technology, 2005.

[31] M. R. Spiegel, S. Lipschutz and J. Liu, *Mathematical Handbook of Formulas and Tables, 3rd. Ed.*, The McGraw-Hill Companies, Inc., 2009.

[32] S. Amari and J. Bornemann, “Efficient numerical computation of singular integrals with application to electromagnetics,” *IEEE Trans. Antennas and Propagation*, vol. 43, no. 11, pp. 1343–1348, 1995.